Dissertation

submitted to the
Combined Faculties of the Natural Sciences and Mathematics
of the Ruperto-Carola-University of Heidelberg, Germany
for the degree of
Doctor of Natural Sciences

Put forward by
Dipl.-Phys. Andreas Kaldun
born in: Saarbrücken

Oral examination: 16.04.2014

Fano Resonances in the Time Domain

- understanding and controlling the absorption and emission of light

Referees: **Dr. Thomas Pfeifer**
Prof. Dr. Selim Jochim

Fano Resonanzen im Zeitbereich - Verständnis und Kontrolle von Lichtabsorption und -emission—Innerhalb dieser Arbeit wird, ausgehend von der bereits bekannten Theorie zum Wirkungsquerschnitt der Photoabsorption von Ugo Fano, ein Formalismus entwickelt, mit dessen Hilfe Phasen- und Amplitudenänderungen eines abstrahlenden Dipols ausgelesen und kontrolliert werden können. Anhand von experimentellen Messergebnissen in einfach und doppelt angeregten Helium wird die Gültigkeit dieses Formalismus gezeigt. Darüber hinaus wird eine Anwendung des Formalismus im Gebiet der zeitabhängigen Quanten-Holographie von angeregten Zuständen gezeigt, die es erlaubt, die verschiedenen Pfade der Laser-induzierten Wechselwirkung zu separieren.

Fano Resonances in the Time Domain - understanding and controlling the absorption and emission of light—Within this work, starting from the well known theory for photoabsorption cross sections by Ugo Fano, a new formalism is developed, which enables measurement and control of phase and amplitude changes in an emitting dipole. This is shown by experimental measurements in singly and doubly excited helium that confirm the formalism. An application in time-domain quantum holography of excited states, allowing to separate laser-induced coupling pathways, is also presented.

List of Publications

Parts of this work have been published or prepared in the following references:

A. Kaldun, C. Ott, A. Blättermann, M. Laux, K. Meyer, T. Ding, A. Fischer, and T. Pfeifer.
Extracting phase- and amplitude modifications of laser-coupled Fano resonances.
accepted by Phys. Rev. Lett. (2014).
(for additional information see [1])

C. Ott, A. Kaldun, P. Raith, K. Meyer, M. Laux, J. Evers, C. Keitel, C. Greene, and T. Pfeifer.
Lorentz meets Fano in spectral line shapes: A universal phase and its laser control.
Science **3** 537- 542 (2013).
(for additional information see [2])

C. Ott, A. Kaldun, L. Argenti, P. Raith, K. Meyer, M. Laux, Y. Zhang, A. Blättermann, S. Hagstotz, T. Ding, R. Heck, J. Madroñero, F. Martin and T. Pfeifer.
Time-dependent two-electron wave-packet observation and control.
submitted (2013).
(for additional information see [3])

Further publications with own contributions:

C. Ott, M. Schönwald, P. Raith, A. Kaldun, G. Sansone, M. Krüger, P. Hommelhoff, Y. Patil, Y. Zhang, K. Meyer, M. Laux and T. Pfeifer.
Strong-field spectral interferometry using the carrier–envelope phase.
New J. Phys. **15**, 073031 (2013).
(for additional information see [4])

P. Raith, C. Ott, K. Meyer, A. Kaldun, M. Laux, M. Ceci, C. P. Anderson and T. Pfeifer.
Carrier-envelope phase- and spectral control of fractional high-harmonic combs.
J. Appl. Phys., **114**, 17 (2013).
(for additional information see [5])

M. Kübel, N. G. Kling, K. J. Betsch, N. Camus, A. Kaldun, U. Kleineberg, I. Ben-Itzhak, R. R. Jones, G. G. Paulus, T. Pfeifer, J. Ullrich, R. Moshammer, M. F. Kling and B. Bergues.
Nonsequential double ionization of N_2 in a near-single-cycle laser pulse.
Phys. Rev. A **88**, 023418 (2013).
(for additional information see [6])

K. Meyer, C. Ott, P. Raith, A. Kaldun, Y. Jiang, A. Senftleben, M. Kurka, R. Moshammer, J. Ullrich, and T. Pfeifer.
Noisy Optical Pulses Enhance the Temporal Resolution of Pump–Probe Spectroscopy.
Phys. Rev. Lett. **108**, 098302 (2012).
(for additional information see [7])

P. Raith, C. Ott, C. P. Anderson, A. Kaldun, K. Meyer, M. Laux, Y. Zhang and T. Pfeifer.
Fractional high-order harmonic combs and energy tuning by attosecond-precision split-spectrum pulse control.
Appl. Phys. Lett. **100**, 121104 (2012).
(for additional information see [8])

T. A. Moore, P. Möhrke, L. Heyne, A. Kaldun, M. Kläui, D. Backes, J. Rhensius, L. J. Heyderman, J. U. Thiele, G. Woltersdorf, A. Fraile Rodríguez, F. Nolting, T. O. Menteş, M. Á. Niño, A. Locatelli, A. Potenza, H. Marchetto, S. Cavill and S. S. Dhesi.
Magnetic-field-induced domain-wall motion in permalloy nanowires with modified Gilbert damping.
Phys. Rev. B **82**, 094445 (2010).
(for additional information see [9])

Contents

Chapter 1

Introduction

How is a spectroscopic absorption line formed? This seemingly simple and yet fundamental question was asked for the first time exactly 200 years ago. In the year 1814 Joseph von Fraunhofer [10] published a systematic investigation about the absorption lines in the spectrum of the sun. Since then, spectroscopic techniques evolved and became the most important tool that astronomers have at hand [11] to study the formation of stars [12] and the distribution of hydrogen in the universe [13] by observing the Lyman-series [14], which consists of spectral lines of atomic hydrogen in the ultraviolet regime. In parallel, spectroscopy was developed into a high precision method for atomic, molecular and nuclear physics. In this context, monochromatic light is used to study the properties of matter and determine fundamental physical constants like the size of the proton [15] or the Rydberg constant [16]. The latter is amongst the most precise physical constants determined to an extraordinary relative precision of $5.0 \cdot 10^{-12}$ [17], again by spectroscopy of the Lyman-series of atomic hydrogen [18].

As all absorption lines of atomic hydrogen show a symmetric Lorentzian profile [19] it came as a surprise when, as a result of the increasing spectroscopic resolution, asymmetric absorption line shapes were observed in 1935 in the absorption spectrum of various noble gases for ultraviolet light [20]. While the symmetric Lorentzian line shape is understood as an exponential decay of a discrete excited state with a finite lifetime, there was no explanation for the newly discovered asymmetric line shapes. In the same year Ugo Fano, inspired by the work of Ettore Majorana[1] published an article explaining these asymmetric line shapes [23]. The accordingly named Fano line shape is understood to be caused by discrete states coupled to a continuum of states. In addition, it was found that the occurrence of the Fano line shapes is a general phenomenon in various research fields, such as nuclear [25], atomic [26–28] and solid-state physics [29–32], as well as chemistry [33]. Later, Fano developed a general theory based on the example of doubly-excited states in helium [34]. There, he introduced the so called q-asymmetry parameter, which is

[1] Ettore Majorana in 1931 already published [21] his considerations on the role of selection rules for the non-radiative decay of two electron excitations in atomic spectra [22], explicitly involving the configuration interaction between discrete and continuum channels, inspiring other works on line shape analysis, e.g. by Ugo Fano [23], Herman Feshbach [24] and many more.

proportional to the ratio between the bound–bound and the bound–continuum transition probability and determines the symmetry of the line shapes. With a quantum-mechanical calculation determining the transition probabilities, the line shape is exactly predicted, see for example Rost *et al.* [28], who explained even tiny differences in the Fano resonances line shapes of doubly-excited helium, which have been found in high-precision studies (e.g. [35]). The authors conclude that "the q-parameter is a much more sensitive probe of the dynamics than the resonance positions and even the widths" [28].

Today, high-precision spectroscopy techniques use monochromatic light which is δ-like in the spectral domain, thus creating well-defined light-induced states. Using such a light field which is nearly infinitely long in time, the dynamical information of the system, encoded in the spectral phase, is typically lost. By contrast, a short, almost δ-like pulse allows for a high temporal resolution resulting in a nearly continuous spectrum. A pulse is considered short when its duration is short compared to the time scale of the dynamics of the system. For atomic systems this time scale is determined by the electronic transitions and typically lies in the femtosecond (10^{-15} s) regime. With the development of mode-locked lasers [36] pulse durations in the near infrared and visible regime (VIS) decreased rapidly. With Kerr-lens mode locked laser systems [37] pulse durations in the femtosecond regime became available in the early 1990's. Only a few years later, in 2001, the first pulse trains in the extreme ultraviolet (XUV) regime were reported [38] having a duration of a few hundred attoseconds (10^{-18} s) making use of high-order harmonic generation (HHG) in a gaseous target by intense laser pulses [39, 40].

In this work we combine the field of high resolution spectroscopy and the field of short-pulse physics enabling a high resolution in the spectral and temporal domain. Having these optical precision tools at hand,we are able to address the following scientific questions:

What does spectroscopy with short pulses mean?

How is absorption understood in the time domain?

To what extent can absorption, in general, be controlled?

Answers to these questions help to understand and to formulate new descriptions of dynamics in light–matter interaction. As Fano described the asymmetric line profile on the example helium–the model system for two-electron dynamics–we will use helium gas in the experiments presented in this work. To excite the two-electron dynamics, we use HHG to produce an attosecond light pulse in the extreme ultraviolet regime (XUV). The XUV light passes through the helium gas target and populates the singly excited 1snp states (with bound–bound transitions only) and the doubly excited $\mathrm{sp}_{2,n+}$ states embedded in the $N = 1$ continuum (with both bound–bound and bound–continuum transitions). From a time-domain perspective, in our spectral interferometer [41, 42] we record the interference between the transmitted XUV light and the light emitted by the decay of the induced polarization. The interference pattern is the line shape of the state. As the emitted light interferes with the transmitted exciting XUV pulse in the spectrometer, the relative phase

information is also encoded in spectral line shapes [43, 44]. If freely decaying, the singly excited 1snp states exhibit symmetric Lorentzian line shapes while the doubly excited $\mathrm{sp}_{2,n+}$ states feature the above mentioned asymmetric Fano line profiles, quantified by the q parameter. For the temporal interpretation used in this work we develop a mapping between the q parameter and the relative phase between the two interfering light fields.

To learn more about the dipole response of the system, we use the excitation of the system as a reference for time $t = 0$ and then–instead of letting the polarization induced by the XUV light decay freely–we perturb the decay by a second light pulse following the XUV closely. This second light pulse is a 7 fs laser pulse in the visible (VIS) regime. We observe that the line shape changes periodically as a function of the intensity and the time delay of the VIS pulse. By setting a fixed time-delay and controlling the intensity, we show how an asymmetric Fano line shape is turned into a symmetric Lorentzian one and *vice versa*. It is even possible to turn an original absorption of light into an emission line. All these observed phenomena are then explained in our Fano phase formalism [2] by *non-resonant*, ponderomotive coupling to a nearby continuum of states. In this formalism we show the intensity dependence of the phase $\varphi = 2\arg(q - \imath)$ between the XUV light and the light emitted by the decay of the induced polarization.

By contrast, the *resonant* coupling of states by pulsed coherent light fields is of substantial interest e.g. to fully understand the creation and probing of electronic wave packets [45–48]. We therefore also examine the *resonant* coupling of two states by interaction with a VIS pulse. For a resonant coupling, the VIS pulse can transfer population depending on its time delay with respect to the exciting XUV pulse. This population transfer alters the spectral amplitude and phase of the light compared to the light from the unperturbed decay (without the VIS pulse) as a function of the time delay. We show, how within a quarter of the VIS period (≈500 attoseconds) an asymmetric Fano line shape is turned into a symmetric Lorentzian one. To explain this fast line shape changes, we develop a generalized model of the Fano-phase formalism [1] and apply it to the measurement of time-dependent phases and amplitudes induced by short-pulsed resonant laser coupling. This model allows to extract the amplitude modifications A_{mod} and phase modifications φ_{mod} by the VIS laser and, thereby, enables the separation of different few-photon quantum pathways that are involved in the coupling dynamics of the autoionizing states. As stated above, the Fano q parameter is a sensitive test of atomic structure calculations under field-free conditions [28,49,50]. In the same way, the determination of the laser-controlled phase φ by the model developed in this work, may in the future provide a sensitive test of time-dependent quantum-dynamics theory [51].

This thesis is structured as follows: In **chapter 2**, the fundamentals of light–matter interaction are recalled based on the example of a few-level system (treated perturbatively and non-perturbatively) with emphasis on the connection between descriptions in the temporal and spectral domain. In **chapter 3**, the multidimensional spectroscopy setup is described in detail. This apparatus allows to measure the spectral line shape as a function of the VIS pulse intensity, the temporal delay of this VIS pulse to attosecond pulsed XUV light, the spatial orientation of both pulses and the density of the target gas atoms. In **chapter 4** the main scientific results of this work are presented. We first show the experimental control

of the line shapes of singly and doubly excited helium states with the 7 fs-VIS pulse and the development of the generalized Fano-phase formalism. This provides a framework to interpret the line-shape control as a "phase kick" of the dipole response by the VIS laser pulse. Further, the investigation of *resonant* population transfer allows to extract the dipole phase relative to the exciting field and thereby gives access to information on the few-photon quantum pathways involved in the coupling dynamics. Finally, in **chapter 5** the results of this work are summarized and an outlook is given on the applications of the presented mechanism, e.g. in the hard-x-ray or γ-ray regime.

Chapter 2

Fundamentals of Light-Matter Interaction

The understanding of light–matter interaction is at the heart of any time-resolved experiment that uses electromagnetic fields as a probe of quantum dynamics. For the experiments presented in this work, the system of interest is helium. While the singly excited 1snp series of helium features a Lorentzian line shape in an spectrometer monitoring the extreme ultra-violet light (XUV) transmission, the first doubly excited resonance series of helium exhibits asymmetric Fano line profiles. In this chapter we will transfer the spectral picture of an absorption line into the temporal understanding as an interference between an exciting light field transmitted through the sample and the re-emission by the decay of the induced polarization on the example of a symmetric Lorentzian line profile (**section 2.1.1**) as well as for a asymmetric, Fano line shape (**section 2.1.2**). The temporal picture is favored, as we use ultra short pulses for the experiments presented in this work to map out the dynamics of the system. To theoretically model the physical processes behind the measured dynamics, we recall the properties of a two-level system coupled to a electromagnetic field (**section 2.3**) and extend this to a few–level-λ (or Ξ) system (**section 2.4**). The actual system under study, the helium atom, is discussed with all involved states in **section 2.5**.

At the end of this chapter, we also outline the techniques to produces ultra short pulses with pulse durations in the range of a few femtoseconds for visible (VIS) light (**section 2.6.1**) and in the few–hundred-attosecond regime for XUV light (**section 2.6.2**) .

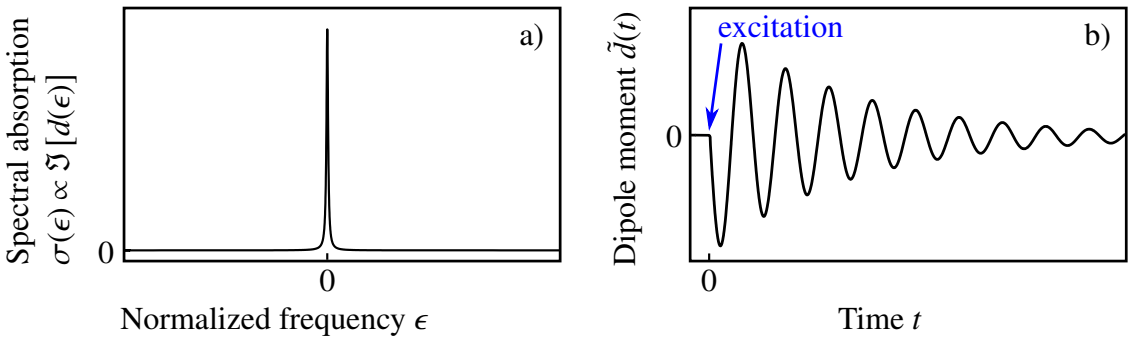

Figure 2.1: a) Lorentzian spectral absorption line shape for the normalized frequency $\epsilon = \frac{\omega-\omega_r}{\hbar\Gamma/2}$ b) Lorentzian temporal dipole response function, the well-known exponential decay, starting after an excitation at time $t = 0$.

2.1 Time Dependent Dipole Moment

2.1.1 Symmetric Lorentzian Line Shapes

If an optical transition between two states with energies E_{ground} and E_{excited} is driven by electromagnetic radiation, a dipole moment between the involved states is induced. In the framework of classical electrodynamics the amplitude of the induced dipole decreases exponentially over time by radiative decay. Mathematically this is described by

$$\tilde{d}(t) \propto \mathrm{e}^{-\Gamma/2} \sin(\omega_r t)\, \theta(t) \tag{2.1}$$

with the resonance energy $\omega_r = (E_{\text{excited}} - E_{\text{ground}})/\hbar$ and the decay rate $\Gamma = 1/\tau$. The Heaviside function $\theta(t)$ starts the dipole oscillation at $t = 0$. The spectral width of the emitted light is inversely proportional to the lifetime τ of the state.The Fourier transformation of $\tilde{d}(t)$ reads

$$d(\omega) \propto \frac{\omega_r}{\omega_r^2 + (\Gamma - \imath\omega)^2} \tag{2.2}$$

Experimentally, the quantity of interest is the photo-absorption cross section σ_{abs} since its measurements gives access to the dynamics of the studied system. The connection between the photo-absorption cross section an the dipole response of the system is derived in detail in appendix B.2. In a nutshell the photo-absorption cross section is proportional to the imaginary part of the refractive index which in turn is proportional to the polarizability and thus to the frequency-dependent dipole response function $d(\omega)$. As a result the photo-absorption cross section

$$\sigma_{\text{abs}}(\omega) \propto \Im(d(\omega)) \tag{2.3}$$

The spectral dipole response $d_(\omega)$ has an Lorentzian profile of width $\Gamma = 1/\tau$, thus the absorption cross section of a dipole also has a Lorentzian shape (see Fig. 2.1).

The relative phase offset between this decaying dipole and the electromagnetic radiation which originally excited the atom plays a major role for the interpretation of the

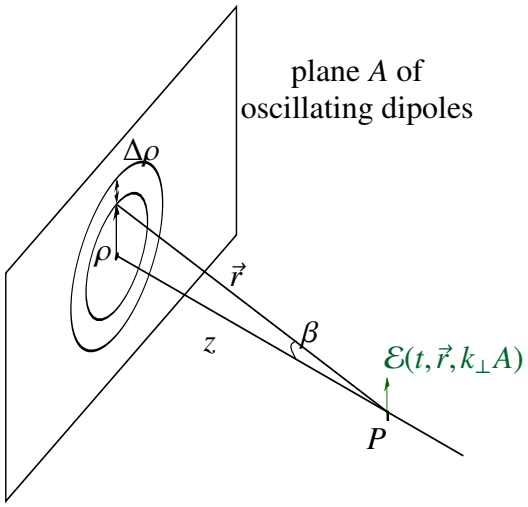

Figure 2.2: Electric field phase shift of a plane A of dipoles compared to a single dipole at point P. With z denoting the distance from P to A and $\vec{r}$ the vector from P to each dipole. Integration over the plane goes along ρ. Only the electric field $\mathcal{E}(t,\vec{r},k_\perp)$ parallel to the plane of dipoles is of interest.

results presented in this work, so some consideration will be spent on it in the following paragraphs. Is the dipole driven resonantly by the exciting field, the phase of the dipole is shifted by $\pi/2$ against the phase of the exciting field if measured in the far-field of the dipole. The same result is obtained by solving the Schrödinger equation for a plane wave [52].

Later in this work, emissions from dilute gases will be investigated therefore we now consider not only one dipole, but a plane full of dipoles and check how the phase of the combined emitted fields far away from the plane is related to the phase of the exciting field. Starting with classical electrodynamics, the electric field $\mathcal{E}_{\text{SingleDipole}}$ of a single dipole is proportional to the acceleration of the charges $-x_0\omega_0^2\cos(\omega_0 t)$ with x_0 the physical dimension of the dipole and $\omega_\text{r} = {}^{(E_\text{excited}-E_\text{ground})}/_\hbar$, like defined above. The electric field perpendicular to the normal vector of the plane (see Fig. 2.2) at a point P at distance z from the plane in atomic units (see apendix A) is given by

$$\mathcal{E}_{\text{SingleDipole}} = {}^{q}/_{c^2}\cdot\cos(\beta)\frac{x_0\cdot\omega_\text{r}^2\cos\left(\omega_\text{r}(t-{}^{r}/_{c})\right)}{r} = {}^{q}/_{c^2}\cdot\frac{z x_0\cdot\omega_\text{r}^2\cos\left(\omega_\text{r}(t-{}^{r}/_{c})\right)}{r^2} \tag{2.4}$$

with the vector $\vec{r}$ connecting point P and the center of the dipole, the angle β between $\vec{r}$ and the normal vector of the plane and $\cos(\beta) = {}^{z}/_{r}$, the speed of light c in atomic units (see Append. A) and the number of electrical charges q. The electric field of all N dipoles in the plane at the point P in distance z is a vector sum of the individual electric fields with distance r and reads (see Chapter 30-7 in [53])

$$\mathcal{E}_{\text{Total}} = -2\pi\cdot{}^{q}/_{c}\cdot N\cdot x_0\cdot\omega_0\cdot\sin\left(\omega_0(t-{}^{z}/_{c})\right). \tag{2.5}$$

Interestingly, for a plane of dipoles a retardation occurs, corresponding to in a phase shift of $\pi/2$ [54, 55] compared to the single dipole response [1] in equation 2.4. In total the phase

[1] This behavior and a more detailed derivation is discussed by Richard Feynman in his famous lectures [53]

shift of the dipole response is π. If both the excitation pulse and the dipole emission are observed in a spectrometer, there will be destructive interference [2] due to the phase shift of π. The recorded spectrum shows the envelope of the exciting pulse before the interaction now with an absorption line around the dipole emission frequency. The absorption line profile is Lorentzian as the spectral distribution of the dipole emission was Lorentzian, too. The correspondence principle translates this classically derived result into quantum mechanics. A single atom in an excited state will emit exactly one photon, but the time of its emission cannot be predicted, although the probability distribution is known. The spectral width of the emitted photons is inversely proportional to the life time of the state. Looking at the number of photons emitted by an ensemble of excited atoms, an exponentially decreasing behavior is observed like for the electric field in the classical case.

2.1.2 Asymmetric Fano Line Shapes

Some Rydberg series of spectral lines in an atom are superimposed on the continuous spectrum of a different configuration. In the case that both configuration interact with each other also the decay is affected and the theory presented in the previous chapter has to be modified to take this changes into account. Effects of interaction between different configurations in the case of noble gases have been investigated by Ugo Fano [23] after their observation by Herbert Beutler [20] in studies of absorption of noble gases. Beutler found asymmetric line shapes for the high energetic Rydberg series in contrast to the symmetric Lorentzian line shapes found for the case of energies below 24.6 eV, the first ionization potential of helium. Fano [23, 34] described the asymmetric line shapes by the energy-dependent absorption of a discrete bound state $|\varphi\rangle$ at energy E_r having spectral width Γ, that is embedded within a continuous set of states $|\chi_E\rangle$ (which will be called continuum in the following). The bound state and the continuum are energetically degenerate. If they interact with each other neither $|\varphi\rangle$ nor $|\chi_E\rangle$ is an eigenstate of the interaction Hamiltonian. In [34] it is described in detail how the new eigenstate $|\Psi_E\rangle$ is expressed in a basis set spanned by $|\varphi\rangle$ and $|\chi_E\rangle$. As a result, the two configurations $|\varphi\rangle$ and $|\chi_E\rangle$ interfere constructively on one side of the resonance energy E_r and destructively on the other side, which gives rise to an asymmetric line shape. To parametrize this asymmetry Fano considered the relation between the following two transition probabilities. First, the probability of the transition $\langle\Psi_E|\hat{\mathbf{T}}|g\rangle$ from the ground state $|g\rangle$ into the new eigenstate $|\Psi_E\rangle$. Second the probability of the transition $\langle\chi_E|\hat{\mathbf{T}}|g\rangle$ from the ground state into the undisturbed continuum $|\chi_E\rangle$, without taking into account the bound state $|\varphi\rangle$. The last assumption means we neglect radiative decay Γ_rad which almost always happens on much longer time scales than the autoionization ($\Gamma_\mathrm{rad} \ll \Gamma_\mathrm{auto}$). Thus, we set $\Gamma = \Gamma_\mathrm{auto}$. Now

[2] This is true for most of the spectrometer apparatus, but technically speaking the coherence depends on the physical dimensions of the spectrograph. For a more detailed explanation as well as a calculation for the experimental setup used for this work see Fig. 3.7 on page 35.

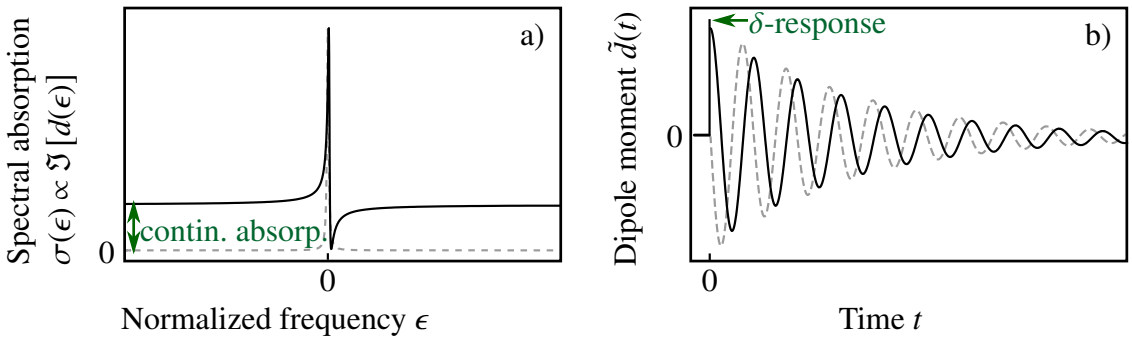

Figure 2.3: a) Fano spectral absorption line shape (solid, black curve) and Lorentzian spectral absorption line shape (dashed, grey curve). The off-resonace difference of both curves is marked by a green arrow. The Lorentzian line goes to zero far off the resonance, while the Fano line has a (constant) finite value. This finite value is the continuum absorption, which gives rise to the δ-peak in subplot b) where the Fano temporal dipole response function (solid, black curve) is shown, consisting of this instantaneous δ-response (due to the continuum absorption), marked by the green arrow, and an exponentially decaying response, governed by autoionization. The Lorentzian temporal dipole response from Fig. 2.1 is shown for comparison (dashed, grey curve). The asymmetric Fano line shape is caused by a phase shift φ_{Fano} of the exponentially decaying dipole response as compared to the Lorentzian case.

looking at the ratio between both probabilities, it is possible to parametrize the ratio

$$\frac{\left|\langle \Psi_E | \hat{\mathbf{T}} | g \rangle\right|^2}{\left|\langle \chi_E | \hat{\mathbf{T}} | g \rangle\right|^2} = \frac{\left|q+\epsilon\right|^2}{1+\epsilon^2} \tag{2.6}$$

where the reduced energy ϵ is defined as

$$\epsilon = \frac{E - E_{\text{r}}}{\hbar\Gamma/2}. \tag{2.7}$$

by using the asymmetry parameter

$$q = \frac{\langle \Phi | \hat{\mathbf{T}} | g \rangle}{\pi V_E^* \langle \chi_E | \hat{\mathbf{T}} | g \rangle} \tag{2.8}$$

with the modified bound state $\langle \Phi|$ and the configuration-interaction matrix element V_E^* which describes the interaction of the discrete state at energy E_{r} with a continuum state at energy E. For a detailed derivation see the review by Ugo Fano from 1961 [34], which was judged to be among the most influential papers published in the history of The Physical Review journal series [56]. The non-resonant continuum absorption $\langle \chi_E | \hat{\mathbf{T}} | g \rangle$ is also called background absorption, since it is present over the whole spectrum and varies only slowly with the photon energy, in contrast to the resonant absorption of discrete states. The corresponding photo absorption cross section σ_0 will accordingly be called background cross section. Equation 2.6 is then rewritten in terms of the photo-absorption cross section:

$$\frac{\sigma_{\text{Fano}}}{\sigma_0} = \frac{\left|q+\epsilon\right|^2}{1+\epsilon^2}. \tag{2.9}$$

To develop a more generalized theory of asymmetric line shape, we now formulate the Fano photo-absorption cross section in units of the background absorption and arrive at the simple expression

$$\sigma_{\text{Fano}} = \sigma_0 \frac{(q+\epsilon)^2}{1+\epsilon^2}. \tag{2.10}$$

Note that the absolute value in Equ. 2.9 is neglected since $q, \epsilon \in \mathbb{R}$. To check the scope of application of Equ. 2.10 we look at the behavior far away from the resonance, i.e. $\epsilon \to \pm\infty$. Therefore we rewrite the formula as follows

$$\lim_{\epsilon\to\pm\infty} \sigma_{\text{Fano}} = \lim_{\epsilon\to\pm\infty} \sigma_0 \left(\frac{q^2+2q\epsilon-1}{1+\epsilon^2} + 1 \right) = \sigma_0 \tag{2.11}$$

In this work, we focus on the time-dependent evolution of the dipole. In order to get the time dependent dipole response, real and imaginary part of the dipole-response function have to be determined. In part 2.1.1 it was shown that the photo-absorption cross section is proportional to the imaginary part of the dipole response (see Equ. 2.3). This is also true in the vicinity of an autoionizing resonance [27]. As the imaginary part represents the absorption, the real part describes the dispersion[3]. The Kramers-Kronig relation [57] is used to determine the real part of the dipole response:

$$\begin{aligned} Re\left[d(\epsilon)\right] &= {}^1\!/\!_\pi P \int_{-\infty}^{\infty} \frac{\Im\left[d(\epsilon)\right]}{x-\epsilon} \mathrm{d}x \\ &\propto {}^1\!/\!_\pi P \int_{-\infty}^{\infty} \sigma_0 \left(\frac{q^2+2q\epsilon-1}{\left(1+\epsilon^2\right)(x-\epsilon)} + \frac{1}{x-\epsilon} \right) \mathrm{d}x. \end{aligned} \tag{2.12}$$

To remove the discontinuity at $x = \epsilon$ we introduce an infinitely broad discrete state to replace the normalized continuum. The infinitely broad discrete state will have a normalized Lorentzian line shape. Then the imaginary part of the complex dipole response is of the form [27]

$$\Im\left[d(\epsilon)\right] \propto \lim_{\alpha\to 0} \sigma_0 \left[\frac{q^2+2q\epsilon-1}{1+\epsilon^2} + \frac{1}{1+(\alpha\epsilon)^2} \right] \tag{2.13}$$

Then the integral in Equ. 2.12 gives the following solution for the full complex dipole response:

$$d(\epsilon) \propto \lim_{\alpha\to 0} \left[\left(\frac{\sigma_0\left(\epsilon + q(2-q\epsilon)\right)}{1+\epsilon^2} - \frac{\alpha\epsilon\sigma_0}{1+(\alpha\epsilon)^2} \right) + \imath \left(\frac{\sigma_0\left(q^2+2q\epsilon-1\right)}{1+\epsilon^2} + \frac{\sigma_0}{1+(\alpha\epsilon)^2} \right) \right] \tag{2.14}$$

Comparing the terms where α appears within Equ. 2.2 we find that the terms containing the infinitely broad discrete state describe the well-known dispersion and absorption of an exponentially-decaying state. The limit of $\alpha \to 0$ will be taken at the end of this paragraph since we validate the following steps in the derivation with the widely-known behavior of a Lorentzian of width Γ/α . Up to here the formula is exact in terms of a response function, i.e. the time- or frequency-dependent dipole as excited by a driving delta function at time zero. Fano and Cooper in 1968 already stated[4]:

[3] this relation is more commonly known for the refractive index

[4] See [58] on page 446 in section "Time Correlations".

In this context one may also consider how the mean electric dipole moment of an atom varies in time following an initial disturbance.

To calculate the time-dependent response function $\tilde{d}(t)$ we apply a Fourier transformation on $d(\epsilon) = d\left(\frac{E-E_\mathrm{r}}{\Gamma/2}\right) = d\left(\frac{\omega-\omega_\mathrm{r}}{\Gamma/2}\right)$ (taking into account equations 2.14 and 2.7 and $\hbar = 1$ in atomic units):

$$\tilde{d}(t) = {}^1\!/_{2\pi} \int_{-\infty}^{\infty} d\left(\frac{\omega-\omega_\mathrm{r}}{\Gamma/2}\right) \mathrm{e}^{\imath\omega t}\mathrm{d}\omega \tag{2.15}$$

$$\propto \imath \lim_{\alpha\to 0}\left[\frac{\Gamma/\alpha}{2}\mathrm{e}^{\left(-\frac{\Gamma/\alpha}{2}+\imath\omega_\mathrm{r}\right)t}\right]\theta(t) + \imath\frac{\Gamma}{2}\mathrm{e}^{-\frac{\Gamma}{2}t}(q-\imath)^2\mathrm{e}^{\imath\omega_\mathrm{r}t}\theta(t) \tag{2.16}$$

where $\theta(t)$ is the Heaviside step function indicating the instantaneous switch-on of the dipole response with the δ-like excitation. The first term is the Lorentzian shaped decaying discrete state of width Γ/α, which aproximates the continuum states and oscillates with the resonance frequency ω_r. The second term also is a decaying discrete state, also oscillating with the resonance frequency ω_r, but of width Γ. The main difference is the additional factor $(q-\imath)^2$, which changes the Lorentzian line shape and therefore, depending on the exact value of q, reassembles the autoionizing Fano resonance shape. To get back to a "real continuum", we now execute the limit $\alpha \to 0$:

$$\tilde{d}(t) \propto \imath\left[\delta(t) + \frac{\Gamma}{2}\mathrm{e}^{-\frac{\Gamma}{2}t}(q-\imath)^2\mathrm{e}^{\imath\omega_\mathrm{r}t}\right]\theta(t) \tag{2.17}$$

The first term in Equation 2.17 has the intuitive physical interpretation of an infinitely short contribution $\delta(t)$ associated with the continuum. The second term is a decaying discrete state of autoionization width Γ at resonance position ω_r and with an additional factor $(q-\imath)^2$. This additional complex factor is due to the configuration interaction and is now expressed in an exponential representation

$$(q-\imath)^2 = (q^2+1)\mathrm{e}^{\imath\varphi(q)} \tag{2.18}$$

where the real amplitude (q^2+1) is the absolute value of $(q-\imath)^2$. Simultaneously the Fano asymmetry parameter q is directly mapped into an effective phase

$$\varphi(q) = 2\arg(q-\imath). \tag{2.19}$$

The final dipole response function

$$\tilde{d}(t) \propto \imath\left[\delta(t) + \frac{\Gamma}{2}\mathrm{e}^{-\frac{\Gamma}{2}t}(q^2+1)\mathrm{e}^{\imath\omega_\mathrm{r}t}\mathrm{e}^{\imath\varphi(q)}\right]\theta(t) \tag{2.20}$$

This means the decaying autoionizing state is phase shifted with respect to an unperturbed Lorentzian line and also with respect to the instantaneous response to an excitation, i.e. the Dirac delta function $\delta(t)$. By this phase shift the profile of the Fano resonance ($\propto \Im[d(\epsilon)]$) is determined. The amplitude (q^2+1) on the other hand scales the resonant part of the Fano cross section relative to the background cross section.

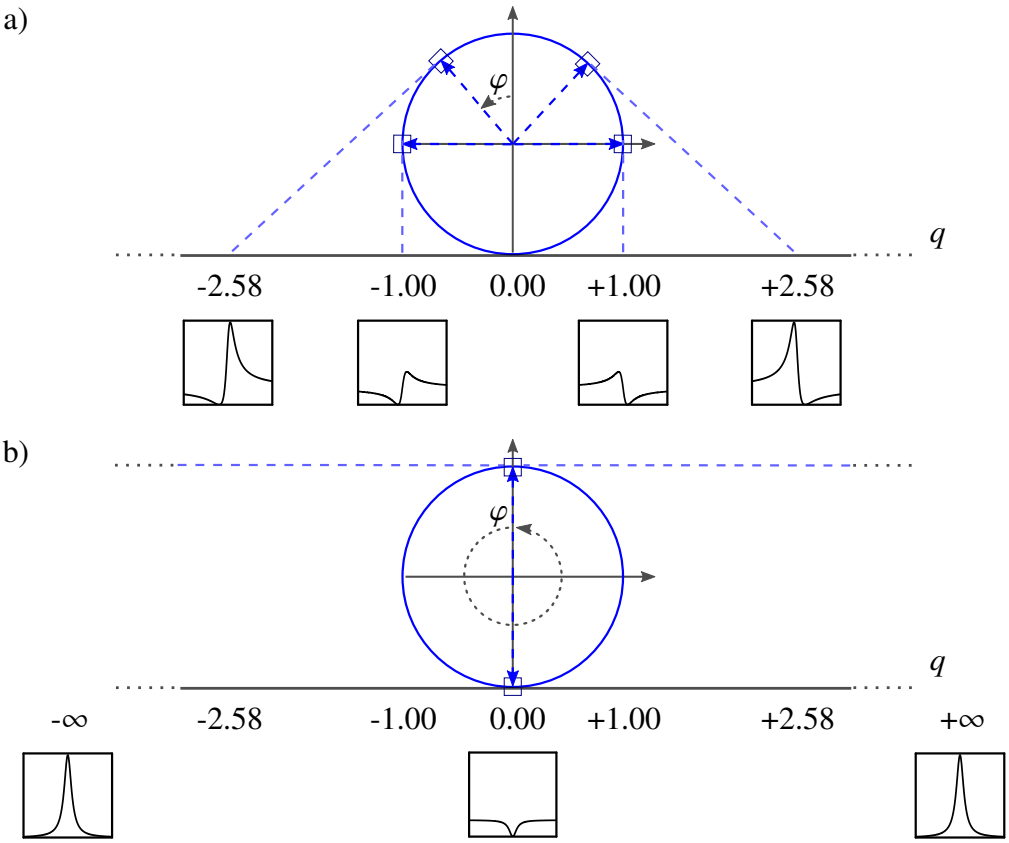

Figure 2.4: Mapping of the temporal response-function phase φ to Fano's q (line-shape asymmetry) parameter. φ starts from the vertical top point rotating in mathematical positive direction (counter-clockwise) in the (complex) plane. a) The tangents (dashed light blue lines) indicate the mapping from a given *phi* value to the horizontal q-axis. The graphs below the q-axis show the absorption line shapes $\sigma(\epsilon)$ [as depicted in figure 2.3 a)] for selected values of $q(\varphi)$. b) There are two special points. The first is the special case $\varphi = \pi$ which is a window resonance $q = 0$. The second is the point at the branch cut $\varphi = 0 = 2\pi$, which is called branch point. Lorentzian line shapes are obtained for the case of $\varphi = 0 = 2\pi$ corresponding to $q \to -\infty$ and $q \to +\infty$, respectively.

The projection is interpreted in analogy to the Riemann sphere and illustrated in Fig. 2.4. As the Riemann sphere is on top of the complex plane and every point in the complex plane is mapped to its surface, the circle is on top of the imaginary axis and every point of the circle is mapped on the horizontal imaginary (q) axis. The topmost point is assigned to $\pm\infty$. Excluding this point the mapping is isomorphic. All φ values are projected onto the horizontal q-axis. The absolute value of q per φ step increases rapidly for the upper hemisphere of the circle. The graphs below the q axis illustrate the photo-absorption cross section. The value of -2.58 has been chosen because of its importance for the measured lines, presented in chapter 4. It is the same as in Fig.2.3 a).

The phase shift φ of the dipole response function is understood as a consequence of the strong coupling between continuum states and discrete quantum states. In Fano's original work [34] this coupling was formulated in terms of the q-parameter as shown in Equ. 2.10. The reformulation first presented by our group [2], similar to the one performed recently for classical Fano resonances [59], provides a more intuitive interpretation in terms of the

dipole-response function showing the universal nature of the phase shift φ. The experimental results presented in this work are based on the fact that any phenomenon that shifts the dipole evolution of a system on the onset of the radiative decay out of phase with an initial excitation will modify the q-parameter and thus the line shape. If it is possible to control the phase shift, one controls the absorption process in general.

2.2 Perturbation Theory

In this work the Schrödinger equation needs to be solved. This is not always possible in full generality. To solve the Schrödinger equation approximately, we use perturbation theory. In the following the principle idea will be explained following the concept of the publication by Paul Dirac [60]. We start out with a time-independent Hamiltonian H that can be split into two parts, namely,

$$\mathcal{H} = \mathcal{H}_0 + \mathcal{V} \tag{2.21}$$

where $\mathcal{H}_0$ the Hamiltonian of the unperturbed system and $\mathcal{V}$ is the perturbation (and not necessarily the full potential operator) that kicks in at $t = 0$. For example, we consider a helium atom in an external laser field $\mathcal{E}_{\text{Laser}}(t)$. The position of the two electrons is denoted by r_i with $i \in [1,2]$. The unperturbed Hamiltonian $\mathcal{H}_0$ in atomic units (see appendix A) consists of the the kinetic energy $\sum_{i=1,2}(-\nabla_{r_i})/2$, the Coulomb potential due to the presence of the nucleus $\sum_{i=1,2}(-Z)/r_i$ with charge $Z = 2$ and the the Coulomb interaction between the two electrons $1/r_i$. Only that part of the potential due to the interaction with the external $\mathcal{E}$ field is represented by the perturbation $\mathcal{V} = -e \cdot (r_1 + r_2) \cdot \mathcal{E}_{\text{Laser}}(t)$.

For the unperturbed case ($\mathcal{V} = 0$) the solution of the Schrödinger equation

$$\mathcal{H}|\phi_n^{(0)}(t)\rangle = \mathcal{H}_0|\phi_n^{(0)}(t)\rangle = \imath\partial_t|\phi_n^{(0)}(t)\rangle = \omega_n^{(0)}|\phi_n^{(0)}(t)\rangle \tag{2.22}$$

are the exact eigenstates $|\phi_n^{(0)}(t)\rangle$ with the exact eigenenergies $\omega_n^{(0)}$. The eigenstates are normalized to $\langle\phi_n^{(0)}(t)||\phi_n^{(0)}(t)\rangle = \delta_{nm}$, using the Kronecker-Delta [61].

The task is to find approximate eigenvectors and eigenvalues for the case $\mathcal{V} \neq 0$:

$$\mathcal{H}|\psi\rangle = (\mathcal{H}_0 + \mathcal{V})|\psi\rangle = \imath\partial_t|\psi\rangle \tag{2.23}$$

We express the solution of the Schrödinger equation for the full Hamiltonian $\mathcal{H}$ in the base of the unperturbed system:

$$|\psi\rangle = \sum_n c_n(t)\mathrm{e}^{-\imath\omega_n t}|\phi_n^{(0)}\rangle \tag{2.24}$$

casting the trivial time dependence from $\mathcal{H}_0$ into the phase $\omega_n t$ while having the time dependent coefficients $c_n(t)$ describing the evolution of the system under the influence of the small perturbation $\mathcal{V}$.

Plugging this back into the Schrödinger equation for the full Hamiltonian Equ. 2.23 and multiplying from left with one of the basis vectors $|\phi_m^{(0)}(t)\rangle = \mathrm{e}^{-\imath\omega_m t}|\phi_m^{(0)}\rangle$ we arrive at the differential equation for the time dependent coefficients $c_m(t)$ which then reads (for a more detailed derivation see appendix B)

$$\frac{d}{dt'}c_m(t') = -\imath \sum_n c_n(t')\mathrm{e}^{-\imath(\omega_n-\omega_m)t'}\langle\phi_m^{(0)}|\mathcal{V}|\phi_n^{(0)}\rangle \tag{2.25}$$

Note that the sum runs over all numbers, explicitly also over m, so we have to solve a system of coupled differential equations. As the ability to do so strongly depends on the exact form of $\mathcal{V}$, it is generally not possible to analytically solve this problem. Now the idea of perturbation theory drops in as we can integrate Equ. 2.25 to the first order by replacing the $c_n(t')$ with their values $c_n^{(0)}$ at the time $t = 0$.

If at $t = 0$ when the perturbation kicks in only the state $|\phi_m^{(0)}(t = 0)\rangle$ is populated, the coefficient on the right-hand side of the differential equation $c_m(t = 0) = c_m^{(0)} = 1$, while all other $c_n(t = 0) = c_n^{(0)} = 0$. We relate $c_m^{(0)}$ to the time derivative of $c_m(t = 1 \cdot \epsilon \cdot t) = c_m^{(1)}$ (for a small $\epsilon \in \mathbb{R}^+$), integrate the differential equation to obtain $c_m^{(1)}$ plug $c_m^{(1)}$ into the right-hand side of Equ. 2.25 again to obtain the differential equation for $c_m(t = 2 \cdot \epsilon \cdot t) = c_m^{(2)}$ and so on. This is how Dirac developed time-dependent perturbation theory in 1927 [60]. A mathematically more strict derivation using the time evolution operator is found in [61]. In this work, we will apply the perturbation theory in order to calculate the population of (atomic) states after their interaction with a light field. We start with the most simple system.

2.3 Two-Level System

We suppose it is possible to isolate two states of an atom. A two-level systems is the most simple (non-trivial) quantum system that exists. It is described by two coupled linear differential equations. A comprehensive and detailed description is found in [62]. The solution for the Hamiltonian $\mathcal{H}_0$ of the two-level system without external forces consists of two independent states $|\phi_0(t)\rangle = \mathrm{e}^{-\imath\omega_0 t}|0\rangle$ and $|\phi_1(t)\rangle = \mathrm{e}^{-\imath\omega_1 t}|1\rangle$, which form a complete basis. Note, that $|\phi_0(t)\rangle$ and $|\phi_1(t)\rangle$ have different parity, allowing for dipole transitions between them. Figure 2.5 gives an illustration of the two level scheme with a dipole transition between the two states (violet arrow). When the two-level system is interacting with an external electromagnetic field $\mathcal{E}_{\mathrm{em}}(t)$, we can use the perturbation theory approach for weak fields to solve the Schrödinger equation. Using Equ. 2.24 we can write the wavefunction in the basis of the system without the electromagnetic field

$$|\psi\rangle = c_0(t)\mathrm{e}^{-\imath\omega_0 t}|0\rangle + c_1(t)\mathrm{e}^{-\imath\omega_1 t}|1\rangle \tag{2.26}$$

When at $t = 0$ we assume all population in the lower state, i.e. $c_0(t = 0) = c_0^{(0)} = 1$ and $c_1(t = 0) = c_1^{(0)} = 0$, we calculate the first order perturbation theory term (see Equ. 2.25) by integrating

$$\frac{\mathrm{d}}{\mathrm{d}t'}c_1^{(1)}(t') = -\imath c_0^{(0)}\mathrm{e}^{-\imath(\omega_0-\omega_1)t'}\langle 1|\Big(-e\cdot r\cdot\mathcal{E}_{\mathrm{em}}(t')\Big)|0\rangle \tag{2.27}$$

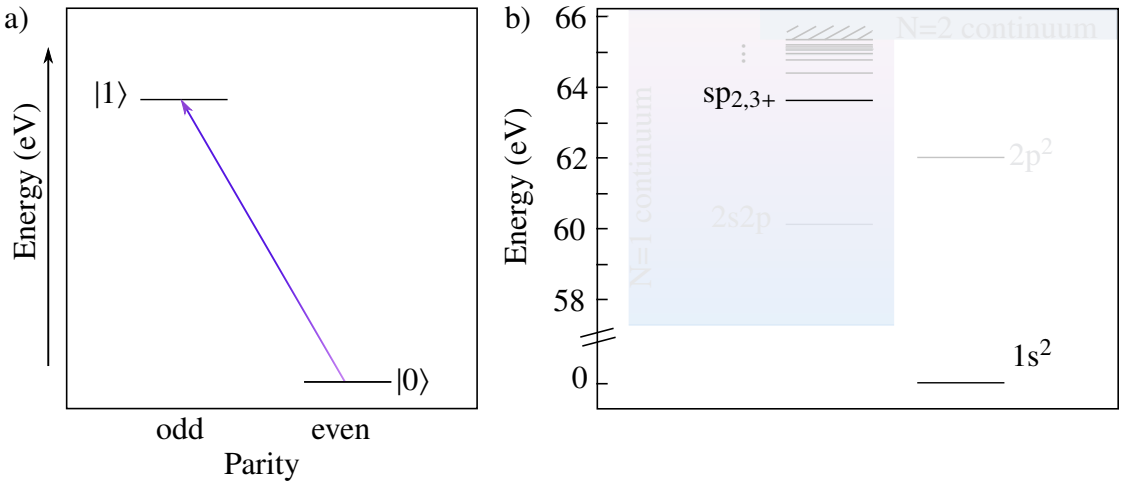

Figure 2.5: a) Illustration of the two-level scheme with a dipole transition. In horizontal-direction the states are separated by their parity, while the vertical axis shows the energy of the states. The coupling between the two states by an external electromagnetic field is depicted by a violet arrow. b) Energy diagram for helium in the range of the doubly excited $sp_{2,n+}$ series (see section 2.5), which is of major importance for this work. To emphasize the analogy to the two-level model, only the ground state $1s^2$ and the doubly-excited $sp_{2,3+}$ state are drawn, while the other states are faded out.

with the perturbation $\mathcal{V} = -e \cdot r \cdot \mathcal{E}_{\text{Laser}}(t)$. to

$$c_1^{(1)}(t) = -\imath\mu_{10} \int_{\infty}^{t} \mathcal{E}_{\text{em}}(t') \mathrm{e}^{-\imath(\omega_0-\omega_1)t'} \mathrm{d}t \tag{2.28}$$

with the dipole transition matrix element $\mu_{01} = \langle 1|(-e \cdot r)|0\rangle$.

Under the interaction with the electric field a dipole moment $\tilde{d}(t)$ is induced between the two levels, which is also called atomic polarization $P(t)$. We will later use this time-dependent dipole response $\tilde{d}(t)$ of the excited system, which is obtained via the expectation value of the dipole moment operator

$$P(t) = \tilde{d}(t) = \langle \psi^{(1)}(t)|(-er)|\psi^{(1)}(t)\rangle = \left(c_0^{(1)}(t)\right)^* c_1^{(1)}(t) \cdot \mu_{10} \mathrm{e}^{\imath(\omega_0-\omega_1)t} + c.c. \tag{2.29}$$

Note, that factor $\left(c_0^{(1)}(t)\right)^* c_1^{(1)}(t)$ and its complex conjugate represent the off-diagonal elements of the density operator $\rho^{(1)} = |\psi^{(1)}(t)\rangle\langle\psi^{(1)}(t)|$. In this work, we observe the emission by the decay of the induced polarization. The excited states couple to the electromagnetic vacuum modes and decay spontaneously. We apply the Weisskopf-Wigner theory of spontaneous emission [63] between two atomic levels and approximate the probability amplitude for spontaneous emission by

$$\frac{\mathrm{d}}{\mathrm{d}t'} c_1^{\text{se}}(t) = -\frac{\Gamma}{2} c_1^{\text{se}}(t) \tag{2.30}$$

$$\tag{2.31}$$

with the decay constant $\Gamma = {}^4\!/_3(\omega_1^3 \mu_{01}^2) = {}^1\!/_{\tau_{\text{life}}}$ and the life time τ_{life}. As a result of this differential equation the excited states decay exponentially.

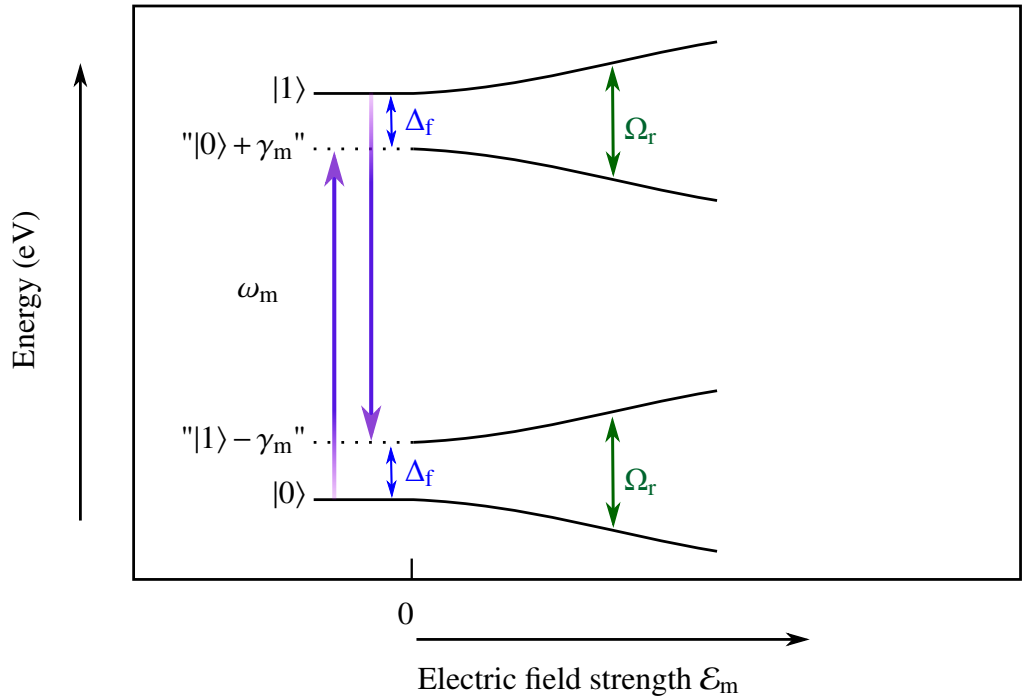

Figure 2.6: Illustration of the two-level system under influence of an off-resonant electromagnetic field (violet arrow) with frequency ω_m. The vertical axis shows the energy of the states, while the horizontal axis shows the absolute electric field strength of the external field. The parts left of $\mathcal{E}_m = 0$ are only to illustrate the field free case and the energy position of the virtual levels "$|0\rangle + \gamma_m$" and "$|0\rangle - \gamma_m$". The detuning Δ_f between the states is depicted by a blue arrow. The Rabi splitting Ω_R proportional to the peak electric field strength is illustrated by a green arrow.

Up to now, we only considered a perturbative description of the system's interaction with a weak electric field. If the field strength increases, the approximation of $c_0(t) \approx 0$ for all times t breaks down, as a significant fraction of the population is transferred back and forth between the two states. This behavior is commonly known as Rabi oscillations [64, 65]. The frequency Ω_R of such a Rabi oscillation the atomic transition between the states $|0\rangle$ and $|1\rangle$ in monochromatic driving field $\mathcal{E}_m$ is defined as

$$\Omega_R = \mu_{01} \cdot \mathcal{E}_m \tag{2.32}$$

This so-called Rabi frequency is a measure of the fluctuation of population between the states.

Furthermore, the energy levels start to mutually repel each other and shift in energy when they are strongly coupled[5] with the electric field (see Fig. 2.6). This effect is known in various fields of physics, for example as Rabi splitting [66], the Autler Townes effect [67] or AC Stark splitting. Additionally the electric field can be detuned, i.e. slightly off the resonant transition $\omega_{10} = \omega_1 - \omega_0$ between the two states. For a electric field which has a detuning $\Delta_f = |\omega_m - \omega_{10}|$ from the resonance frequency, the energy splitting ΔE is

[5]The situation becomes more complicated if the field strength increases further and the Rabi frequency $\Omega_R \propto \mathcal{E}_m$ becomes comparable to (or even larger than) than the transition frequency ω_{10}. However, this so-called ultra-strong coupling regime lies beyond the scope of this work.

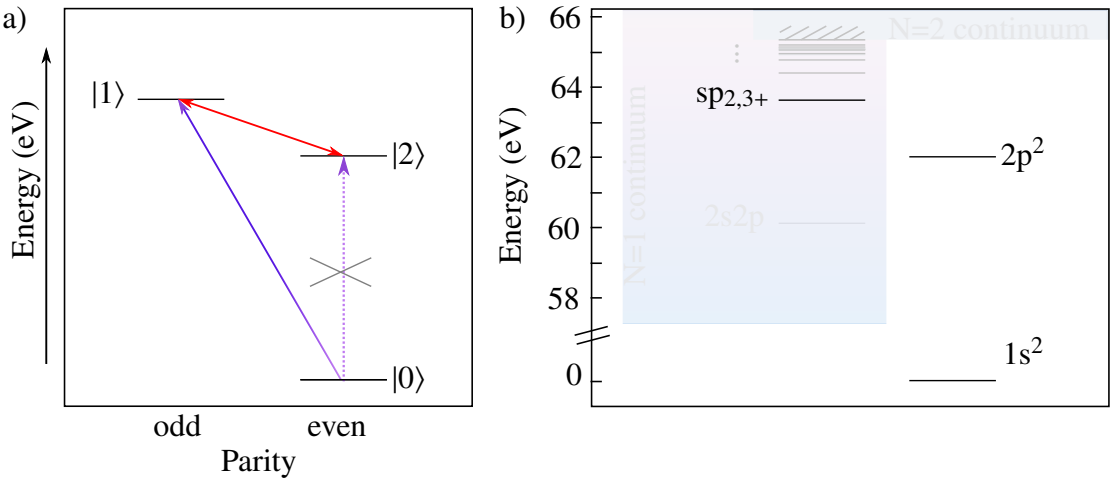

Figure 2.7: a) Illustration of the three-level scheme with a dipole transition. In the horizontal direction the states are separated by their parity, while the vertical axis shows the energy of the states. The coupling between the two states by an external electromagnetic field is depicted by a violet arrow.Doubly-excited states of helium and the embedded 3-level laser-coupled system. The XUV pulse coherently excites the dipole-allowed $|1\rangle$ ($\hat{=}$ $sp_{2,3+}$) state (violet arrow), while the energetically intermediate $|1\rangle$ ($\hat{=}$ $2p^2$) state cannot be accessed from the ground state $|0\rangle$ ($\hat{=}$ $1s^2$). The $|1\rangle$ state is resonantly coupled to the $|2\rangle$ state by the VIS pulse (red arrow). b) Energy diagram for helium in the range of the doubly excited $sp_{2,n+}$ series (see section 2.5). Similar to Fig. 2.5, the ground state $1s^2$ and the two doubly-excited states $sp_{2,3+}$ and $2p^2$ are drawn to emphasize the analogy to the three level model, while the other states are faded out.

calculated as

$$\Delta E = \Delta_f \pm \sqrt{\left(\Delta_f^2 + \left|\Omega_R\right|^2\right)} \tag{2.33}$$

The details of the derivation of Rabi oscillations and splitting for a two level system are subject of many physics textbooks [53, 62, 68, 69] and shall not be repeated here in detail. Instead we extend the scheme to more levels, approaching the case of helium.

2.4 Three-level Systems

In this section a three-level atom is considered. To this end, we introduce an additional state $|\phi_2(t)\rangle = e^{-i\omega_2 t}|2\rangle$, energetically between the states $|\phi_0(t)\rangle$ and $|\phi_1(t)\rangle$, i.e. $\omega_0 < \omega_2 < \omega_1$. Figure 2.7 illustrates the 3 levels. Note, that we use an unusual labeling for the states, as we will later map these states onto the helium atom and for consistency apply the labeling convention used later in this work. This system is a so called Ξ system, as illustrating the 3-level system without regarding the parity resembles the Greek letter.

As introduced in the previous section, $|\phi_0(t)\rangle$ and $|\phi_1(t)\rangle$ have different parity, allowing for dipole transitions between them. We chose the state $|\phi_2(t)\rangle$ to have the same parity as

the state $|0\rangle$ allowing for dipole transitions between $|\phi_1(t)\rangle$ and $|\phi_2(t)\rangle$. As the transition frequency ω_{12} differs from ω_{10}, we now use a second light field to investigate the coupling between states $|\phi_1(t)\rangle$ and $|\phi_2(t)\rangle$.We assume the second light field (red arrow in Fig. 2.7) to be applied a with a time delay τ to the first one (violet arrow). As in the previous section, we describe the wavefunction in the basis of the system without electromagnetic field:

$$|\psi\rangle = c_0(t)\mathrm{e}^{-\imath\omega_0 t}|0\rangle + c_1(t)\mathrm{e}^{-\imath\omega_1 t}|1\rangle + c_1(2)\mathrm{e}^{-\imath\omega_2 t}|2\rangle \tag{2.34}$$

The Hamiltonian contains two different electric fields

$$\mathcal{H} = \mathcal{H}_0 + \mathcal{H}_I = \mathcal{H}_0 - e\mathcal{E}_{\mathrm{XUV}}(t)r - e\mathcal{E}_{\mathrm{VIS}}(t,\tau)r \tag{2.35}$$

where in anticipation of the experiments presented in this work, the electric field coupling the states $|\phi_0(t)\rangle$ and $|\phi_1(t)\rangle$ is named $\mathcal{E}_{\mathrm{XUV}}(t)$ and the electric field coupling the states $|\phi_1(t)\rangle$ and $|\phi_2(t)\rangle$ is named $\mathcal{E}_{\mathrm{VIS}}(t)$. $\mathcal{H}_0$ is the Hamiltonian of the system without the electromagnetic fields.

As we now consider two light fields at different times, we can split the integral in two subsequent steps for calculating the coefficients. Starting from the ground state, in the first step we transfer population only to state $|\phi_1(t)\rangle$. After time delay τ the second electric field $\mathcal{E}_{\mathrm{VIS}}(t)$ couples the states $|\phi_1(t)\rangle$ and $|\phi_2(t)\rangle$. We use perturbation theory to solve it, resulting in an effective second order perturbation theory.

2.5 The Helium Atom

In this work, the response of matter to interaction with light is investigated. In the previous sections we started our theoretical descriptions with the most simple two- and few-level systems to develop a deeper understanding of this light–matter interaction. These systems form the basis for the later presented formalisms. To experimentally observe the predicted effects, we also need the most simple system, to eliminate complicated many-electron interactions. On the other hand it is of major importance for the understanding of electron correlation effects to have at least two electrons interacting. Both requirements are fulfilled for the helium atom. As we use the XUV light from the HHG process to populate exited states in helium, we mostly discuss resonances of $^1\mathrm{P}^\mathrm{o}$ symmetry[6], which are accessible via one photon transitions from the ground state. We use the spectroscopic nomenclature to address the different states. The ground state is denoted by $1\mathrm{s}^2$.

For photon energies between the first dipole-allowed excited state at 21.22 eV = 0.78 a.u. the first ionization threshold at an energy of 24.59 eV = 0.90 a.u. only one electron is excited from the ground state, the principal quantum number $N = 1$. In this work we will

[6] In the Russell-Saunders term symbol notation [70], P is the total angular momentum quantum number and the superscript 1 refers to the multiplicity, which is $(2\mathrm{S}+1)$ for the total spin S of the atom, while "o" (odd) denotes the parity of P. The ground state has a symmetry of $^1\mathrm{S}^\mathrm{e}$.

mostly refer to the dipole-allowed transitions of the excited electron into the p-state. The singly excited resonance series is denoted by their subshells 1snp for subshell $n = 2, 3, 4, \ldots$ and converges towards the $N = 1$ threshold (see Fig. 2.8). Their energy position as well as the line width up to $n = 8$ is included in Tab. 2.1. As all 1snp states are unperturbed in their decay, they exhibit a symmetric Lorentzian line shape, corresponding to an asymmetry parameter of $q = \infty$.

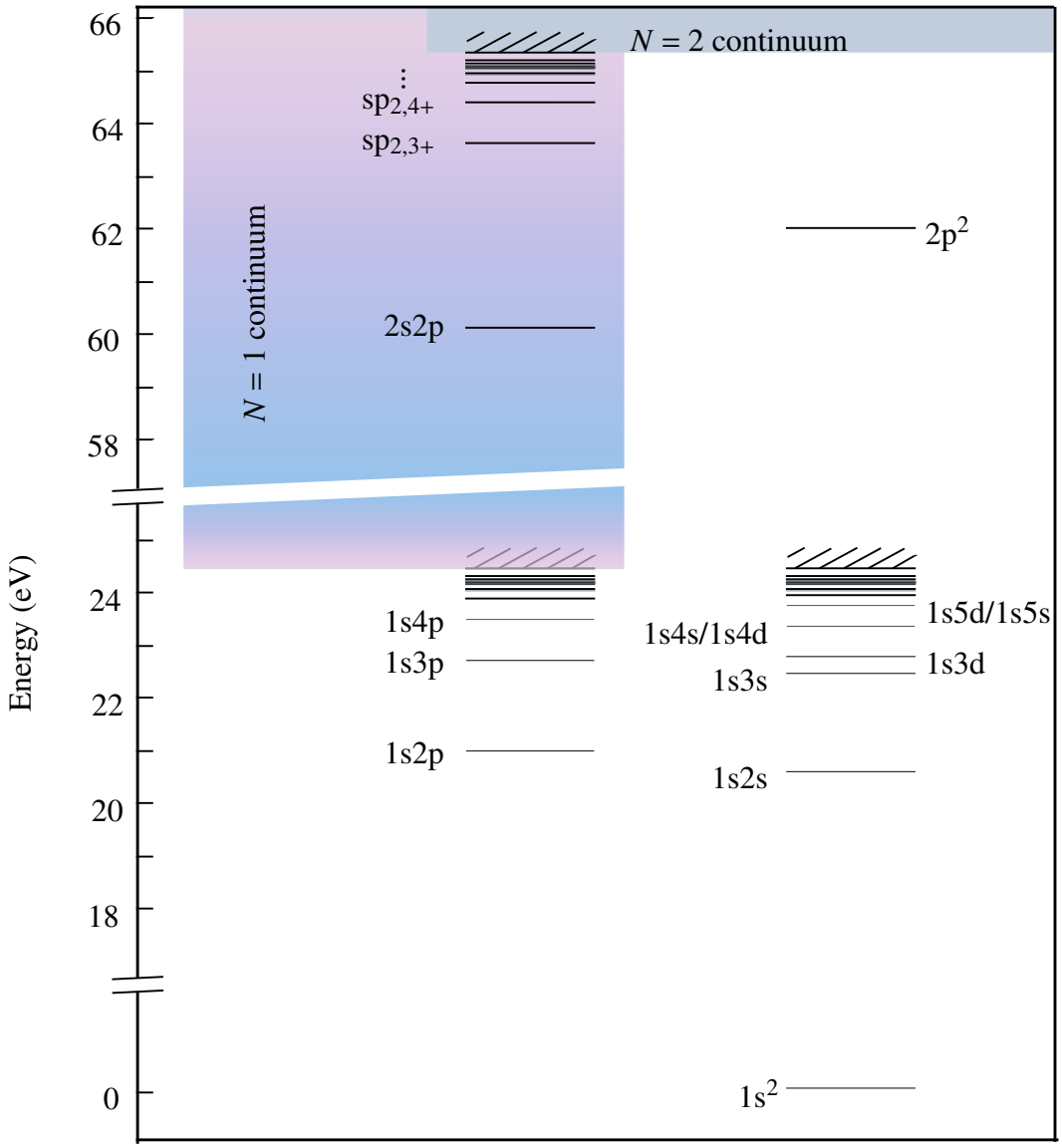

Figure 2.8: Level scheme for helium up to the $N = 2$ ionization threshold. All states are placed in their relative energy spacing. Note the two axis breaks around 16 eV and 26 eV. On the left-hand side are states that favor dipole-allowed transitions from the ground state. In the experiment described below, these states are accessible by the XUV excitation. On the right-hand side are states with a different symmetry which can be experimentally coupled by one VIS photon to the states excited by the XUV. At 24.59 eV the first ionization threshold is reached. All states above this energy are embedded in the $N = 1$ continuum (also the $2p^2$ state). Energy position taken from [28, 71, 72].

Series	Configuration	Energy (eV)	Γ (meV)	q
N=1	1s2p	21.2180	0.0074	$-\infty$
	1s3p	23.0870	0.0023	$-\infty$
	1s4p	23.7421	0.0010	$-\infty$
	1s5p	24.0458	0.0005	$-\infty$
	1s6p	24.2110	0.0003	$-\infty$
	1s7p	24.3107	0.0002	$-\infty$
	1s8p	24.3755	0.0001	$-\infty$
N=2	1s2p	60.147	37.4	−2.77
	$sp_{2,3+}$	63.658	8.2	−2.58
	$sp_{2,4+}$	64.466	3.5	−2.55
	$sp_{2,5+}$	64.816	1.8	−2.54
	$sp_{2,6+}$	65.000	1.0	−2.53
	$sp_{2,7+}$	65.110	0.7	−2.52
	$sp_{2,8+}$	65.179	0.4	−2.58

Table 2.1: Tabulated values for the 1snp singly excited series and the $sp_{2,n+}$ doubly excited series of helium. Data for the singly excited states are taken from NIST [71]. Values for the doubly excited states are extracted from [28]. See also Tab. C.2 and C.3.

For certain photon energies above 60.15 eV = 2.21 a.u. there are two possirbilities. Either one electron is ionized and takes away the energy difference to the $N = 1$ ionaization threshold or both electrons are excited to higher states. These doubly excited states in helium can be classified by the shell notation using the principal quantum number $N = 2$ for the shell and then denote the subshells, resembling the uncorrelated product of single-electron orbitals.

There are three dipole allowed $N = 2$ resonance series, namely 2snp, 2pns and 2pnd [73], which converge to the $N = 2$ ionization threshold at 65.40 eV = 2.40 a.u.(see Fig. 2.8), where one electron leaves the ion core and the other one is left in an excited state. For this work we only consider the 2snp and 2pns series, as their photo-absorption cross section is much larger then the one of the 2pnd series[7]. As the states of the 2snp and 2pns series are energetically degenerate, we describe the corresponding states as a superposition via

$$sp_{2,n\pm} = \frac{1}{\sqrt{2}}(2snp \pm 2pns) \tag{2.36}$$

[7]The 2pn series involves no s subshell and is more unlikely to be excited as both electrons have to exchange angular momentum with the radiation field. In fact, it has be observed [74,75] more than 30 years after the others [26].

where the "+" states belong to the stronger (larger photo-absorption cross section)series and the "-"states belong to the weaker series. In this work we mainly focus on the stronger $sp_{2,n+}$ states. The autoionization life times $\tau_{\text{life}} = 1/\Gamma$ fall within the range between 17 fs for the lowest 2s2p state and hundreds of femtoseconds for the highest $sp_{2,n+}$ state. The energy position, line widths and the Fano asymmetry parameter describing the line shape of each state are listed in Tab. 2.1. The energy data for the $N = 1$ series are taken from the NIST data base and references therein [71,76] where they are given in a precision of neV, much better than the precision needed for these experiments (meV). Values have been rounded to match the necessary precision. The lifetime data are taken from [77, 78] and [79] in [80]. The data for N=2 are taken from [28]. As mentioned in the introduction of this thesis, in their comprehensive publication Rost, Schulz, Domke and Kaindl conclude [28]:

> It turns out that the q-parameter is a much more sensitive probe of the dynamics than the resonance positions and even the widths.

Therefore it is very important to have a spectrograph powerful enough to resolve even small changes in the q-parameter, respectively in the line shape.

2.6 Ultra-Short Laser Light Sources for the Coupling of States

In this work we consider dynamical processes on the time scale of a few femtoseconds or less. As the interaction is of electromagnetic nature it is not far to seek the help of laser light to probe and control the interaction. To achieve this high temporal resolution, we need ultrashort laser pulses to prevent the time information from being smeared out. The term ultrashort light pulses generally refers to time durations of below one picosecond. As the bandwidth $\Delta\omega_{\text{Laser}}$ for a dispersionless Gaussian pulse is the Fourier transform of its duration $\Delta\tau$, such pulses have a broadband spectrum. To achieve the formation of a short pulse out of a broad spectrum it is necessary that all the modes are locked, i.e. they have a fixed phase relation, as illustrated in Fig. 2.9. The peak intensities are extremely high for these short pulses, for example the laser pulses used in this work can reach a peak intensity[8] of $\approx 3.5 \cdot 10^{15}\,\text{W/cm}^2 = 3.5\,\text{PW/cm}^2$. No gain medium in a laser can stand such intense pulses. Therefore these high power pulses are created in steps. A mode-locked oscillator produces a broad spectrum and a short pulse. This pulse is then amplified using the technique of chirped pulse amplification[9] [82].

The traditionally most successful gain medium for such ultrashort pulsed lasers is a titanium doped sapphire (Ti:Al_2O_3, short Ti:Sa) crystal.

[8] For a 7 fs pulse as it is used in this work with a pulse energy of $\approx 500\,\mu$J, resulting in a peak power of 70 GW, focused on a spot of 50 μm diameter

[9] Chirped pulse amplification was first introduced for radar in 1960 [81] then adapted for high power optical lasers in 1985 [82]

2.6.1 Compressed Ti:Sa Pulses

The first operation of the Ti:Sa laser was reported by Moulton in 1982 [83]. These solid-state lasers were first used in continuous wave (cw) mode and with external mode-locking techniques with pulse durations in the picosecond regime. That the Ti:Sa- amplification bandwidth allows the formation of pulses with pulse durations of a few femtoseconds when all the modes are locked, is illustrated in the comparison of Fig.2.9 a) and b). As not the whole bandwidth is amplified with the same efficiency, the bandwidth is convoluted with a Gaussian envelope, still producing a few-femtosecond pulse in the mode-locked operation [see Fig. 2.9 d)]. With the discovery of the Kerr-lens mode locking inside the Ti:Sa crystal [37] those pulse durations in the femtosecond regime became available. In short, the Kerr lens effect causes light with higher intensity to be focused more tightly inside the crystal. As a pulse, created by a distortion of the cw-mode, has a higher peak intensity than the latter, it will stimulate more emission than the cw-mode and clear the population inversion, thus increasing the absorption for the cw-mode. If the pump laser which creates the population inversion is focused tightly in the Ti:Sa crystal, the (by the Kerr lens effect) more tightly-focused pulsed mode is preferred compared to the cw-mode. This tendency is additionally enhanced when the cavity is at the limit of the stability range for the cw-mode. There, the Kerr lens effect stabilizes the lasing.

Ti:Sa laser systems with pulse durations around 10 fs and repetition rates from kilohertz to megahertz are commercially available since 1997 [84]. For the experiments presented in this work a commercial FEMTOPOWER compact PRO [85] chirped pulse amplifier with a subsequent KALEIDOSCOPE [86] hollow fiber compressor is used to produce 7 fs laser pulses. These pulses yield peak intensities in the $1\,\mathrm{PW/cm^2}$ regime (corresponding to electric field strength around 0.5 a.u.). The electric field which the electron in a semiclassical picture would feel in the first Bohr orbit of the hydrogen atom is 1 a.u.. Due to this high electric field strength of the laser pulse, highly non-linear effects take place when interacting with atomic systems, such as non-sequential double ionization [6, 87], high-order above threshold ionization [88] and high-order harmonic generation (HHG) [39]. The latter one is of great importance for this work. In HHG one uses the femtosecond pulse as an expedient to produce even shorter attosecond pulses, as it is described in the next section.

2.6.2 High-Order Harmonic Generation

For the generation of high-order harmonics an intense femtosecond laser pulse impinges on a gaseous target, ionizes an electron and drives it back so it can recollide with the parent ion under emission of XUV light (see Fig. 2.10). We will here explain the 3-step model for the HHG process as an overview and reminder. A mathematically more strict and detailed derivation is found in modern attosecond science literature, e.g. [90].

As explained in the previous section, such femtosecond laser foci reach peak electric field strengths on the order of half an atomic unit. This field strengths is sufficient to significantly suppress the Coulomb barrier and increase the probability for tunnel ionization of

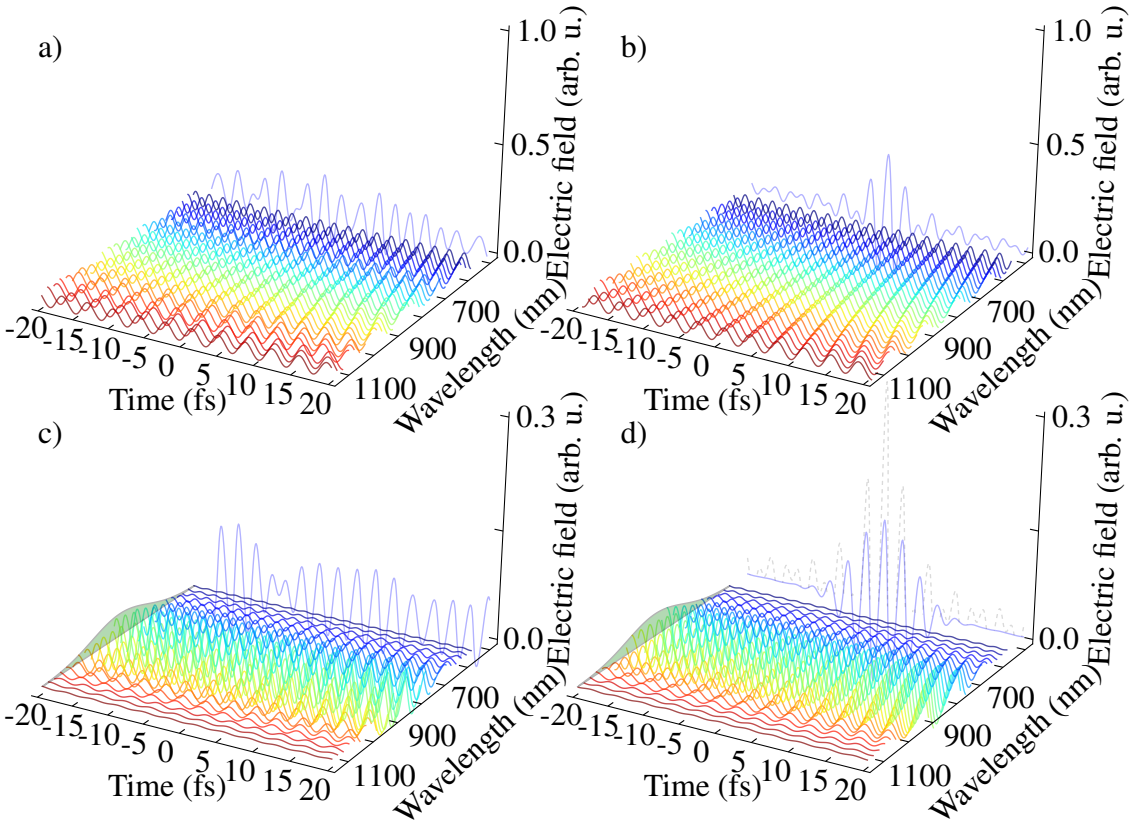

Figure 2.9: a) Oscillations between 1100 nm and 500 nm with random phase relation and unitary amplitude of 1. The sum of all modes (light-blue solid curve) is projected onto the electric-field/time plane (xz-plane). Since all phase relations are random, the pattern is noisy. b) Oscillations in the same wavelength and amplitude as in a) but in contrast to the former case all waves are in phase. The sum of all modes is projected onto the xz-plane (light-blue solid curve) and forms a short pulse with a pulse duration $\tau_{\mathrm{FWHM}} = 5.2\,\mathrm{fs}$. The maximum of the electric field amplitude of the pulse shown in the xz-projection is 0.33 arb.u.. c) Oscillations between 1100 nm and 500 nm with random phase relation but each amplitude is scaled by a Gaussian centered around 780 nm (shown in the projection on the electric-field/wavelength-plane (green filled curve). Note that to enhance visibility the z-axis range is reduced compared to a) and b). Again the sum of the unrelated waves gives a noisy pattern, which is visible in the projection on the xz-plane (light-blue solid curve). d) Oscillations in the same wavelength and amplitude as in c) but now all waves are in phase. The z-axis has the same scaling as in c). The projection on the xz-plane shows a short pulse (light-blue solid curve). For comparison the positive part of the pulse from b) is also shown in the xz-plane (light-grey dashed curve). This pulse has a duration of $\tau_{\mathrm{FWHM}} = 8.2\,\mathrm{fs}$ and is longer than the one shown in b) but shows less oscillation in the pedestal due to the tapering of the wavelength. The maximum electric field is 44% of the maximum electric field for the case shown in b).

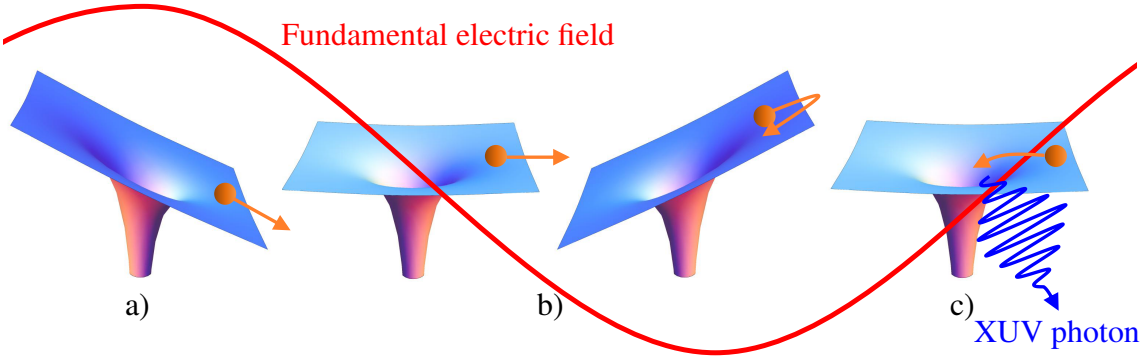

Figure 2.10: Artist's view of the three-step model for HHG. a) In the first step, an electron is extracted near the peak of a fundamental laser field. b) In this field, the freed electron is accelerated away from the ion core. When the field reverses direction the electron is driven back. c) For a linearly polarized laser field the electron passes by and can "recollide" with the parent ion leading to the emission of XUV radiation. Illustration adapted from [89]

a valence electron into the continuum. The tunneling ionization rate is essentially determined by the instantaneous field strength [91]. At the moment of ionization [see Fig. 2.11

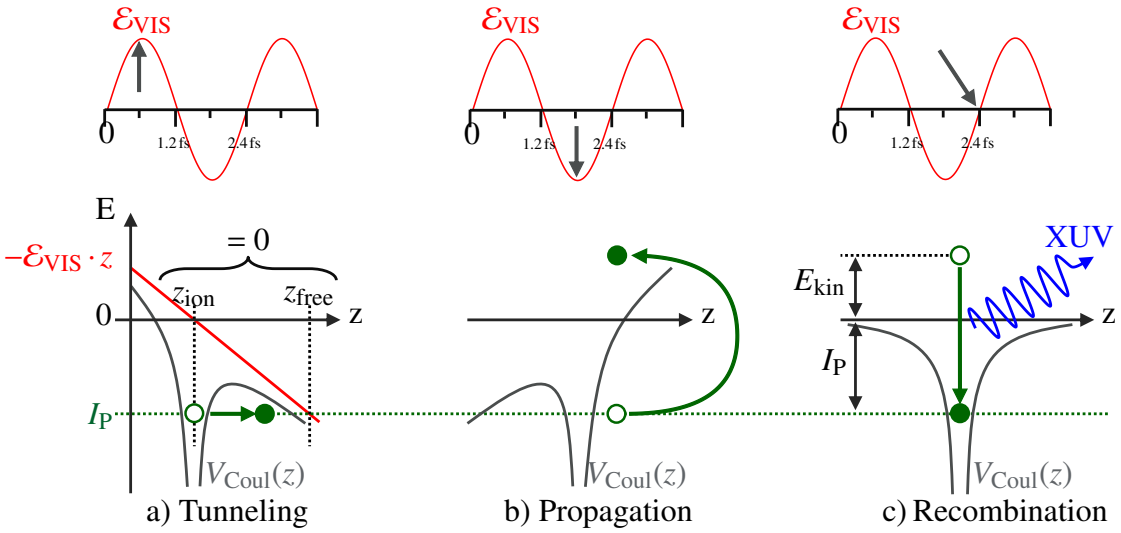

Figure 2.11: Schematic illustration of the three-step model for HHG. a) Tunneling: Near its peak field strength, the intense femtosecond VIS field $\mathcal{E}_{VIS}$ (red solid line) extracts an electron wave packet from an atom. b) Propagation: The electron propagates in the field and when $\mathcal{E}_{VIS}$ reverses, the electron is driven back. c) Recombination: The electron passes by the parent ion and can recombine leading to the emission of a XUV photon. Illustration adapted from [89]

a)] an electron appears in the continuum where it is immediately accelerated away by the strong laser field and starts to return to its parent ion, if the the electric field points into the opposite direction [see Fig. 2.11 b)]. For a linearly polarized driving field, there is a non-vanishing probability that the returning electron is recaptured by the parent ion[10].

[10] In most cases however, the free electron will oscillate in the field until the end of the pulse and not

If this is the case, the combined kinetic and binding energy is carried away by an XUV photon 2.11 c)].

As this three steps are repeated every half-cycle of $\mathcal{E}_{\mathrm{VIS}}$, high-order harmonics are emitted as light bursts with a periodicity of half the fundamental laser period [93]. Taking into account that the sign flips between successive bursts, it follows from the symmetry properties of the Fourier transform that the produced harmonic spectrum consists of the odd harmonics of the fundamental laser frequency [94, 95]. Additionally, it is found theoretically and experimentally that the intensity of the lowest order harmonics decreases apace, followed by a long plateau with equal intensities and ends in an abrupt cutoff [96]. This cutoff lies at $I_{\mathrm{p}} + 3.17U_{\mathrm{p}}$ with the field-free ionization potential of the atom I_{p} and the ponderomotive energy U_{p}, of the free electron gained by the Lorentz force in the electric field (see [90] and chapter 4.2.2).

recombine with the parent ion [92]

Chapter 3

The Multidimensional Spectroscopy Setup

The precise characterization of quantum states is at the heart of atomic and molecular physics. Different techniques including detection of photon-electrons and ions have been developed to access the properties of quantum states in various systems [97]. The very first observations of electronic levels in atoms and molecules two centuries ago were performed measuring the light absorption spectra [10, 98]. Since photons do not suffer from space-charge effects, are insensitive to stray electric or magnetic fields, and can be detected with high dynamic range using existing charge-coupled device technology, they are still the first choice for the precise characterization of bound-bound transition in atoms. To gain insight in quantum *dynamical* processes it is necessary to introduce timing information to the system. Therefore it is inevitable to have a time reference. One of the most successful measurement schemes in the last 40 years detecting photons to explore the dynamics of the system uses two light pulses in a so called pump-probe scheme where one of the two light pulses is delayed with respect to the other. The first light pulse starts a process when absorbed in the system and the second light pulse probes response of the system[1] when arriving delayed thus introducing a measurable time difference.
The essential idea of traditional time-resolved absorption spectroscopy is to start dynamics with a pulse short compared to the time scale of the system dynamics to observe its time evolution by measuring the absorbance of the system as a function of time after excitation by a second laser pulse. This transient-absorption technique is a very well-established method in other regions of the electromagnetic spectrum [99] and/or on longer timescales (e.g. [100]). It recently has been transferred to attosecond science [101–105]. In contrast to other techniques like streaking [106, 107] or stroboscopic photo-electron spectroscopy [108], where electrons are detected after changing their trajectory due to the second laser field, transient absorption spectroscopy does not require the presence of a

[1] this probing can for example be the ionization of the excited state, then information is acquired by measuring electron and/or ion **CITE** . Probing can also mean that the spectral and/or temporal profile of the pulse is changed and information of the system is gained be determine this differences.

strong laser field[2].
To gain access to the dynamical phase information of the excited system, the original transient absorption spectroscopy scheme is extended for the experiments presented in this work. In the first step an XUV light pulse passes through a gas target. The second light pulse is a visible laser (VIS) pulse. In contrast to the original transient absorption scheme this second pulse is not used to probe the absorption of the excited system, but to control the coupling to other excited (continuum) states by changing its intensity and time delay. Therefore the measured absorption spectra are not in the frequency domain of the second pulse (VIS), but in the region of the first, exciting XUV-pulse. In combination with our high-resolving XUV spectrometer even small changes in the observed line shape of the excited states are observed enabling the extraction of dipole phase changes. Since the decaying dipole is altered by the second pulse this measurement scheme is known as perturbed polarization decay (as first described by Joffre et al. [110]). Together with additional observables, controlled by macroscopic experimental parameters like pressure of the target gas, incident angle and intensity of the second light pulse a deeper understanding of the interaction between the incoming light and the atomic quantum states is achieved.
This chapter is structured as follows: **Section 3.1** gives a brief introduction into the experimental setup lining out the most important ideas and components and introducing the perturbed-polarization decay scheme. The experimental setup is then described in detail of **section 3.2**. Each of the components adding another dimension for the multidimensional spectroscopy setup is described in a separate subsection. **Section 3.2.1** expands the detail on the split mirror setup and the filter unit, enabling separation in space and time of the two co-propagating pulses. The newly build computer-controlled micro-stepper iris aperture for controlling the coupling strength between different states via the intensity of the VIS pulse is discussed in **section 3.2.2**. In **section 3.2.3** the pressure control of the target cell is described. **Section 3.2.4** presents the spectrometer including a backside illuminated XUV camera and a variable line space grating. Finally in **section 3.4** the analysis of the recorded experimental absorption spectra is carried out.

3.1 Overview of the Beamline

In the experimental setup (see Fig. 3.1) an XUV light pulse—produced in a HHG process (see Chapter 2.6.2) with a 7 fs 760 nm driver pulse—travelling in an ultra high vacuum (UHV) chamber passes through a helium gas target with variable backing pressure (see Chapter 3.2.3). The spectral range of the generated XUV pulses depend on the phase matching conditions of the HHG process and the used generation gas and can be flexibly tuned from 15 eV to 110 eV[3]. For the experiments presented in this work the singly

[2] It should be mentioned though that strong fields could still be useful, for example to create an electron-wavepacket by strong field ionization [109].

[3] Usually, not the whole range is covered at once. For neon gas with 100 mbar backing pressure in the HHG cell it is possible to achieve a continuous and barely modulated XUV spectrum, indicating a single attosecond pulse, for the energy range between 55 eV and 90 eV. Using argon with 60 mbar backing pressure as a generation gas the region between 20 eV and 70 eV is covered, but the spectrum is deeper modulated,

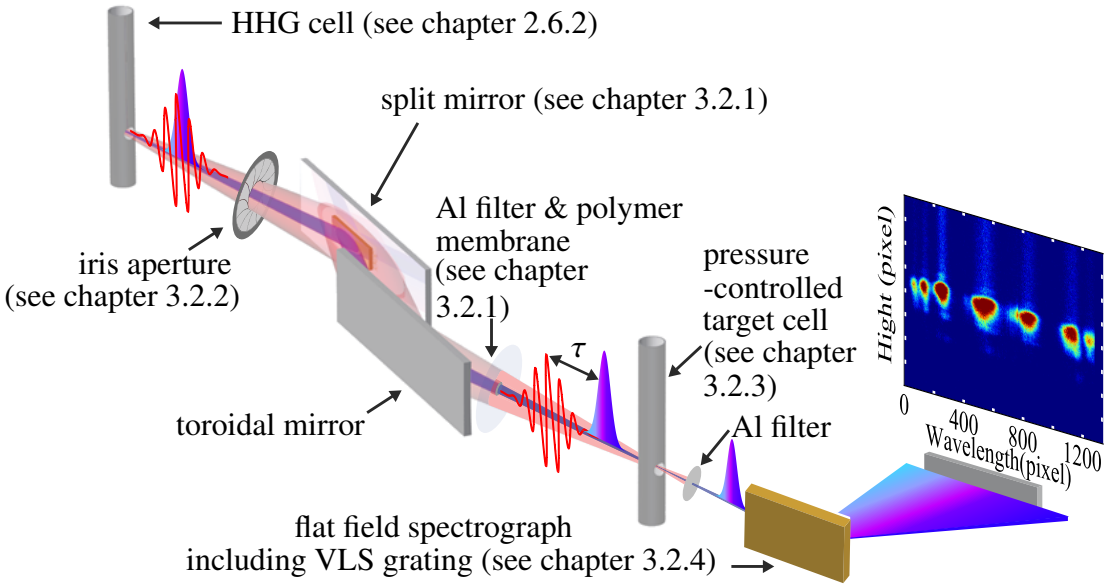

Figure 3.1: Schematic illustration of the experimental setup. All depicted components are located in an UHV chamber, reducing absorption and dispersion of the light pulses before reaching the target gas. The fundamental VIS laser pulse enters the HHG cell from the upper left corner of the picture. Both VIS and produced XUV light pulses leave the HHG cell heading towards the flat-field spectrograph in the lower right corner. They are re-focused into the pressure-controlled target gas cell by a toroidal mirror with an 1:1 imaging geometry. After the target gas cell the VIS light is completely filtered out by an thin-film metal filter. Only XUV light enters the spectrograph and is recorded on the camera after being split-up into different wavelength components.

and doubly excited states of helium are investigated demanding a spectral range between 20.6 eV for the lowest-lying state 1s2p and 65.4 eV for the double-ionization threshold. The transmission of the employed aluminum filters ranges between 18 eV and 72 eV thus covering the region of interest. During the interaction with the helium atoms the XUV light coherently excites the 1snp state resonance series and the $sp_{2,n+}$ [75] state resonance series (see chapter 2.5 and Fig. 2.8 therein). The absorption spectra are observed by using a home-built flat-field spectrometer featuring a resolution of better than 20 meV (standard deviation, see chapter 3.2.4), achieved by a variable line space (VLS) grating (see chapter 3.2.4), which is crucial to resolve small changes in the observed line shapes. In addition, a synchronized VIS laser pulse of controlled intensity, time delay and angle relative to the XUV pulse follows the XUV pulse. The VIS laser (photon energy $\hbar\omega_L \approx 1.7$ eV) couples different states to each other after the initial XUV pulse created a coherent superposition between the $1s^2 = |0\rangle$ ground state and the dipole-allowed excited states. Additionally to the observation of intensity- and time-delay-dependent changes of the absorption line shape it is also possible to scan the density of the atomic target by controlling the backing pressure, thus unveiling propagation effects and, potentially (but not observed here) coherence effects between the atoms[4]. In absorption spectroscopy, different spectral line

indicating an attosecond pulse train. With xenon at 25 mbar backing pressure a quasi-continuous spectrum is generated with a cut-off around 36 eV under our experimental conditions.

[4]Some recent publications even hint the possibility of coupling effects between different excited atoms in the gas phase [111].

shapes arise by the interference of the systems dipole response with the incoming light. By controlling the focal spot positioning of the pulses relative to each other, it is possible the send the XUV through a region with an inhomogenous VIS intensity distribution and thereby steer the re-emission of the excited target gas atoms thus separating the incoming XUV light from the emitted dipole radiation.

3.2 Multidimensional Spectroscopy: Energy, Space and Time Resolution

Transient absorption spectroscopy is not limited to scanning the time delay between the two pulses. By extending the free parameters for manipulating the system in the experiment one obtains an extensive knowledge of the the properties and the behaviour of the system under study. This has already been done for the spatial distribution of the emitted dipole radiation [112]. In the following the extension of a two-dimensional setup (time delay and energy) to a multi-dimensional setup including additionally control over the spatial electric field gradient, the average distance between two neighboring atoms and the strength of the coupling between different quantum states of the system is presented in detail.

3.2.1 Temporal Control of Split Pulses

The major control parameter to reveal time dependent processes in the experiment is the time delay between XUV and VIS pulse. To make a control of the time delay possible it is necessary to first spatially separate the pulses, as they are overlapping due to the nature of the HHG process. In our setup we take advantage of the intrinsically lower divergence of the attosecond pulses (~ 1 mrad) compared to the copropagating VIS pulses (~ 15 mrad). Approximately 70 cm behind the high harmonic generation a filter is placed that spatially separates the inner XUV pulse from the VIS pulse (see Fig. 3.2). The outer part of that filter is made of an uncoated nitrocellulose membrane. It is transparent for the VIS laser pulses with an average refractive index of 1.50 [113] and due its thickness of only 2 μm introduces a group delay of 3 fs, but only negligible dispersion. For the XUV pulses on the other hand it shows an optical density of 5 [114] resulting in a complete absorption of XUV stray light of higher divergence. To let the XUV light pass part of the polymer membrane is removed in the center. In front of this hole in the membrane the second, inner part of the filter is placed. It is composed of an aluminum foil of 200 nm thickness [115]. In the photon energy range between 18.2 eV and 72.6 eV at least half of the XUV intensity is transmitted through the Al-foil (see Fig. 3.3). By contrast, the penetration depth in aluminum for the VIS laser field is around 10 nm and therefore it is completely absorbed.
The outcome of the measured spectra depends on the amount of VIS light which still remains in the XUV beam path (this light will be called leakage) either due to micro-holes in the sub-micron metal foils or due to misalignment of the filters relative to the

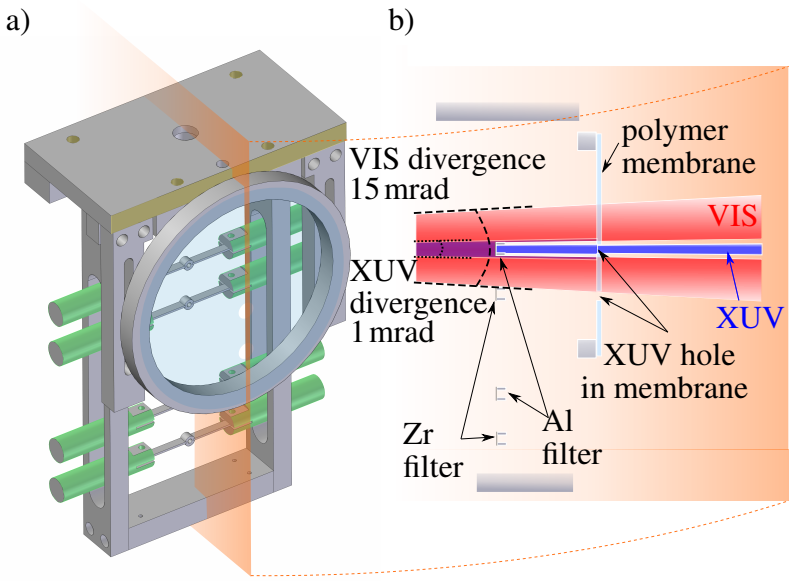

Figure 3.2: Schematic illustration of the filter setup consisting of thin-film metal filters (attached to the small grey tubes, which are connected by planks to the green cylinders) for blocking the VIS laser pulse and a polymer membrane (colored in light blue, inside the big metal ring) for blocking the XUV pulse. The polymer membrane only covers the area around the upper two thin-film metal filters. It transmits all visible light and is colored in blue for visibility in this illustration. To allow XUV light to pass the filter at the right spot, the membrane has been removed co-aligned with the small metal filters (small holes in the light-blue membrane).

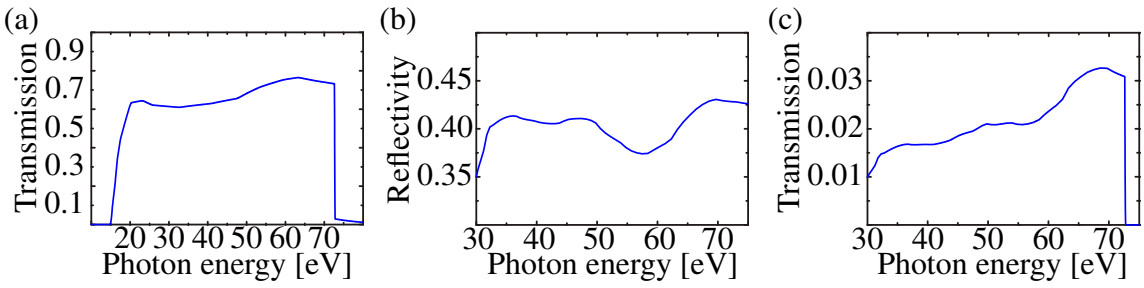

Figure 3.3: (a) The transmission of aluminum of 200 nm thickness between 10 eV and 80 eV is important for the use of thin metal foils spatially separating XUV and VIS pulse. (b) Reflectivity of gold between 30 eV and 75 eV is used to estimate the influence of the mirrors to the spectrum. (c) The overall transmission for an XUV pulse starting from the high-harmonic generation cell to the XUV-CCD-camera, taking into account three reflections from gold surfaces on glass (inner mirror, toroidal mirror and spectrometer grating) and transmission through three 200 nm-layers of aluminum. The amplitude of the recorded spectra exactly follows this envelope. All data exported from [114]

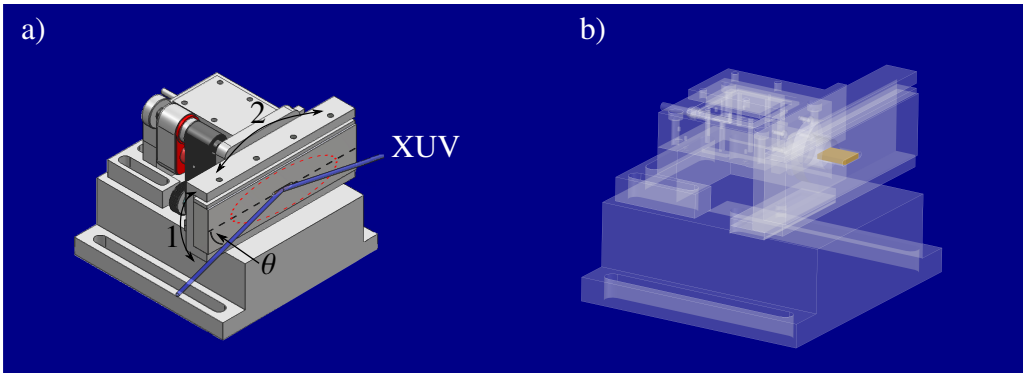

Figure 3.4: a) Schematic illustration of the grazing-incidence split-mirror setup. The grazing incidence angle θ is market. The outer mirror is mounted on a piezo-driven tip-tilt platform which can be tilted around the horizontal axis (1) and the vertical axis (2) to steer the VIS beam. The VIS beam diameter on the mirror is depicted as red dotted line. The gold coated, piezo-controlled inner mirror reflects the XUV beam (blue solid line) and is highlighted in yellow in subfigure b) on a blueprint illustration of the grazing-incidence split-mirror setup.

beam such that light passes by on the side of the filters. Therefore, the placement of the filter unit in the exact center of the XUV beam is crucial and will be described here in a bit more detail. This placement is checked separately for the horizontal (x) and the vertical (y) direction. Since the XUV camera shows the spatial distribution of the HHG light in y-direction the alignment is oriented on the edges of the aluminum filter, which appear as dark stripes on the illuminated camera. The y-axis movement of the filter is controlled by a ultra-high vacuum (UHV) linear translator. In x-direction the XUV camera observes the wavelength-separated spectrum from the grating. The only control parameter for the alignment are changes of the natural line shape due to leakage of the VIS laser pulse. These line shape modifications are minimized by precisely aligning the filter in x-direction with a picomotor.

Having discussed in detail the spatial separation of the pulses, now the temporal separation is described. We use a gold-coated mirror for the XUV on a piezo-positioning device [116] to manipulate its beam path length and change its arrival time at the target relative to the arriving time of the VIS laser pulse. A schematic view of the gold-coated movable mirror (inner mirror) sitting embedded in a large silver-coated mirror (outer mirror) with fixed transversal position is shown in Fig. 3.4.

Mechanical fluctuations of the inner mirror induced by external (e.g. vibrations from the vacuum pumps) or internal disturbances (e.g. fluctuation in the piezo positioning) lead to geometrical changes of the beam path, induce timing jitter and and uncontrollably change the overlap of the two foci. To determine these instabilities a helium-neon laser was coupled into the system and one part was reflected off the movable inner mirror and the other part of the fixed outer mirror. By recombining the two beams, focusing on a photo diode and monitoring the intensity modulations the interferometric stability was determined to be on the order of 10 as (root-mean square error) rms-noise. This is only a factor of five higher than the theoretical limit of 2 as for the typical 1 nm accuracy of the piezo-positioning device [116]hitting the mirror under 15° gracing incidence.

3.2.2 Intensity Control of the Coupling Pulse

The intensity of the VIS laser pulse in the experimental interaction region is another major control parameter of this time-resolved absorption experiment. In the first part the control of the absolute value of the intensity is described. This control is realized using a home-built motorized zero-aperture iris. The iris precisely controls the beam diameter of the

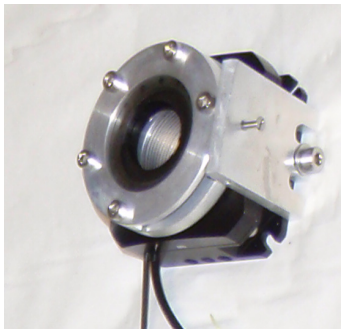

Figure 3.5: Photographic picture of the motorized zero-aperture iris used in the setup presented in this work. With the iris mounted on the 0.035 mrad step size motor the beam diameter of the divergent VIS pulse can be controlled with high precission.

divergent VIS pulse and thus the focus size after re-focusing with the toroidal mirror into the target gas cell. A photographic picture is shown in Fig. 3.5. The iris aperture is centered around the combined XUV and VIS beam path after the attosecond pulses are generated. To control the opening of the aperture during vacuum operation a modified closed-loop rotation mount [117] is used enabling reproduction of iris positions with a precision of 0.035 mrad. The opening of the iris is controlled by the angle of the rotation stage. Consequently, the minimum intensity step size of the iris is below the shot-to-shot rms of the intensity fluctuations of the laser system. The VIS intensity calibration is done in situ using the Autler-Townes splitting of the helium 2s2p state (see Chapter 2.3 and 3.4.2, respectively). For future work an intensity calibration using the attosecond streak camera technique [107, 118] is envisaged.

Having discussed the control of the absolute value of the VIS intensity, in the following the control of the spatial homogeneity of the intensity is described. An inhomogeneous intensity distribution is used to separate the atoms response from the excitation pulse. The observations and effects resulting from this separation are subject of chapters 4.1.1 and 4.3 while the experimental realization will be discussed here. As long as the VIS pulse is centered around the preceding narrow XUV pulse, all atoms which are excited by the XUV pulse will be exposed to nearly the same VIS intensity [see Fig. 3.6 a)]. When the VIS beam path is slightly displaced from the center the XUV beam path and the excited atoms experience a spatial gradient of the VIS intensity distribution [see Fig. 3.6 b)]. Slightly rotating the silver-coated outer mirror around its vertical and horizontal axes (see Fig. 3.4) changes the angle of the VIS pulse reflected from the outer mirror and thus its focal position in the target gas cell. The sensitivity for the displacement of the VIS beam increases with decreasing VIS focus diameter. Therefore, the inhomogeneity is larger with larger iris opening. The focus spot size of the VIS pulse for a iris opening

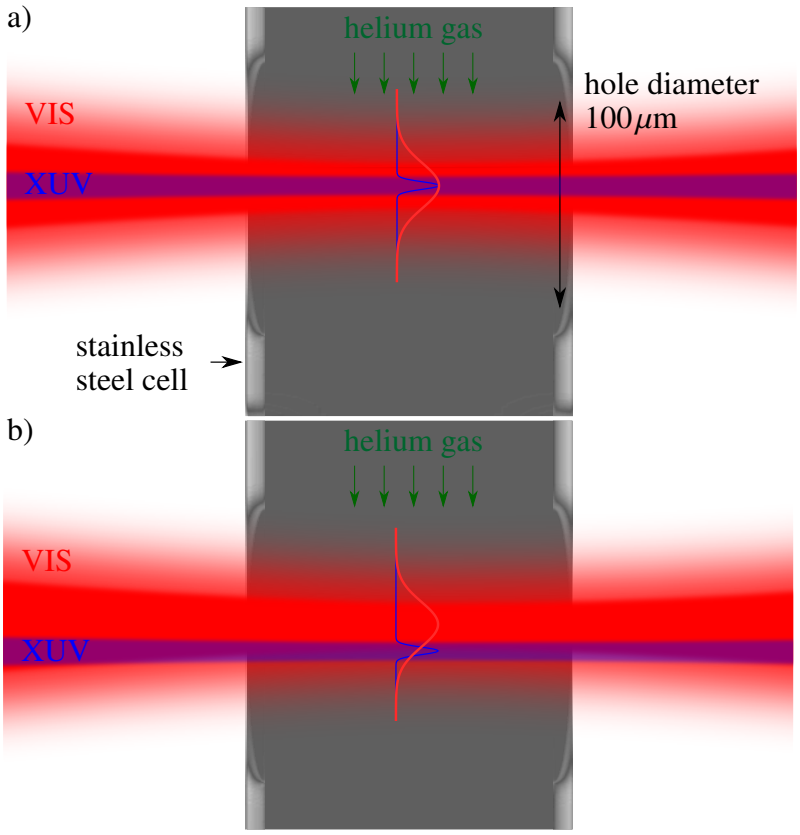

Figure 3.6: a) XUV (blue) and VIS (red) beam paths passing the target gas cell (grey cylinder) through a hole of only 100 μm diameter. The stainless steel target gas cell provides helium with backing pressures between 30 mbar and 100 mbar. The VIS beam is centered around the XUV beam creating a nearly homogenous intensity distribution [indicated by the broad vertical Gaussian profile (red, solid line)] around the atoms excited by the XUV [indicated by the narrow vertical Gaussian profile (blue, solid line)]. b) Here the VIS beam path is moved upwards relative to the XUV path by rotating the outer mirror of the split mirror setup around its horizontal axis (see 3.4). Now the atoms excited by the XUV and located in the rising edge of the VIS intensity distribution are exposed to an inhomogeneous intensity distribution [indicated by by the narrow vertical Gaussian profile on the rising edge of the broad vertical Gaussian profile].

of 50% is around 50 μm. The spot size of the XUV beam is on the order of a few μm. For a complete opening of the iris some inhomogeneity effects can already occur for no displacement since the VIS focus is only a few tens of μm.

3.2.3 Pressure Control of Target Gas

The target gas is provided by a 2 mm inner-diameter stainless-steel tube with 100 μm diameter holes in order to let the focused co-propagating beams pass through (see Fig. 3.6). To achieve high optical densities and thus good spectroscopic contrast, high target gas pressures are required. By contrast, low pressure is preferred to avoid propagation effects. In helium for the doubly-excited states, a good compromise for this tradeoff is a backing

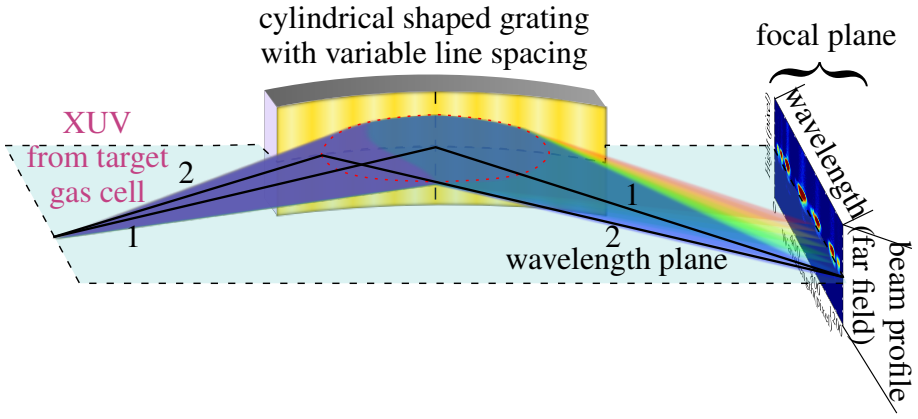

Figure 3.7: The XUV beam (purple) is diverging after the target gas cell and enters the spectrometer after passing another thin-film metal filter. The cylindrical VLS grating focuses the split-up wavelength onto the charge-coupled device (CCD) camera chip. The horizontal axis of the camera shows the wavelength spectrum of the XUV light while the vertical axis shows the beam profile of the XUV beam. Two beam paths (marked 1 & 2) of the short wavelength (blue beam) are drawn. Number 1 reflects of the center of the grating while number 2 reflected of the left hand side. The dotted red circle represents the are of the VLS grating which reflects the XUV beam.

pressure between 30 mbar and 100 mbar corresponding to at least $\sim 0.2\,\mathrm{mbar\,l/s}$ of gas leaking into the chamber. With our 2000 l/s turbomolecular pump it is possible to maintain a pressure of 10^{-5} mbar in the vacuum chamber, for backing pressures up to 300 mbar. This represents the upper limit for pressure-dependent measurements. The lower limit is given by the possibility to measure the backing pressure. Measuring the thermal conductivity with a Pirani gauge [119] we determine the backing pressures down to 0.1 mbar. The backing pressure is controlled by a mechanical needle valve. For measurements at fixed pressure a standard backing pressure of 100 mbar was applied for doubly-excited helium and 30 mbar for singly excited helium.

3.2.4 Energy Resolution of the Flat-Field Spectrograph

We use a reflective, gold-coated line grating after the target cell to split up the attosecond beam in space and time and let it interfere with the equally split-up dipole response of the target. To project the focus in the experimental interaction region onto the camera, the grating has a cylindrical shape and therefore additionally acts as a focusing optic for the (horizontal) wavelength axis. A cylindrically shaped grating with equally spaced lines will focus onto a circle, the Rowland circle [120, 121]. A projection of the focus on a flat focal plane is achieved by using a variable line space (VLS) structure instead of a linear one, a technique that is used in the XUV region for over 30 years [122,123]. We use such a VLS grating to disperse the wavelengths between ~ 11 nm and 62 nm (corresponding to ~ 20 eV to 110 eV) onto a flat wide image plane of ~ 110 mm size (see Fig.3.7). The average groove spacing is 833 nm [124] corresponding to a lattice constant of 1200^{-1} mm. In the image plane the XUV light is detected by a back-illuminated thermo-electrically cooled charge-coupled device (CCD) camera [125] with a pixel resolution of 1340×400 (also

see chapter 3.3). Typically the integration time is set between hundreds of milliseconds up to a few seconds enabled by the low thermal and readout noise and the high dynamic range. As the physical dimension of the camera chip is 26.8 mm × 8 mm it is moved along the horizontal axis to cover the whole wavelength range from 11 nm and 62 nm. The groves of the used VLS grating are linear along the vertical direction and thus the grating acts as a plane mirror in the vertical direction, perpendicular to the spectral separation. On the camera chip the vertical beam profile can thus be analyzed (see Fig. 3.7). For the experiments discussed in this work the interference between the XUV pulse from the HHG process and dipole response of the target on the camera chip is of importance. Therefore, the question arises how long after the XUV pulse is reflected off the grating it is possible to observe such interference. Two beam paths of the short wavelength (blue beam) are drawn in Fig.3.7. Number 1 travels in the center of the beam and is reflected of the center of the cylindrical shaped grating and then projected onto the camera. Beam path number 2 travels at the edge of the pulse and is reflected on the left hand side of the grating and the projected onto the same camera spot as beam path 1. Since the VLS grating has a cylindrical shape the beam path number 1 is longer than path 2. The path length difference s is roughly 1.5 cm. The maximal time difference is given by $\Delta t = s/c = 50$ ps, where c is the speed of light. If two XUV light pulses are not more than 50 ps delayed against each other, they will be coherently add up on the camera chip.

Later in this work, we will map the wavelength on the an energy axis, allowing for a more intuitive physical description of the observed phenomena. Therefor the spectrometer resolution in terms of XUV photon energy is of importance. As the wavelength axis is equally spaced ($\frac{\mathrm{d}\lambda}{\lambda}$ =const.), the energy resolution $\frac{\mathrm{d}\omega}{\omega}$ increases quadratically with increasing wavelength ($\frac{\mathrm{d}\omega}{\omega} = \frac{\mathrm{d}\lambda}{\lambda} \cdot \frac{c}{\lambda^2}$). The spectrometer resolution is estimated by determining the line width of the asymmetric 2s2p resonance of helium for the case of no VIS pulse and comparing it to the literature value [28, 35]. The best result is produced if the 2s2p line is calculated using the literature values ($E_\mathrm{r} = 60.15$ eV, $\hbar\Gamma = 37$ meV) and convoluted with an Gaussian distribution of 20 meV standard deviation, which we take as an estimator for the spectrometer resolution. For the resolution for photons around 20 eV we convolve a δ-like absorption line with an Gaussian to match the experimentally observed spectral width to confirm this resolution. Using a δ-like absorption line is reasonable due to the lifetime in the nanosecond regime of these singly-excited states (see Tab.2.1). We thereby estimate a resolution of 5 meV standard deviation corresponding to 11.7 meV FWHM. Other experimental setups also using the same VLS grating model estimate a resolution of 12 meV FWHM for the energies of around 20 eV [126].

3.3 Recording Spectral Data

In Fig. 3.8 a full chip camera picture is shown as it is acquired during the experiment. The camera has 400 vertical pixels and 1340 horizontal ones. The vertical axis shows the spatial distribution of the XUV light while the horizontal axis is approximately proportional to wavelength as the light is split up into its wavelength components by the VLS grating (see focal plane in Fig. 3.7). The target gas was helium with a backing pressure

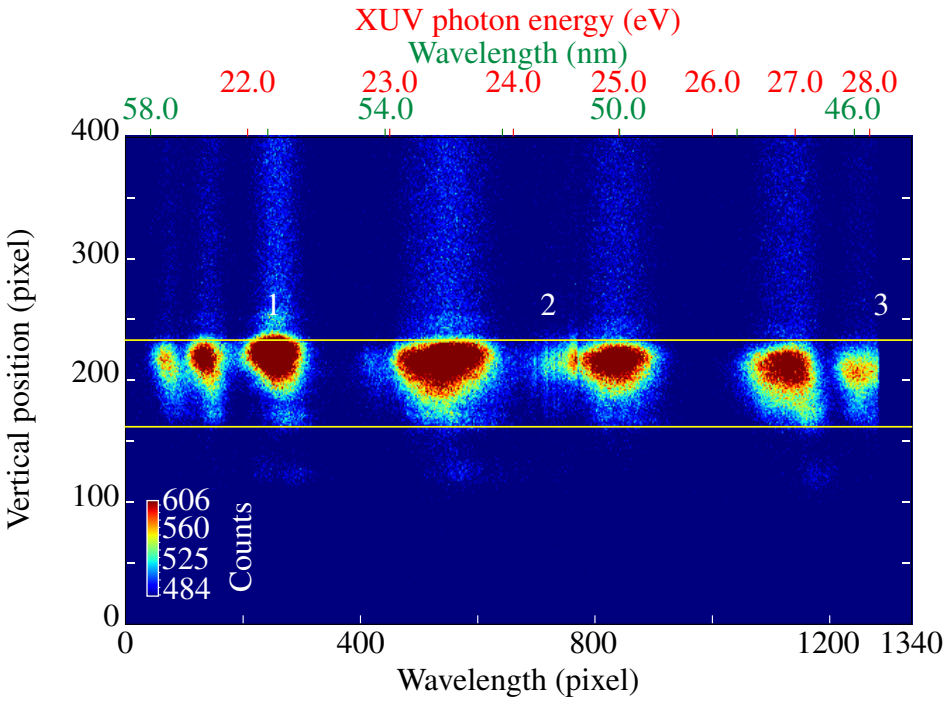

Figure 3.8: Full-chip camera picture (representing an XUV spectrum) as it is acquired during the experiment. The lower x-axis and y-axis are labeled in raw pixels of the camera, where the x-axis is approximately proportional to wavelength diffracted by the grating and the y-axis shows the spatial distribution of the XUV light. Above the graph the calibrated wavelength and photon energies are added. The picture shows the measurement of singly excited helium. The close to round spot below marker 1 is caused by one harmonic in the XUV pulse train. All other circular structures are harmonics. Some of them appear as triple spots. The structure elongated in the y-direction in the area below marker 2 arise from the absorption of the 1s*n*p Rydberg series of helium. The yellow horizontal lines are markers for the vertical (spatial) binning of the data (see Fig. 3.9 for the result).

of 30 mbar. A coarse energy scale is attached to the camera linear translation stage. According to this scale the center of the camera chip is at 24 eV, so the covered area is in the energy range of the singly excited helium series.

The thin vertical stripes in the area below marker 2 arise from the absorption of the 1s*n*p Rydberg series of helium. The close to round spot below marker 1 is caused by one harmonic in the XUV pulse train. All other circular structures are harmonics with a main periodicity of 3.4 eV, but some of them appear as triple spots with a separation much smaller than 3.4 eV. These triple spots could be caused by several effects. One is a spatial chirp on the fundamental pulse (see [112]), the other is that the third order diffraction of the grating overlaps with the first order, so some of the weaker spots are third order diffraction of the thirty-fifth and thirty-seventh harmonic. The sharp edge at marker 3 has no physical but geometric reasons caused by the layout of the spectrometer chamber [5]. The light from the VLS grating cannot reach the outer part of the camera chip. However, this does not negatively affect the measurement. The information about the vertical beam

[5] If the camera is moved to higher energies another sharp vertical cut will be observed - the absorption edge of aluminum (filter material) at 72.1 eV

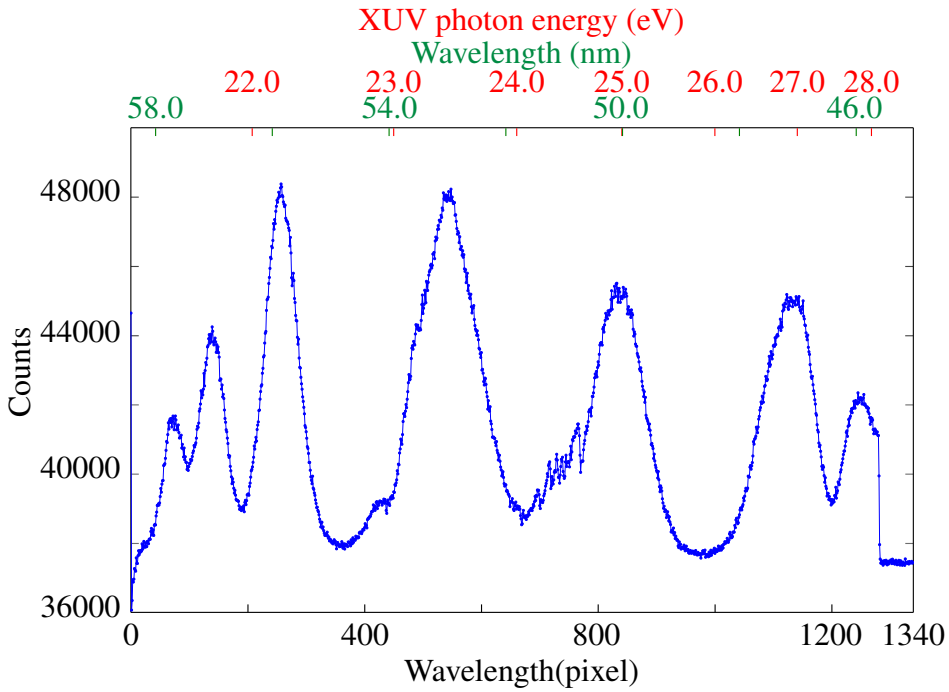

Figure 3.9: Software binning of an acquired XUV spectrum. Shown is the part within the yellow horizontal cursors of the full chip camera picture shown in Fig. 3.8. The lower x-axis shows the different wavelength diffracted by the grating and the y-axis shows the accumulated counts. Above the graph the calibrated wavelength and photon energies are added. The structures between pixel 650 and pixel 800 is again absorption of the 1s*n*p Rydberg series of helium. Again the sharp edge at pixel 1281 is visible (which is also visible below marker 3 in Fig. 3.8), resulting from a geometric blocking of the beam path.

profile is important to align the setup and for measurements which separate the exciting light field from the target's dipole response. For most of the other setups a vertically (spatially) binned (integrated) spectrum is recorded and analyzed.

3.3.1 Software & Hardware Binning

By integrating over a certain region of the chip (indicated by the two yellow horizontal lines in Fig. 3.8) the information of the vertical axis is sacrificed for an enhanced signal to noise ratio and a faster read-out time of the camera.

The integration can be done by software after the data recording or by controlling the shift of the registers on the camera chip. For both cases the signal to noise ratio is enhanced because only those parts of the chip are selected which have been illuminated. But only if the registers of the chip are directly shifted and summed up "on chip" the read out time is shortened because of the reduction of transferred and stored data. This plays an important role for the measurements since the read-out time is reduced from the order of seconds for a full chip image to the order of hundred milliseconds for a so-called binned spectrum, thus making the measurement more independent of long term drifts of the laser system. More important than the decreased readout time, is the reduction in read-out noise arising

in the digitization of the number of accumulated charges. After recording the spatially binned spectrum of the XUV camera picture, we map the wavelength axis of the camera bin to an energy axis by using the literature values [28, 35, 71] for the energies of the recorded line shapes. Then, we linearize the energy axis by interpolation. From now on, we will only use the energy calibrated spectra for the further analysis.

3.4 Analyzing the Absorption Line Shape Spectra

3.4.1 Reconstructing the Absorbance of Helium

After the energy calibration of the spectra, the absorbance is calculated out of the recorded intensities of the XUV light after transmission through the helium target. At first sight, the recorded spectra show the slowly varying high-harmonic spectrum and the sharp line shapes of the helium states (see for example Fig. 3.9). As we are interested in the absorption properties of the excited states in helium, we will only consider the helium absorbance [also called the optical density (OD)] and therefore remove the high-harmonic modulation of the spectrum.

The OD is determined by dividing the transmitted spectral intensity I through helium by the corresponding spectral intensity I_0 of the pure high harmonics and then taking the negative logarithm[6] of this intensity ratio $\frac{I}{I_0}$. There are two methods of acquiring I_0:

A. Measured reference I_0^{m}: determine I_0 by removing the helium from the target gas cell and perform the measurement.

B. Fourier filtered reference I_0^{f}: apply a low-pass Fourier filter on I to extract the low frequency part, scale it and use this as the reference I_0.

The more straightforward method is using $I_0 = I_0^{\mathrm{m}}$, the measured reference. When there is no gas in the target cell, the camera will detect the unperturbed XUV spectrum as it is produced in the HHG cell and transmitted to the spectrometer[7]. The disadvantage of this method is that HHG, being a highly non-linear process, is sensitive to even small fluctuations in the driving laser. As a consequence, these fluctuations translate into measurable changes in the spectral intensity profile. This means that even for exactly the same settings two spectra recorded one after the other are distinct. To get rid of these fluctuations, we use the second method (B) mentioned above to acquire I_0: We apply a low-pass Fourier filter on I to extract the low frequency part I_0^{f}. In Fig. 3.10, a comparison between I_0^{f} and I_0^{m} for the energy range of the doubly excited $\mathrm{sp}_{2,n+}$ states in helium is shown. Plotted are

[6] Note, that within this work, we use the decimal logarithm for the definition of the absorbance. Other fields (e.g. biology) define the absorbance using the natural logarithm.

[7] As the inner mirror produces a small walk off, different spectra for different mirror positions must be recorded.

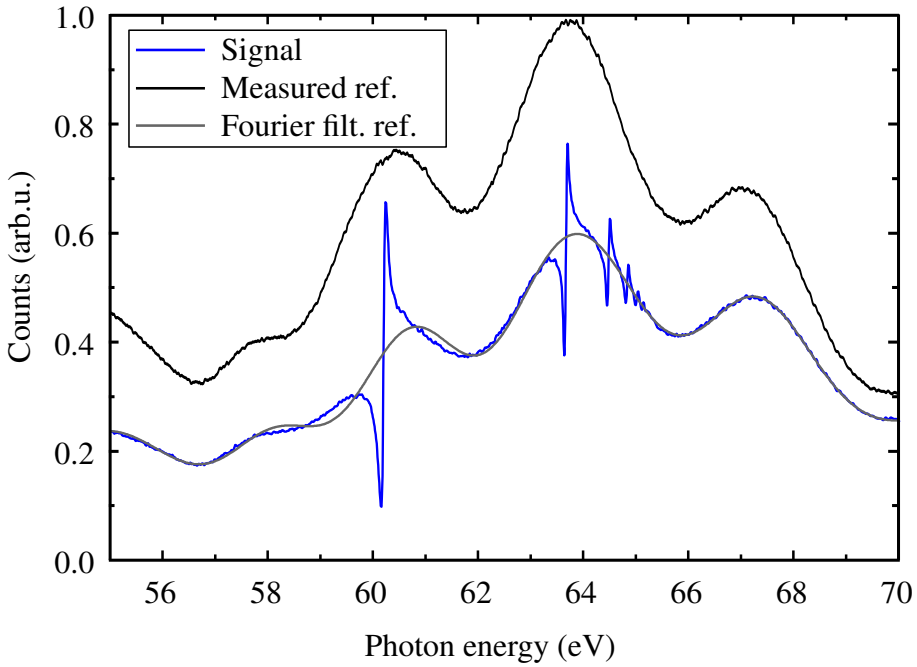

Figure 3.10: Directly measured XUV spectra $I(\omega)$ after the transmission through the helium target (blue solid line), together with the Fourier low–pass-filtered harmonic modulation I_0^{f} (grey solid line) and the measured reference I_0^{m} (black solid line) taken with the same experimental settings but without the target gas. The actual harmonic spectrum I_0^{m} has a higher count rate, which cannot be recovered by the Fourier filter. If I_0^{f} is scaled to match the height of the actual harmonic spectrum. It can be used as the reference spectrum I_0 to retrieve the resonant absorption profiles OD (see for example Fig. 4.9 on page 61).

the energy-calibrated transmitted spectra for the measured reference I_0^{m} (black solid line) and the Fourier-filtered reference (grey solid line) as well as the corresponding measurement with target gas (blue solid line). The intensity of the actual harmonic spectrum I_0^{m} is twice as big as the Fourier filtered one because of the continuum absorption of helium in this energy range, which cannot be revealed by the Fourier filter.

The non-resonant continuum absorption σ_0 in the regime of the doubly-excited states of helium arises from the absorption into the $N = 1$ continuum. It only changes slowly as a function of energy. Therefore, σ_0 is also termed background absorption. It is extracted from the precision measurements in the publication of Samson, Xe, Yin and Haddad [127]. The data in this publication (namely figure 3 and table 1) have been fitted using a fifth-order polynomial. The best fit parameters are listed in Tab. C.1 in appendix C.3, which define the slowly changing background absorption $\sigma_0(\omega)$. For a XUV photon energy of 63.66 eV the corresponding background absorbance roughly evaluates to 0.294.

Having applied the Fourier filter on I to extract the low frequency part I_0^{f}, we now calibrate I_0^{f} in the second step. Therefore, we scale the spectrum I_0^{f} by the continuum absorption σ_0 via

$$I_0^{\mathrm{f}} \cdot \mathrm{e}^{+\sigma_0 \cdot \rho \cdot l} = I_0^{\mathrm{r}} \tag{3.1}$$

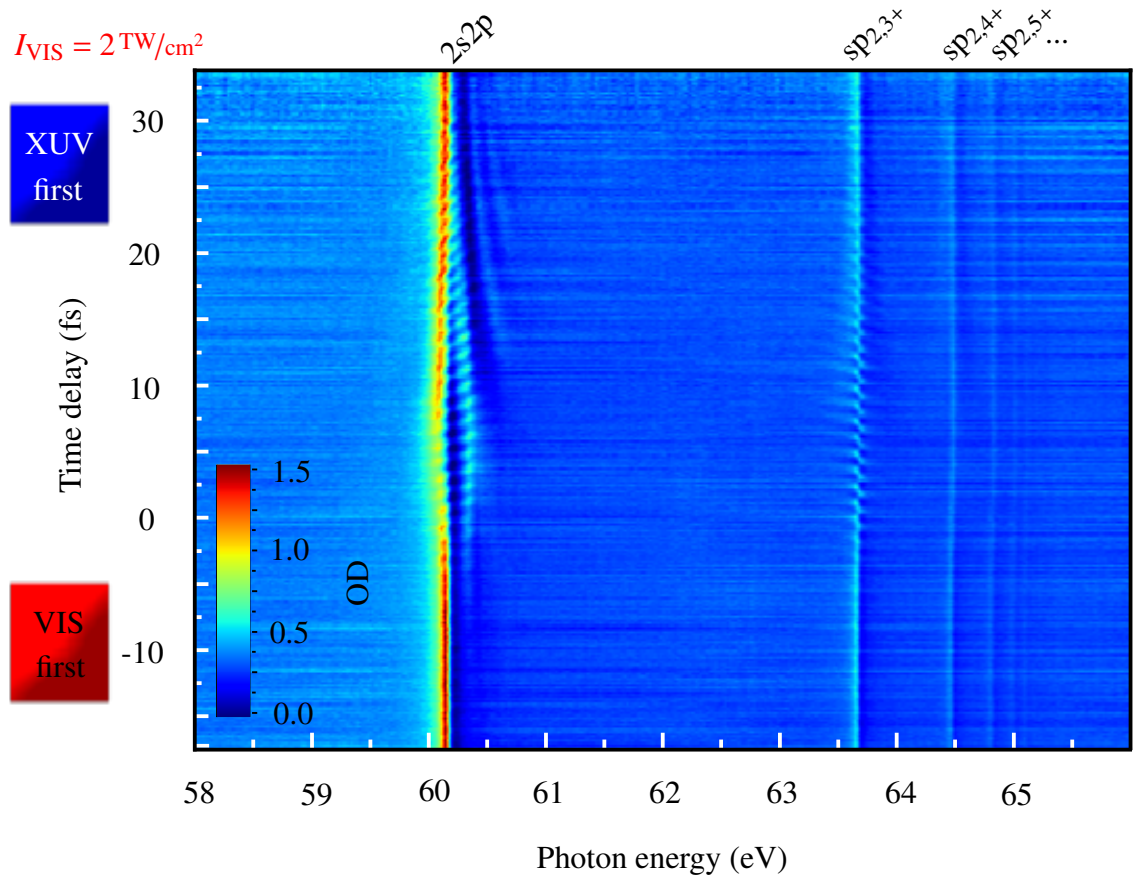

Figure 3.11: Absorbance (OD) for different time delays between XUV and VIS pulse. The relative ODs have been obtained by dividing the spectra with helium in the target cell by the measured reference, acquired without helium in the target cell. For negative time delays the VIS pulse precedes the XUV pulse.

with the path length density product $\rho \cdot l = 0.15$ a.u.. This value was determined from method A by directly measuring I_0^{m}, and averaging over the fluctuations in the XUV spectrum. For this procedure it is assumed that the background absorption is not altered by the VIS laser pulse. The rescaled spectrum I_0^{r} is then used as the reference I_0. For the case of the singly excited 1snp series there is no background absorption, as these states are not embedded in a continuum. Therefore the Fourier filtering of I returns the correct result without rescaling.

Fig. 3.11 shows the absorbance obtained using the measured reference (method A), while Fig. 3.12 shows the OD obtained using the reference reconstructed by the Fourier filtering method B. The fluctuations of around 10% in the absorption, visible as thin horizontal lines in Fig. 3.11, are caused by pulse to pulse intensity fluctuations in the driving laser translating into small changes of the XUV–high-harmonic spectral profile. In contrast to Fig. 3.11 there are almost no fluctuations visible in Fig. 3.12, where the absorption is obtained using method B, resulting in a higher signal-to-noise ratio. Comparing the results of method A with the Fourier reconstructed spectra of method B shows that the later does not change the spectral line shapes. This is due to the fact, that the Fourier

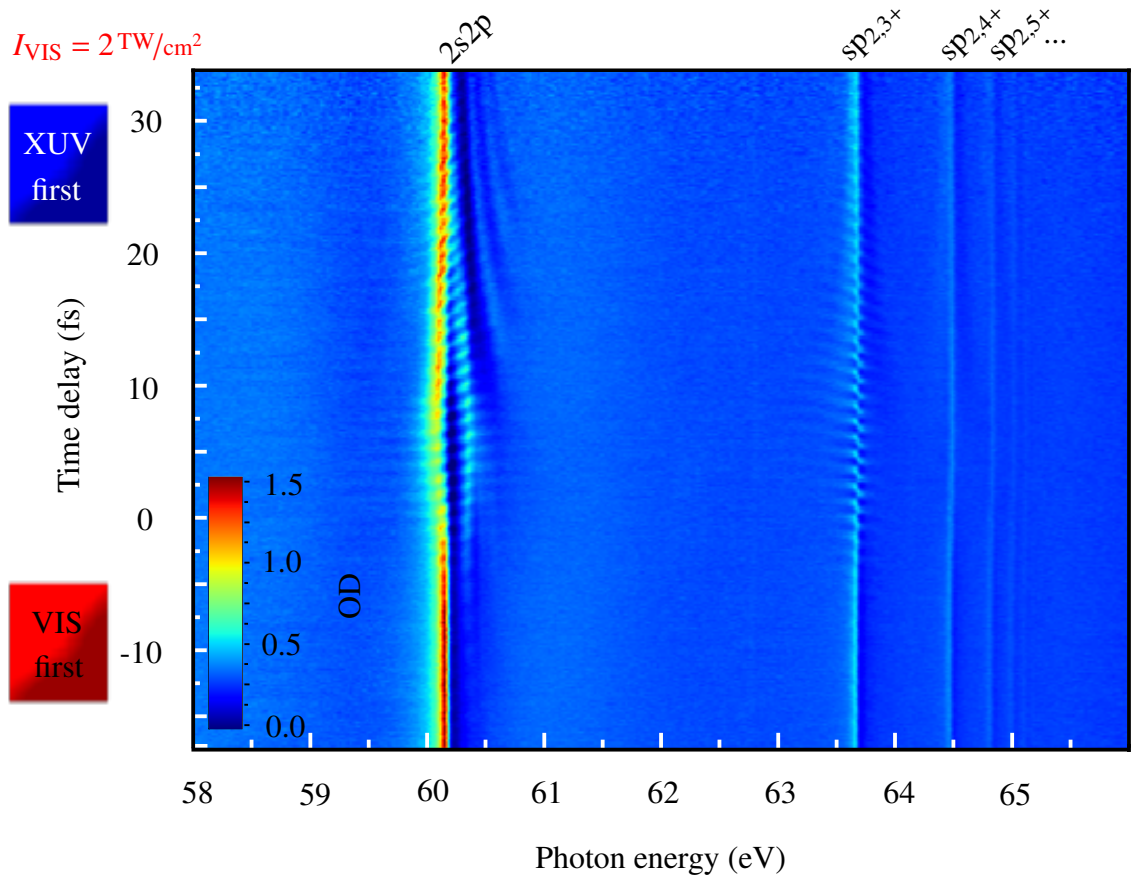

Figure 3.12: Absorbance (OD) for different time delays between XUV and VIS pulse. The experimental data set is the same as in Fig. 3.11. In contrast to Fig. 3.11, the ODs have been obtained by method B, i.e. dividing by the Fourier-filtered reference which has been rescaled with the background absorption σ_0. With this method a higher signal-to-noise ratio is obtained, since for each single time-delay step the statistical harmonic intensity fluctuations are eliminated. The visible structures are the same, proving the validity of the Fourier-filtering method.

components of the harmonics in the spectrum are clearly separable from those of the observed features. The periodicity of the harmonics is twice the photon energy of the driving laser (see chapter 2.6.2), namely 3.4 eV. The broadest feature that can be reliably extracted using the Fourier-reconstruction method has a maximal width of 850 meV. In the performed experiments, the VIS laser pulse following the XUV excitation changes and also broadens the line shapes. For the spectra presented in this work, the condition of maximal width of 850 meV for each spectral feature of interest is fulfilled for almost every experimental condition. Therefore from now on we will use method B, the Fourier filtering, for all optical densities of the singly and doubly exited states of helium presented in this work.

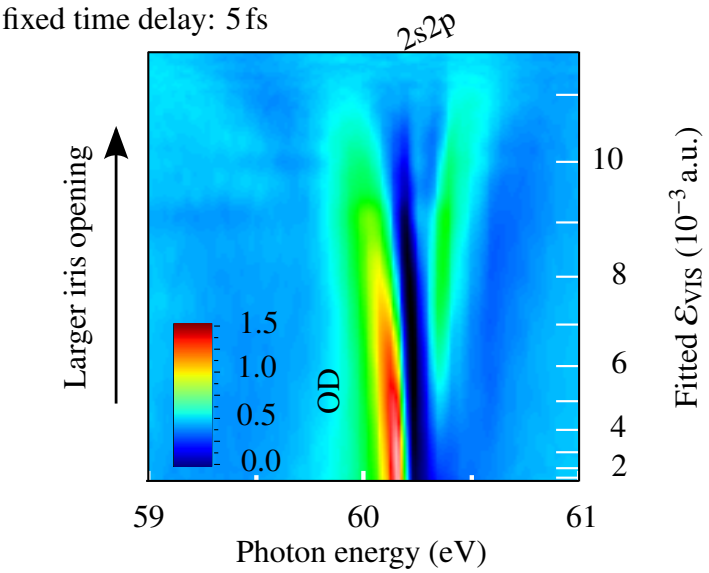

Figure 3.13: Optical density of helium in the energy region between 59 eV and 61 eV. The vertical axis on the left shows the iris opening in steps from small to large beam diameter. The vertical axis on the right shows the electric field strength $\mathcal{E}_{VIS}$ used in the time-dependent close-coupling simulation to reproduce the measured Autler–Townes splitting of the 2s2p line.

3.4.2 Calibration of the VIS peak intensity

As previously stated, if the VIS laser pulse is present, the natural line shape can be altered. We now look at the profile of the 2s2p line. This line shape changes in the region of the pulse overlap (around time delay zero) depending on the VIS pulse intensity and the time delay between XUV and VIS pulse.

The 2s2p starts to split around time delay zero (see Fig. 3.13). The maximum of the splitting is reached for a time delay of +5 fs. To cancel out time-delay dependent fast oscillations, we build an average over two such modulation periods. Plotting this averaged 2s2p line shape as a function of the iris opening (see Fig. 3.13) we note an increase of the splitting with accordingly increasing VIS intensity in the interaction region. This is the so-called Autler–Townes splitting arising from the repulsion of two states coupled to each other in the presence of an electromagnetic field (see chapter 2.3). The stronger the coupling between the states, the larger their energy splitting.

For the case of strong coupling (larger than the detuning from the resonance, see secion 2.3), the coupling strength between the 2s2p state and the laser-dressed state "$2p^2 - \gamma$" is proportional to the electric field strength of the VIS pulse. Subsequently the width of the Autler–Townes splitting is proportional to the square root of the VIS-pulse peak intensity. For the intensity calibration we compare the measured splitting with the splitting obtained in a time-dependent close-coupling simulation for autoionizing states. For details of the simulation see [128]. The spectra obtained from the simulation are convoluted with the spectrometer resolution. A comparison with the measured data gives the calibration curve for the VIS intensity. This method of determining the VIS intensity via the Autler–Townes

splitting enables us to perform the intensity calibration *in-situ*. The relative systematic error is on the order of 0.5, as it is common for intensity calibrations of short pulses[8]. In any case, we have the additional information that the iris opening, and thus also the intensity, is monotonically increasing as set experimentally, which reduces the error in the intensity calibration. A more detailed description of the VIS intensity calibration is found in chapter 6.6 of Christian Ott's PhD thesis [128].

To calibrate the VIS intensity for the singly excited states we use the fact that the third order diffraction of the VLS grating for 60.1 eV lies at 20 eV and therewith in the energy range of the singly excited states of helium. As a result the 2s2p line shape can be resolved in third order diffraction along with the 1s*n*p states on the camera chip, if the HHG process is optimized to produce XUV light covering the complete range between 20 eV and 65 eV. Then we use the calibration for the 2s2p state as explained above to gauge the intensity values for the VIS pulse also for measurements near 20 eV. After the calibration of the energy axis, the time-delay axis and the intensity of the VIS pulse, the data are prepared for the discussion and the interpretation in the following chapter.

[8]Determining the peak intensity in the focus from the measured averaged intensity of the VIS laser beam does require the laser repetition rate, pulse duration, pulse energy and the focal diameter. The latter involves a large error as it depends on the exact beam alignment between XUV and VIS pulse as well as the iris opening. However, the focal diameter is not necessary for the *in-situ* calibration. Thus, the error bar for the intensity determined by the *in situ* calibration is much lower than for the *ex-situ* calibration.

Chapter 4

Laser Control of Absorption

Spectroscopic methods to characterize light after its interaction with matter are an essential tool for uncovering the mechanisms involved in this interaction. In this work, we use helium as a prototype system for matter with correlated-electron effects and laser light to investigate its properties. Typical ground-state transition frequencies in helium are of the order of $10^{17}\,\mathrm{Hz} \mathrel{\hat{=}} 41\,\mathrm{eV}$. As typical optical laser photons are far off this energy range, we use high-order harmonic generation to produce attosecond extreme-ultraviolet (XUV) pulses with energies between 15 eV and 110 eV. These XUV pulses induce a polarization in the helium atom, which we then perturb by a subsequent 7 fs near-visible (VIS) laser pulse. Observing the singly excited $1sn\mathrm{p}$ series and the doubly excited $\mathrm{sp}_{2,n+}$ series, we extract information on the relaxation process. As described in section 2.1.2, the transition strength varies over a certain energy range close to a resonance due to interference between different quantum-mechanical pathways. This distribution is called the line shape of the transition.

In general, different relaxation channels exist. Some states decay only radiative, others have multiple radiative and non-radiative decay channels. Controlling the coupling between different states leads to many interesting phenomena which have been widely studied in the optical frequency regime, such as electromagnetically induced transparency (EIT) [129, 130] or the possibility to slow (or even stop) light [131, 132].

As a result of a relaxation process, a particle carries away the excess energy. This particle is either an electron in the case of (auto-) ionization or a photon in the case of radiative decay from an excited state. If only a single radiative decay channel exists (and no additional effects like Doppler broadening [133] occur) the resulting line shape is a symmetric Lorentzian. Asymmetric absorption line shapes emerge when the pathways (phases) for different competing decay channels add up coherently. For example, asymmetric Fano line shapes are observed when discrete excited states are coupled to an energetically degenerate continuum of states [23, 34]. In helium one observes Fano line shapes above 60 eV, where both bound–bound and bound–continuum dipole transitions are present. The dipole response of the bound–bound transition exhibits an exponentially decaying

envelope, while the dipole response of the bound–continuum transition is instantaneous and therefore modeled by a δ-function.

As the doubly excited states of helium are embedded in the $N = 1$ continuum, both of these transitions are degenerate and are coupled to each other by the configuration interaction. As result of this discrete–continuum coupling mechanism, the temporal dipole response to an infinitesimal short excitation is not simply the sum of the exponentially decaying isolated state and the δ-like continuum response. In fact, the influence of the coupling (as described in section 2.1.2) induces a phase shift in the exponentially decaying dipole response with respect to a decay in the absence of an interfering continuum channel. The phase shift manifests itself in the change of the line shape with respect to the Lorentzian one. This is the interpretation of the time-domain formalism of the Fano process, as it was developed in our group (also see [1] and [2]).

Such a phase shift, which naturally occurs in the case of doubly-excited helium due to the configuration interaction can also be induced by an artificial interaction. In our experiment this artificial interaction is realized by a VIS laser pulse. As a result of the interaction with the VIS laser pulse the unperturbed decay of the excited states is changed and the naturally resulting line shape is altered. The detailed analysis and modeling of this process is subject of this chapter.

This chapter is structured as follows: In **section 4.1** the experimental control of the spectral line profile by the intensity of the VIS pulse or the time-delay between the XUV and the VIS pulse is presented. The control of the line shape and absorption in general can be understood with the theoretical framework developed in **section 4.2**. Finally, the discovered control mechanism is employed to access amplitude and phase information of a dipole oscillating with 15 PHz in **section 4.4**.

4.1 Controlling Spectral Line Shapes

In this section the main experimental results of this work are presented. We will discuss how the experimental control of the absorption of singly and doubly-excited states of helium is realized. In that context, it will be shown that the spectral (absorption) profiles are not only slightly altered, but can be completely changed in their nature and even be inverted.

This is first shown for the time–delay-independent measurement, where the control parameter is the intensity of the coupling VIS pulse, while the time delay is kept fixed at a constant value. With a suitably chosen intensity we achieve an gain of light at an energy where it was absorbed before.

Then, we extend the controllability and also vary the time-delay between the exciting XUV and the coupling VIS pulse. Some recent publications in the field of attosecond science report about effects connected to energetic line shifts observed on a time scale

faster than a cycle of the near-visible laser light used in their experiments [134, 135] or theoretical calculations [136, 137]. In this chapter we show that also in our data the absorption maximum energetically shifts as a function of the time delay. We find that this goes along with changes in the line shape and use the high resolution to identify these changes in the line profiles as the actual source of an apparent sub-cycle energy shift of the states. In addition, we will show that within a fifth of the oscillation period of the VIS laser pulse ($\approx 500\,$as) we turn a symmetric Lorentzian absorption into an asymmetric Fano line shape and *vice versa*.

4.1.1 Intensity Control

In this section we investigate the intensity-dependence of the line profiles of the $sp_{2,n+}$ and the 1snp states. To focus on the intensity dependent effects, we rule out any time-delay dependence by scanning the time delay over a full VIS optical cycle and taking the average spectrum of these spectra, as done in the previous section for the intensity calibration. The full optical cycle of 2.4 fs is centered around the time-delay +5 fs. This procedure was performed for each intensity. First we will present and discuss the intensity-dependent effects in the data set of the doubly excited series, then the effects in the data set of the singly excited series will be approached.

A sequence of four OD spectra of the $sp_{2,n+}$ ($n \geq 5$) states is shown in Fig. 4.1 for different intensities of the VIS pulse. The continuum absorption has been subtracted for these spectra. For zero intensity the well-known Fano line shapes are recorded. Labeled above each graph is the fitted Fano asymmetry parameter for the absorption profile of the $sp_{2,5+}$ state. When the VIS intensity is set to $2\,\mathrm{TW/cm^2}$ the former asymmetric Fano line shapes have changed to symmetric (Lorentzian) absorption peaks. The profile of each state reverses in shape if the VIS intensity is set to $3\,\mathrm{TW/cm^2}$. When we use a VIS pulse peak intensity of $4\,\mathrm{TW/cm^2}$ even a window resonance is produced.

The full set of 33 spectra of the complete doubly excited $sp_{2,n+}$ ($n \leq 8$) series ranging from zero VIS intensity (neglecting leakage) to $4.5\,\mathrm{TW/cm^2}$ is shown in Fig. 4.2. The labels on top of the graph show the energy positions for the unperturbed states as listed in Tab. 2.1. The white curve marks the field strength for the barrier suppression ionization (BSI) into the $N = 2$ continuum.

BSI occurs, when an electric field is strong enough to bend the Coulomb potential such that the Coulomb barrier is completely suppressed and the bound electron is free to move into the continuum, i.e. the electronic wavefunction spreads into the continuum. Therefore the laser field strength must be above a critical value $\mathcal{E}_{\mathrm{crit}}$, which in atomic units is defined by

$$\mathcal{E}_{\mathrm{crit}} = \frac{\mathcal{I}_{\mathrm{P}}^2}{4Z}. \tag{4.1}$$

where Z is the charge of the remaining ion and $\mathcal{I}_{\mathrm{P}}$ is the ionization potential, which in the case of the $sp_{2,n+}$ series is the respective energy distance of each state to the $N = 2$

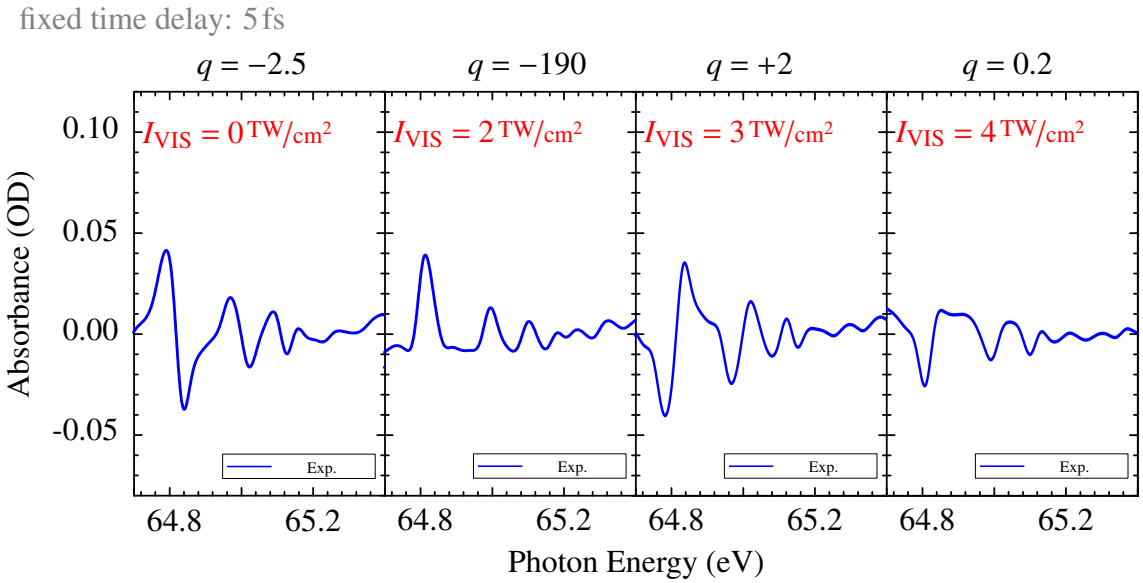

Figure 4.1: Measured line shapes of the doubly-excited $sp_{2,n+}$ series for $n \geq 5$ in helium referenced to the continuum absorption. The first panel shows the unperturbed (without the VIS pulse) asymmetric Fano spectral absorption line with a literature value of $q_{\mathrm{orig}}(sp_{2,5+}) = -2.5$. In the presence of the VIS pulse set to a peak intensity of $2\,\mathrm{TW/cm^2}$ and following the δ-like XUV excitation with a time delay of 5 fs, the line shapes turns into symmetric Lorentzian absorption peaks with a q fitted by eye to -190. If the VIS pulse is set to a peak intensity of $3\,\mathrm{TW/cm^2}$, the absorption profiles revert their original symmetry now showing a $q = +2.0$. At an intensity of $4\,\mathrm{TW/cm^2}$ the special case of a window resonance $q = 0.2$ is achieved. If no continuum absorption was present, this scenario could even lead to a gain of photons at the resonance energy (see chapter 4.1.1).

continuum at 65.40 eV. As the energy distance of the $sp_{2,n+}$ (Rydberg) states to the $N = 2$ continuum decreases proportional to the square of the principal quantum number, the critical field strength $\mathcal{E}_{\mathrm{crit}}$ decreases rapidly towards the ionization threshold. Remarkably, all states in Fig. 4.2 are clearly observed as stable and sharp resonance lines significantly above critical field strengths for BSI into the $N = 2$ continuum, until a sudden change occurs at a VIS intensity of around $4\,\mathrm{TW/cm^2}$ where all states disappear abruptly. At first sight the systematic error in the intensity calibration of $\frac{\Delta I_{\mathrm{VIS}}}{I_{\mathrm{VIS}}} \approx 0.5$ might be a possible explanation. This is true for the state 1s2p and $sp_{2,3+}$ with relative high critical field strength $\mathcal{E}_{\mathrm{crit}}$. The higher states ($n \geq 4$) by contrast have a very low critical field strength and still resist the ionization by the laser.

The resistance to laser-induced ionization comes as a surprise. Experimental results from Loh *et al.* [101] could not be explained without taking into account an additional ionization channel. It is found that the 2s2p state is coupled to the $2p^2$ state by one VIS photon[1]. In short, the additional channel necessary to explain the findings is identified as the tunnel ionization of the $2p^2$ into the $N = 2$ continuum [138, 139]. The main difference between the experiment presented by Loh *et al.* [101] and the one presented in this work is the pulse duration of the used coupling pulse. In [101] a much longer coupling pulse with a

[1]The nature of this coupling goes beyond the scope of this section and will be discussed in detail in section 4.3.5, see for example Fig 4.15 therein.

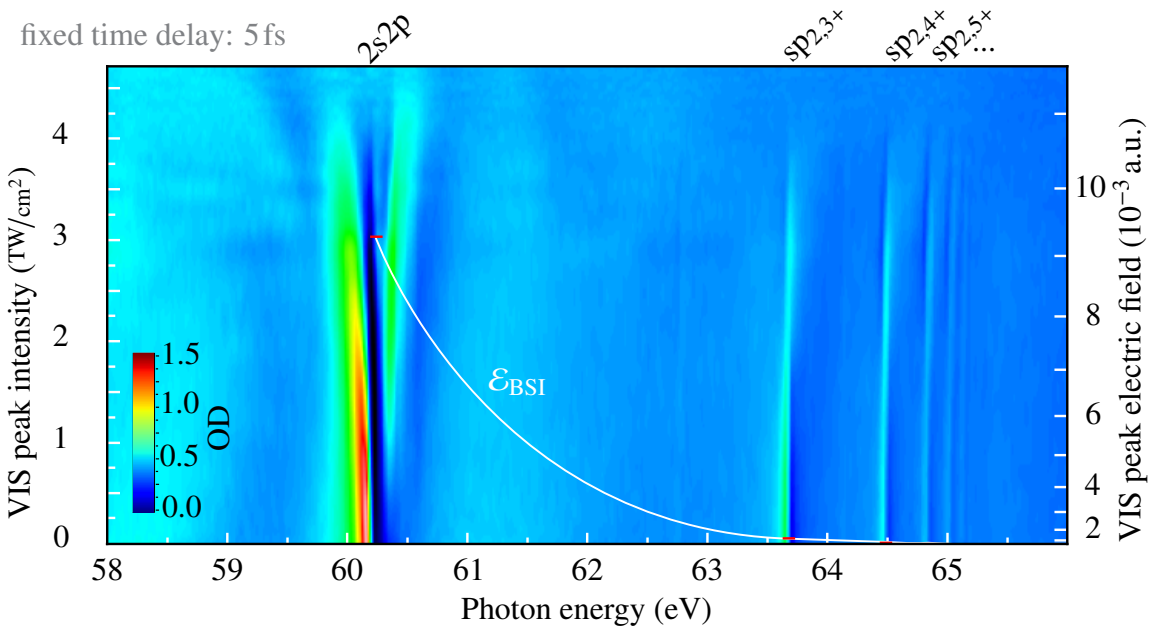

Figure 4.2: Optical density of helium in the energy range between 58 eV and 66 eV. The vertical axis shows the different intensities for the VIS pulse. The critical field strength $\mathcal{E}_{\mathrm{BSI}}$ for barrier-suppression ionization (BSI) into the $N = 2$ continuum is indicated (red bars) and connected by a cubic spline interpolation as a guide to the eye (white line). All states exist for intensities high above the BSI limit. The states above 63 eV disappear at a VIS intensity around $4\,\mathrm{TW/cm^2}$. A detailed description of the features in this graph is given in the main text.

duration of 42 fs FWHM was used. This longer pulse duration means a longer interaction time and thus a more severe influence on the states in terms of their ionization and their dipole response, as it will be explained in the next section. This might be the origin of the different finding in the case of a longer coupling pulse.

The resistance against ionization of the highest states in our short VIS pulse is a benefit as it allows to trace the profile of the states in the transition from the perturbative to the strong-coupling regime. And indeed the line profiles change significantly with increasing VIS intensity. Below, we will use the change in the line profile to extract state-resolved phase information from this data.

In the structure around the 2s2p state the formation of an Autler–Townes doublet is visible, which occurs due to the repulsion of the 2s2p state and the laser-dressed state "$2p^2 - \gamma_{\mathrm{VIS}}$", as also discussed in [101]. In the center part of the structure around the 2s2p state at intensities above $3\,\mathrm{TW/cm^2}$ the laser dressed state "$\mathrm{sp}_{2,3+} - 2\gamma_{\mathrm{VIS}}$" emerges.

Also the absorption line shape for the higher excited $\mathrm{sp}_{2,n+}$ ($n \geq 4$) states is altered with increasing VIS intensity. In contrast to the Autler–Townes splitting of the 2s2p state, the energy position for each state remains constant (which is important and will be discussed in chapter 4.4). Instead, their asymmetry parameter q changes. For zero intensity the profiles show a high optical density at their lower energetic edge and a lower OD at their high-energetic edge, visible as light blue/dark blue shape for increasing photon energy in Fig. 4.2. The profile of all states reverses in shape (now going dark blue/light blue

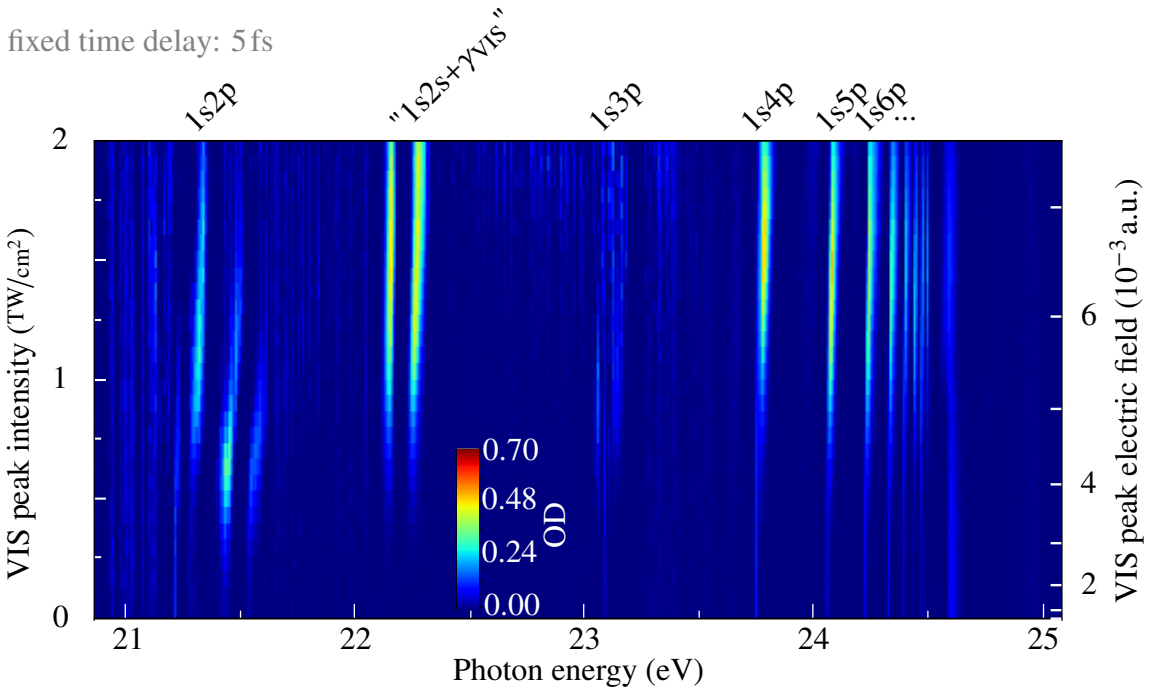

Figure 4.3: Optical density of helium in the energy region between 20.7 eV and 24.55 eV. The vertical axis shows the different intensities for the VIS pulse. For the lowest intensity values the lines are not altered. The energy position of the undisturbed states are marked on top on the graph. The highest state which is distinguishable from its neighbor is 1s14p. In the main text a description of the features visible in this graph is given.

for increasing photon energy) between VIS intensity 2.5 TW/cm² and 3.5 TW/cm² [128]. As described above, Lorentzian absorption peaks appear for 2 TW/cm² symmetric (Lorentzian) and window resonances are produced shortly before the complete ionization takes place (around 4 TW/cm²). The theoretical explanation of these changes will be subject of the next chapter.

The intensity-dependent effects of the singly excited 1s*n*p series are presented in Fig. 4.3 which shows 36 spectra starting from nearly zero VIS intensity to 2 TW/cm². The labels on top of the graph give the energy positions for the unperturbed 1s*n*p states as listed in Tab. 2.1, while the energy of the 1s2s state is taken from [71].

For the 1s*n*p series, the states with highest energies start to ionize at a VIS intensity of around 1.9 TW/cm², which shows that these states are less resistant to high-intensity VIS light than the doubly excited $sp_{2,n+}$ series. Also, no abrupt disappearance of all states at the same intensity is observed. The fact that the 1s*n*p lines are visible at all also for zero VIS intensity comes unexpected considering their natural line widths of 7.4 μeV for the 1s2p down to 0.1 μeV for the 1s8p, which are at least three orders of magnitude below the resolution of the spectrometer resulting in a reduction of the absorption peak amplitude.

The reason for a measurable absorption peak amplitude is a laser broadening by the long lasting pedestal of the VIS pulse, as it is typical for compressed ultra-short Laser pulses. A recent publication on *in situ* calibration of XUV spectrometers [126] showed, that it is necessary to use the broadening by a near-visible laser pulse and its pedestal for the observation of singly excited 1s*n*p states of helium. They used the the VLS grating model as it is done in the experiments presented here and reach almost the same resolution. They observe the same structures as presented in Fig. 4.3 for zero VIS intensity.

In the following we will discuss the structure for non-zero VIS intensities. In the structure around the 1s2p state for the energies higher than the position of the 1s2p state, the formation of laser-dressed states is visible. For intensities above $0.5\,\mathrm{TW/cm^2}$ the laser-dressed states repel each other, leading to a shift towards higher energies. These laser-dressed states have also been observed in experiments by the group of Steve Leone [72,140]. They find that the 1s3s state at 22.92 eV and the 1s3d state at 23.07 eV are both dressed by the VIS laser pulse and form the light-induced states "1s3s$-\gamma_{\mathrm{VIS}}$" and "1s3d$-\gamma_{\mathrm{VIS}}$". Around the same intensity as these laser-dressed states, the structure at 22.15 eV appears. It is identified as three laser-dressed states which lie close to each other. One is the dressed state "1s2s$+\gamma_{\mathrm{VIS}}$" , the second the dressed state "1s4s$-\gamma_{\mathrm{VIS}}$" and the other the dressed state "1s4d$-\gamma_{\mathrm{VIS}}$". The fact that these laser-dressed states also occur for negative time delays (VIS pulse first) in the time-delay scans for intensities above $0.5\,\mathrm{TW/cm^2}$ hints that the copropagating VIS pulse from the HHG is not filtered out completely, thus leading to a complex mixture of laser dressed states in the intensity scan. At the same intensity as the state "1s2s$+\gamma_{\mathrm{VIS}}$" becomes visible, the original Lorentzian profile of the 1s2p line changes to an asymmetric Fano line shape.

The 1s3p state also shows a splitting, but meaningful interpretation fails due to the high noise level in this energy range. When the ratio between measurement and reference $\frac{I}{I_0}$ is considered for the calculation of OD shown in the figure (see chapter 3.4.1), the noise level is high at that energy as I_0 is almost zero. The reason for the low intensity of the high harmonic spectrum in the energy range around 23 eV is that the HHG process did not produce a single attosecond pulse but a pulse train for these comparably small photon energies between 20 eV and 25 eV. As a result the high harmonics are separated and energy regions with almost no harmonic light lead to a high noise level and almost no measurable signal of the resonances therein.

With increasing VIS intensity, the absorption line shapes for the higher excited 1s*n*p ($n \geq 4$) states are altered, while their energy position stays constant (which will be discussed in chapter 4.1.2). Instead, in analogy to the doubly excited states for $n \geq 4$ their asymmetry parameter q is altered by the laser. For zero intensity the profiles are pure Lorentzian. Then above $1\,\mathrm{TW/cm^2}$ they are turned into asymmetric Fano-like profiles, with a low optical density at their lower energetic edge and a high OD at their high-energetic edge, inverse to the natural Fano line shape of the $\mathrm{sp}_{2,3+}$ states. A comprehensive explanation for this behavior and an intuitively accessible picture of underlying physics will be given in the section 4.2.1.

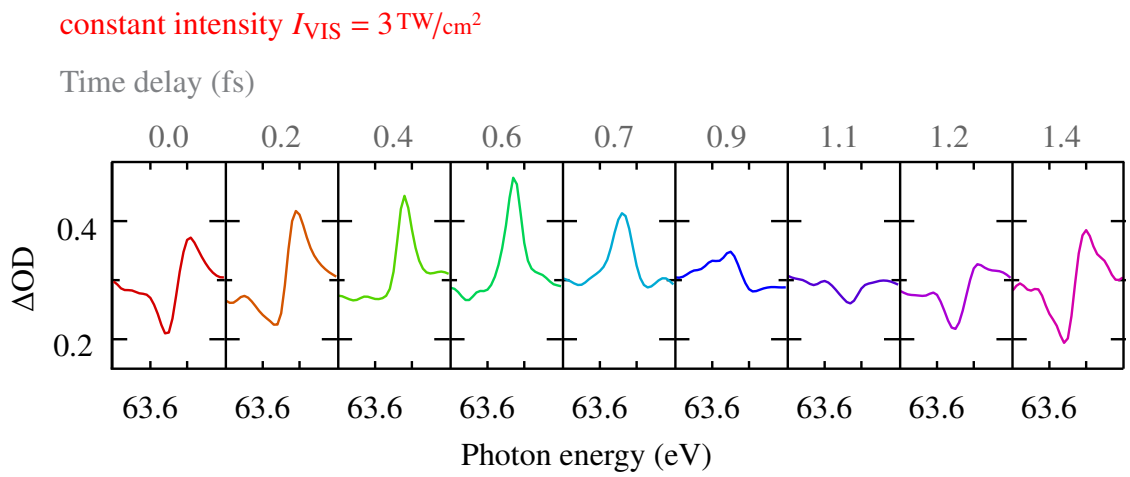

Figure 4.4: Sequence of measured time–delay-dependent absorption spectra of the $sp_{2,3+}$ state. The profile starts with a Fano-like structure with a fitted $q \approx -2.5 \mathrel{\hat{=}} \varphi = 0.24\pi$, then turns into a symmetric Lorentzian profile $\varphi = 0.06\pi$ at one quarter of the VIS laser period. A few hundred attoseconds later it even reaches a positive q parameter of ≈ 0.8 corresponding to a phase $\varphi = -0.6\pi$ before turning back into its initial shape.

4.1.2 Temporal Control

Taking a first look at the time–delay-dependent experimental data (see Fig. 4.4) already shows a periodic alternation in the line profiles calling for a time-dependent Fano phase approach. In the shown sequence of absorption spectra a striking change in the line profiles with a period corresponding to approximately half the optical cycle of the VIS pulse ($T_{VIS}/2 \approx 1.2\,fs$) is clearly visible.

In Fig. 4.5 we show the acquired line shapes as a function of the time-delay between XUV and VIS pulse and the XUV photon energy. The intensity was kept constant at $0.5\,TW/cm^2$. As for the intensity-dependent graphs in the previous section the positions of the unperturbed autoionizing $sp_{2,n+}$ states are labeled on top of the graph.

For negative time delays the well-known Fano line shapes are measured. For the line shapes of the $sp_{2,n+}$ states with $n \geq 4$ no time-delay dependence is visible. A fast oscillation with time delay is present for the 2s2p and the $sp_{2,3+}$ state between 0 fs and 25 fs. The oscillation period is 1.2 fs, corresponding to $T_{VIS}/2$. Additionally the 2s2p line is split up for time delays between −2 fs and 30 fs. It is connected to the Autler–Townes splitting due to the coupling between the 2s2p and the "$2p^2 - \gamma_{VIS}$" (see chapters 2.3 and 3.4.2).

Another weak line is visible at a XUV photon energy of 62.8 eV for time delays between −10 fs and 15 fs. It is identified as the absorption line corresponding to the $sp_{2,3-}$ state. The $2p^2$ state with an energy of 62.06 eV is not visible, as it is not accessible from the ground state due to symmetry reasons.

To further investigate the fast oscillation visible for the $sp_{2,3+}$ state between 0 fs and 25 fs, we now display in Fig. 4.6 the detailed view on area 1 (white rectangle) of Fig. 4.5. As

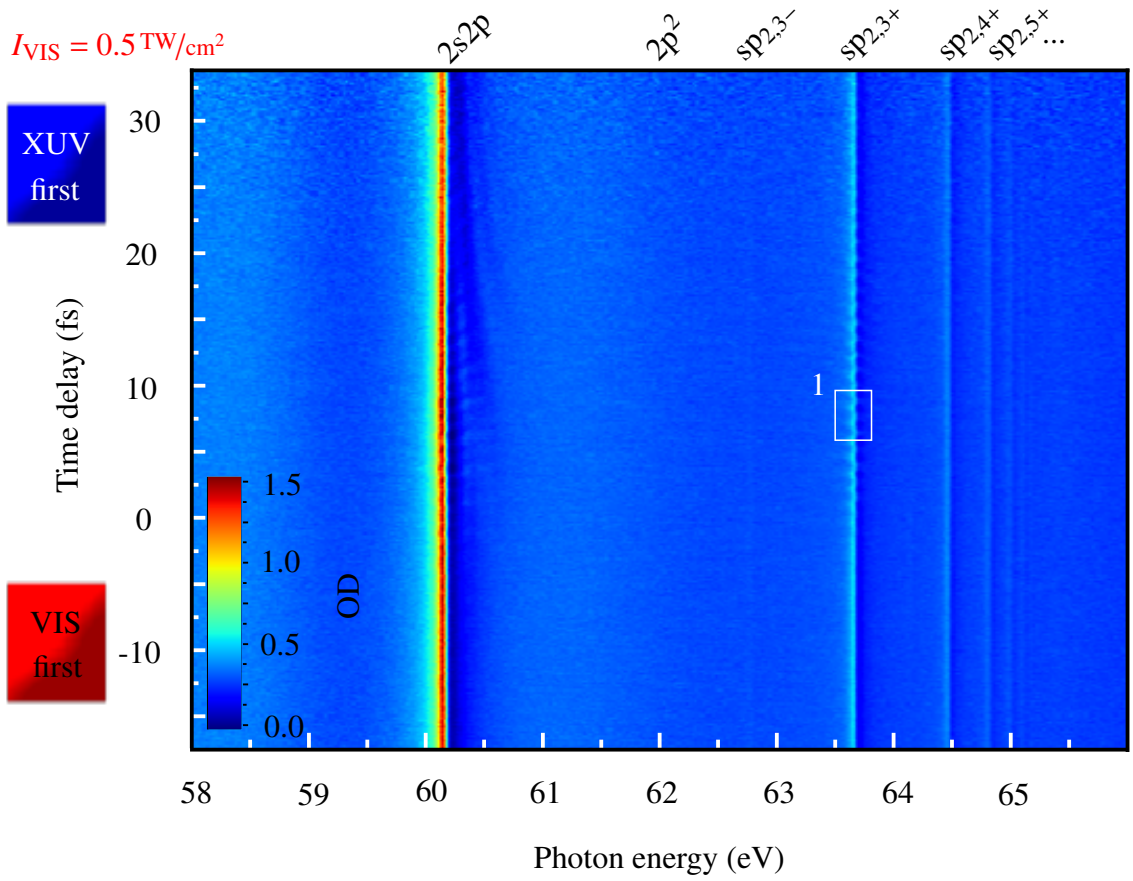

Figure 4.5: Absorption (OD) in the energy range between 58 eV and 66 eV for different time delays between XUV and VIS pulse. A fast oscillation of the $sp_{2,3+}$ state is visible. Also the 2s2p state shows a slight oscillation with the time delay. The position of the $2p^2$ state at 62.06 eV is marked, as it plays an important role in resonantly coupling the 2s2p and the $sp_{2,3+}$ state. Area 1 (white solid rectangle) marks the region where lineouts are taken for further analysis.

we are interested in the line-shape modifications of the $sp_{2,3+}$ state, we subtracted the background absorption $\sigma_0(\omega)$ for this detailed view to enhance the contrast. The black trace in the center of Fig. 4.6 connects the maxima of each spectrum. Despite the fact, that this maxima trace is oscillating with the period of half an optical cycle ($\hat{=}$ 1.2 fs), the energy position of the state is constant for the VIS peak intensity of 0.5 TW/cm² and an energy resolution of 20 meV. In fact, the only parameter altering periodically with the time delay in this graph is the line shape asymmetry. For example, the line shape for a time delay of 7 fs is symmetric, while the line shape for 7.5 fs shows a strong asymmetry. This time-dependent change of the line shape will be subject of chapter 4.3.5.

As already mentioned, the energy position of the $sp_{2,3+}$ state in Fig. 4.6 is constant as a function of time delay, while the line shape oscillates with a period of half an optical VIS cycle. For a VIS peak intensity of 0.5 TW/cm² a shift of the absorption maximum of the $sp_{2,n+}$ states with $n \geq 4$ is below the energy resolution of 20 meV. For higher VIS pulse intensities a shift of the maximum of the $sp_{2,n+}$ states with $n \geq 4$ is resolved. Figure 4.7 shows the line shapes between 62 eV and 66 eV for different time delays between XUV

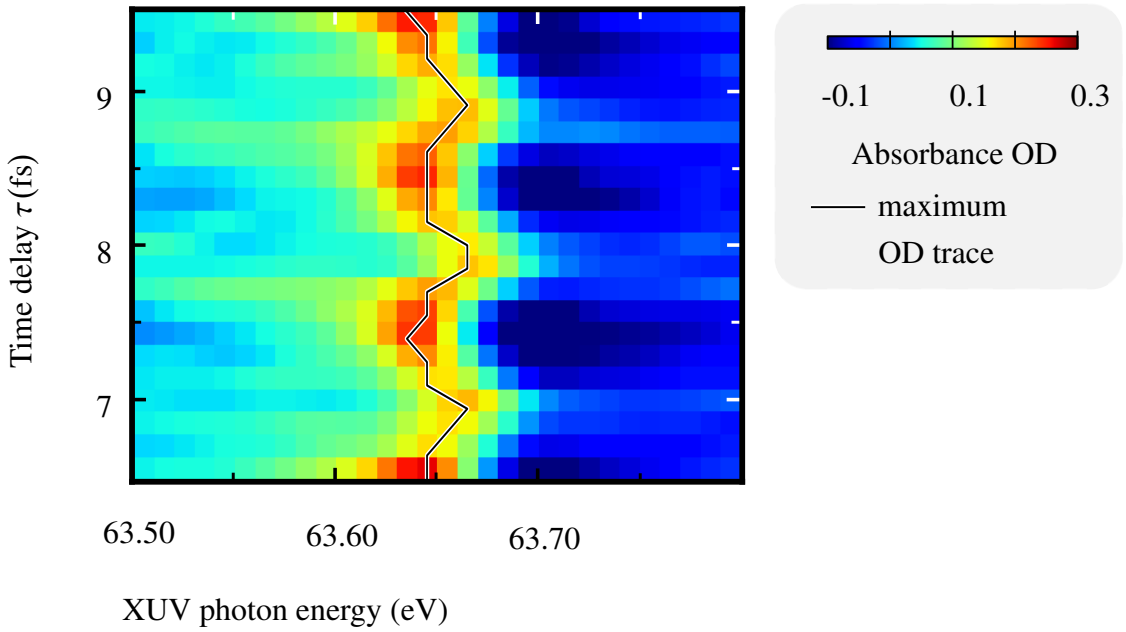

Figure 4.6: Measured Fano resonance absorption spectrum near the He $1s^2 \rightarrow sp_{2,3+}$ transition for varying time delay. The VIS intensity was set to $0.5 \times 10^{12}\,\mathrm{W/cm^2}$. Note that the OD in this plot is given relative to the nonresonant background (which has been subtracted). The maxima of each of the spectra are also highlighted by the black solid oscillatory trace. The oscillation of the maxima is due to a line-shape change while the resonance energy remains constant.

and VIS pulse which was set to an intensity of $2\,\mathrm{TW/cm^2}$. The absorption maxima of the $sp_{2,n+}$ states with $n \geq 4$ show a shift to higher energies. As a guide to the eye, the original (unperturbed) energy position of maximum of the $sp_{2,4+}$ state is indicated by the vertical white dashed line. The period of the absorption maximum change is much lower and is not connected to the optical cycle of the VIS pulse. For the time delay range between 0 fs and 25 fs the maximum is shifted towards higher energies. This shift is below 100 meV. Panel b) compares lineouts of panel a) for different VIS pulse time delays in the energy range of the $sp_{2,4+}$ state and the $sp_{2,5+}$ state. For negative time delays (the VIS pulse arrives before the XUV) the unperturbed Fano line shape is measured (black solid line). For a time delay of +5 fs the line shape (blue solid line) features a symmetric Lorentzian, as it was shown for the intensity scan (compare to Fig. 4.1 of the previous section). The maxima of the curves are different, albeit the energy position of the state is not shifted by the VIS laser pulse or its pedestal. If the time delay of the VIS pulse is 30 fs, which is larger than 30% of the lifetime τ_{life} of the state ($\tau_{\mathrm{life}}(sp_{2,3+}) = 80\,\mathrm{fs}$), the line shape (red solid line) features a Fano profile again.

These time-dependent effects displayed here, as well as the intensity-dependent effects presented in the previous section are understood in our model based on Ugo Fano's theory [34] where he described the asymmetry in unperturbed doubly exited states. In our model, Fano's theory is generalized to also explain effects dependent on the time delay and the intensity of a laser pulse following the excitation for both singly and doubly excited states. The key to this extension of the original Fano theory is that the VIS pulse perturbs the system right at the onset of the polarization decay.

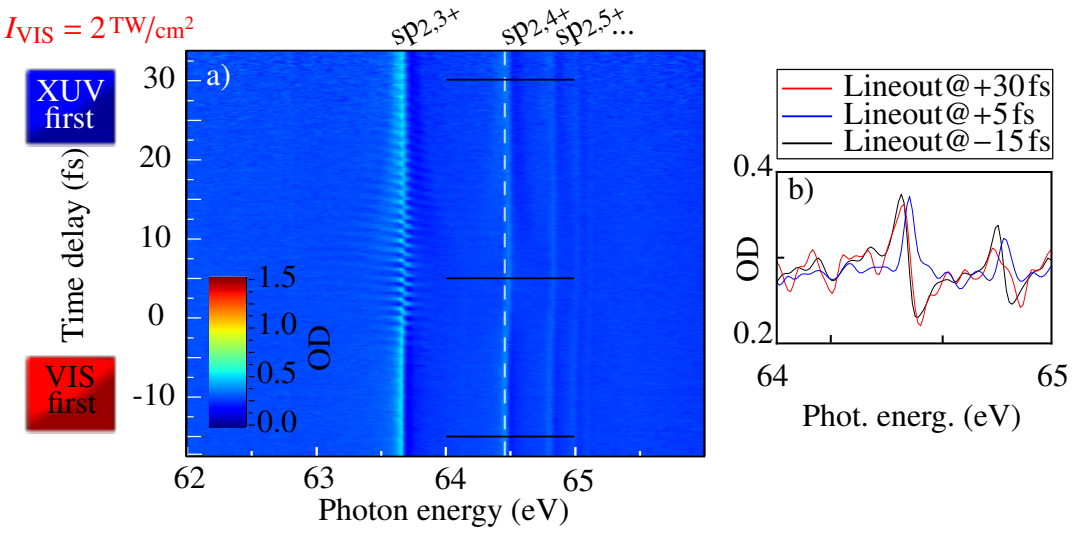

Figure 4.7: a) Line shapes in the energy range between 62 eV and 66 eV for different time delays between XUV and VIS pulse. The intensity of the VIS pulse was set to $2\,TW/cm^2$. A fast oscillation with time delay is visible for the $sp_{2,3+}$ state changing its line shape periodically. While the lines at higher photon energy show no oscillation a slight shift of their maxima to higher energies is visible for the time delay range from −5 fs to 25 fs. This shift is indicated for the $sp_{2,4+}$ state by the white dashed line starting at the maximum of the unperturbed $sp_{2,4+}$ profile. The 3 horizontal black solid lines ranging from 64 eV to 65 eV correspond to the lineouts shown in b). The lineout at −15 fs (black solid line)features the unperturbed Fano line shape. If the VIS pulse arrives shortly (+5 fs) after the XUV, the line shape (blue solid line) changes to a symmetric Lorentzian, in consistency with the intensity scan (see Fig. 4.1). Note, that the maximum of the absorbance shifted despite the fact, that the energy position remained constant. If the VIS pulse arrives later than 10% of the lifetime of the state, in this case +30 fs, the line shape (red solid line) yields an asymmetric Fano-like profile, again.

4.2 General Fano Phase Formalism

Having presented the line-shapes changes as a function of VIS pulse intensity and time-delay in the experimentally measured data, we now explain how to control absorption in general. To this end, the necessary theoretical framework is presented and we derive an analytical formula for the dipole-response function of a system excited by an infinitesimally short (δ-like) XUV flash and a subsequent interaction with a short VIS laser pulse. We elucidate the switching from a Fano line shape into a Lorentzian one and *vice versa* by tuning the VIS laser intensity or the time delay between the XUV and the VIS pulse. Moreover, we will describe how absorption is even transformed into emission.

4.2.1 Time Independent Fano-Phase Formalism

The spectral line profile is linked to the imaginary part of the spectral dipole response, $\sigma(\omega) \propto \Im[d(\omega)]$. As shown in chapter 2.1.2, the origin of the asymmetric line shape of the

Fano resonance is a shift in phase of the exponentially-decaying temporal dipole response with respect to the Lorentzian dipole response.

To model a line shape, it is sufficient to take into account a single atomic bound–bound and the corresponding continuum transition. In this approximation, the dipole response of the instantaneous excitation of the system is semi-classically described by

$$\tilde{d}(t) \propto \imath \left[c \cdot \delta(t) + \frac{\Gamma}{2} \mathrm{e}^{-\frac{\Gamma}{2}t} (q+1)^2 \mathrm{e}^{\imath\omega_\mathrm{r} t} \mathrm{e}^{\imath\varphi(q)} \right] \theta(t), \tag{4.2}$$

where the δ-term represents the instantaneous response of the $N = 1$ continuum with amplitude c and the second term describes the decaying discrete state of width Γ, oscillating with the resonance frequency ω_r. Here, q is the asymmetry parameter as defined in Equ. 2.8. The additional phase $\varphi(q)$ results from the interaction between the energetically degenerate bound–bound and bound–continuum transition. For the special case of $\varphi = c = 0$, a Lorentzian dipole-response function is obtained. Otherwise, the line shape deviates from a symmetric profile. We note that φ is expressed using the asymmetry parameter q of the line shape (see Equ. 2.19).

In turn, this relation can be inverted allowing to map a phase shift into the Fano q parameter [2] via

$$q(\varphi) = \imath \left(\frac{1 + \exp(\imath\varphi)}{1 - \exp(\imath\varphi)} \right) = -\cot(\varphi/2). \tag{4.3}$$

In other words, the shape of the resonance is determined by the phase φ. This implies that if the phase of the dipole response is altered, the interference pattern of the excitation pulse and the dipole emission is changed.

In the experiment, we induce a change of the phase φ by the VIS laser pulse temporally after the XUV excited the helium atoms. This phase change is considered to happen instantaneously on the time scale of the dipole response if the latter lives much longer than the VIS pulse duration. We call this instantaneous phase change a "phase kick". Such a "phase kick" changes the dipole response function and thereby the line profile as illustrated in figure 4.8.

For the validity of the above description, it is necessary that the VIS pulse arrives immediately after the XUV light has excited the dipole. Notably, the above description is applicable to any system with a lifetime longer than the duration of the interaction.

4.2.2 Physical Origin of the Phase Shift

To understand how the VIS laser pulse may induce a phase shift, it is necessary to recall the meaning of the phase of a quantum mechanical state. For a time-independent system the wave-function $|\psi(t)\rangle$ of a state with energy in atomic units $E_\mathrm{r} = \omega_\mathrm{r}$ is in the Schrödinger picture given by

$$|\psi(t)\rangle = e^{-\imath\varphi(t)} |\psi_{E_\mathrm{r}}\rangle, \qquad \varphi(t) = -\omega_\mathrm{r} t. \tag{4.4}$$

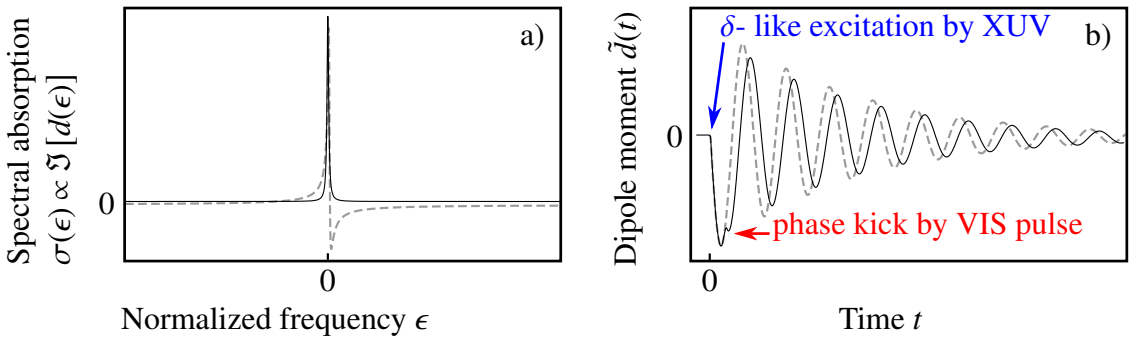

Figure 4.8: a) A schematic illustration how an asymmetric Fano line profile with $q = -2.54$ corresponding to a phase $\varphi = 0.24\pi$ (grey dashed line) turns into a symmetric Lorentzian profile with $\varphi = 0$ (black solid line), when the phase of the decaying dipole is altered by a "phase kick" of -0.24π induced by the VIS laser pulse [marked by the red arrow in b)]. Note, that the exponentially decreasing envelope, due to the fact that the system radiates energy with a lifetime of hundreds of femtoseconds, lives on a much longer timescale than the oscillation period of $\tilde{d}(t)$ which is less than 60 as. To show both in one graph, the oscillation period is enlarged by three orders of magnitude. Note also, that it is important that the "phase kick" happens right at the beginning of the decay, within $\approx 1‰$ of the lifetime.

where $|\psi_{E_r}\rangle$ denotes an eigenstate of the Hamiltonian. We note that the unperturbed phase is defined by the energy of the state. The Hamiltonian $\mathcal{H}$, which determines the energy, contains the electromagnetic (Coulomb) potential. Slightly changing this potential by adding a weak external electromagnetic field alters the life time and the energy of the state. This energy shift is known as a dynamical Stark shift or alternating current (AC) Stark shift [68, 69]. The AC Stark shift in our system is induced by a laser pulse that is short in comparison with the life time $\tau_l = 1/\Gamma$ of the state [62] and it adds an additional contribution to the phase φ in Equ. 4.4.

Qualitatively, this is easily understood in a semiclassical picture[2]. To this end, we consider a free electron in an infinitely long, coherent and monochromatic electromagnetic field of field strength $\mathcal{E}_{\text{Laser},0}$ and frequency ω_{Laser}[3].The electron is driven by the electric field resulting in a quivering motion. The average energy $\Delta\omega$ gained by this wiggling compared to the field-free case is called ponderomotive energy U_P. It is expressed via

$$\Delta\omega = U_\text{P} = \frac{(\bar{v}(t))^2}{2m} = \frac{e^2 {\mathcal{E}_{\text{Laser},0}}^2}{4m{\omega_{\text{Laser}}}^2} \tag{4.5}$$

where $\bar{v}(t)$ is the velocity average over one optical cycle, e is the elementary charge and m the electron mass, respectively (which are actually both set to 1 in atomic units, see appendix A). A similar energy shift is expected for a bound electron and must be added to the Coulomb term in the Hamiltonian if an atom interacts with a monochromatic field. The deeper the state lies within the Coulomb potential the less it is affected by the external

[2]The linear Stark shift can be explained classically, while the classical pictures of the quadratic and dynamical Stark effects are only valid if the correspondence principle is applicable [141]

[3]We start with the monochromatic case, which, of course, is not applicable to the short VIS pulse, but helps to understand the physical processes in a much simpler picture, before we consider the case of a short pulse. Additionally, it does explain effects arising from the long-lasting VIS pulse pedestal.

field. As a result, the actual energy change that is induced by the monochromatic field differs from U_P in Equ. 4.5. In turn, the higher the states lies in the Coulomb potential (e.g. Rydberg states) the more appropriate becomes the approximation of the free electron and the more the energy shift approaches U_P. It is added to the phase evolution (see Equ. 4.4)

$$\varphi(t) = -(\omega_r + \Delta\omega)t. \tag{4.6}$$

Inserting this in the time-dependent dipole response function for a two-level system (see chapter 2.3) yields

$$\tilde{d}^{(0)}(t) \propto \imath \left|\mu_{ge}\right|^2 e^{-(\Gamma_{lb}/2)t} e^{\imath(\omega_r+\Delta\omega)t}\theta(t) \tag{4.7}$$

with the dipole expectation value μ_{ge} between the ground state and the excited state. In addition to the constant energy shift $\Delta\omega$, another consequence of the monochromatic laser field is the reduced life time of the state resulting in the laser-broadened (lb) line width Γ_{lb}. A Fourier transformation of $\tilde{d}^{(0)}(t)$ yields the expected Lorentzian absorption line shape, which is the spectral dipole response of a discrete state (see Fig. 2.1 on page 6). Note, that the Lorentzian absorption line is now centered around the energy $\omega_r + \Delta\omega$.

Having understood the simplified picture of the monochromatic case, we now consider the case of laser pulses. In the time domain, this leads to an explicitly time-dependent energy shift $\Delta\omega(t)$ in the phase evolution given in Equ. 4.6. However, the pulse duration $\Delta\tau_{Laser}$ of the VIS laser is much shorter than the lifetime of the state. Therefore, the laser-induced effects on the state are summarized in a total phase shift

$$\Delta\varphi = -\int_{\Delta\tau_{Laser}} \Delta\omega(t')\mathrm{d}t' \tag{4.8}$$

with the integral running over the duration of the VIS laser pulse $\Delta\tau_{Laser}$ (if the state is populated during that time).

In the limit of δ–function-like pulses (both excitation and phase-shifting pulse) impinging at time $t = 0$, the time-dependent-dipole response function reads

$$\tilde{d}^{(\delta)}(t) \propto \imath \left|\mu_{ge}\right|^2 e^{-(\Gamma/2)t} e^{\imath\omega_r t} e^{-\imath\Delta\varphi}\theta(t). \tag{4.9}$$

At first sight, $\tilde{d}^{(0)}(t)$ and $\tilde{d}^{(\delta)}(t)$ look similar, but they feature some important differences. In Equ. 4.7 the decay width of the state Γ_{lb} is broadend by the laser and an AC-Stark shift $\Delta\omega$ is added to the phase evolution. By contrast, the decay width and the energy of the state in the case of a δ-pulse (Equ. 4.9) remain unchanged, while the phase is changed by $\Delta\varphi$. Remarkably, the dipole response due to a δ-like laser perturbation (see Equ. 4.9) is similar to the time-dependent dipole response as derived by the Fano approach from strong coupling between continuum states and discrete quantum states (see Equ. 4.2 and the derivation in chapter 2.1.2). By comparing both expressions, we identify the phase shift $\Delta\varphi$ induced by the laser pulse as the Fano phase $\varphi(q)$.

4.2.3 Calculation of the Line-Shape Changes

By calculating the phase shift $\Delta\varphi$ for a known laser pulse, we can predict the change of the q parameter of the observed line shape, via the mapping presented in Equ. 4.3. We perform this calculation for the highest-lying states of the doubly excited $sp_{2,n+}$ series of helium, i.e. for $n \geq 4$. For these states, the inner electron is mainly located close to the nucleus. The outer electron, however, is more likely to be found far away from the nucleus. So we consider the p-electron as asymptotically free [3] and calculate the change in energy by the Lorentz force from the time-dependent laser pulse $\mathcal{E}_{\text{Laser}}$ with envelope $F_{\text{L}}(t)$ in atomic units using the instantaneous ponderomotive potential $U'_{\text{P}}(t)$:

$$\Delta\omega(t) = U'_{\text{P}}(t) = {}^1\!/_2(\bar{v}(t))^2 \tag{4.10}$$

where $\bar{v}(t)$ is the average of the instantaneous velocity $v(t)$ during the period of one optical cycle T, as we use the instantaneous ponderomotive potential $U'_{\text{P}}(t)$ for the laser pulse envelope $F_{\text{L}}(t)$. The phase shift $\Delta\varphi$ is finally calculated using

$$\Delta\varphi = -\int_{\Delta\tau_{\text{Laser}}} U'_{\text{P}}(t')\mathrm{d}t' \tag{4.11}$$

The total phase $\varphi = \varphi_{\text{orig}} + \Delta\varphi$ is the sum of the laser-induced phase shift $\Delta\varphi$ and the original phase[4] φ_{orig} induced by the strong coupling between the continuum and the discrete quantum state. Interestingly, the laser-induced phase shift $\Delta\varphi$ (see Equ. 4.11) is always negative as the square of the time integrated VIS envelope will always be positive. Therefore, the final q parameter will always be smaller than the original parameter q_{orig} (see Fig. 4.10), up to the branch point $\varphi = 0$, where the function jumps from $-\infty$ to $+\infty$.

In the next paragraph we show that the above theoretical description is in excellent agreement with the experimental data if a pulse is used which is short compared to the decay time of $\tilde{d}(t)$.

4.3 Experimental application of the Fano Phase Formalism in Helium

The theoretical behavior of a decaying dipole under the influence of a δ-like pulse has been described in the previous paragraph. In the following, we apply the knowledge of the developed Fano-phase formalism to quantify the derived phase shift by inserting the laser-pulse characteristics of our laser system and calculating the expected optical density of the helium target gas.

The line shapes observed for the unperturbed singly excited 1snp series in helium feature a symmetric Lorentzian absorption profile (see chapter 2.5). For the case of the doubly-excited $sp_{2,n,+}$ series, an asymmetric optical-density profile is observed. As explained

[4]The original phase φ_{orig} is calculated from the original Fano line shape asymmetry parameter q_{orig} using $\varphi_{\text{orig}}(q_{\text{orig}}) = 2\arg(q_{\text{orig}} - \imath)$ (see Equ. 2.19).

above, each excited state $|\mathrm{sp}_{2,n+}\rangle$ of the doubly-excited resonance series interacts with the $N = 1$ continuum $|1\mathrm{s}\varepsilon\mathrm{p}\rangle$. This interaction induces a "temporal phase shift" to the natural dipole moment. The q parameter resulting from this interaction can be determined using (see Equ. 2.8)

$$q = \frac{\langle \mathrm{sp}_{2,n+}|\hat{\mathbf{T}}|1\mathrm{s}^2\rangle}{\pi V_E^* \langle 1\mathrm{s}\varepsilon\mathrm{p}|\hat{\mathbf{T}}|1\mathrm{s}^2\rangle} \tag{4.12}$$

with $\hat{\mathbf{T}}$ denoting the perturbative coupling induced by the XUV light and V_E the configuration interaction term. The absorption cross section is given by (see Equ. 2.3 and Equ.2.10)

$$\sigma_\mathrm{Fano} = \sigma_0 \frac{(q+\epsilon)^2}{1+\epsilon^2} \propto \Im\left(d(\omega)\right) \tag{4.13}$$

with the reduced energy $\epsilon = 2^{(\omega-\omega_\mathrm{r})}/\Gamma$ and the spectral-domain dipole response $d(\omega)$. In the region around the $\mathrm{sp}_{2,n+}$ states series in helium, the absorption cross section is a sum of two parts [28]:

$$\sigma_\mathrm{Fano} = \sigma_0(\omega) + \sigma_\mathrm{r}(\omega), \tag{4.14}$$

where $\sigma_0(\omega)$ is the non-resonant offset, arising from the continuum absorption. The second part is the resonant absorption cross section $\sigma_\mathrm{r}(\omega)$ due to the discrete bound two-electron states. As we extract the resonant part from the experimental data by subtracting the background absorption $\sigma_0(\omega)$ (known from synchrotron data), we only consider the resonance absorption cross section $\sigma_\mathrm{r}(\omega)$ in the following.

For the theoretical calculation of the resonant absorption cross section we use the relation given in [28]

$$\sigma_\mathrm{r}(\omega) = \sum_\mathrm{n} \sigma_\mathrm{r}^{(\mathrm{n})}(\omega) = \sum_\mathrm{n} \mu_{(\mathrm{n})}^2 \left(\frac{\sigma_\mathrm{Fano}^{(\mathrm{n})}(\omega)}{\sigma_0^{(\mathrm{n})}(\omega)} - 1 \right) \tag{4.15}$$

where $\mu_{(\mathrm{n})}^2$ is the strength parameter of the remaining resonant part [2, 28] and is listed in Tab. 2.1 in appendix C.2. The parametrization in Equation 4.15 is similar to the one used by Ugo Fano [34]. The background absorption is assumed to be constant across each resonance at the respective energies $\hbar\omega_\mathrm{r}$, i. e. $\sigma_0^{(\mathrm{n})}(\omega) = \sigma_0^{(\mathrm{n})}$ and the sum runs over all involved discrete states. Using $\sigma_\mathrm{Fano}^{(\mathrm{n})} = \sigma_0^{(\mathrm{n})} \frac{(q_{(\mathrm{n})}+\epsilon)^2}{1+\epsilon^2}$ (see Equ. 2.10) the resonant absorption cross section reads:

$$\sigma_\mathrm{r}(\omega) = \sum_\mathrm{n} \mu_{(\mathrm{n})}^2 \left(\frac{(q_{(\mathrm{n})}+\epsilon)^2}{1+\epsilon^2} - 1 \right). \tag{4.16}$$

Using this equation, we can now calculate the theoretical line shapes and compare them to the experimentally measured ones.

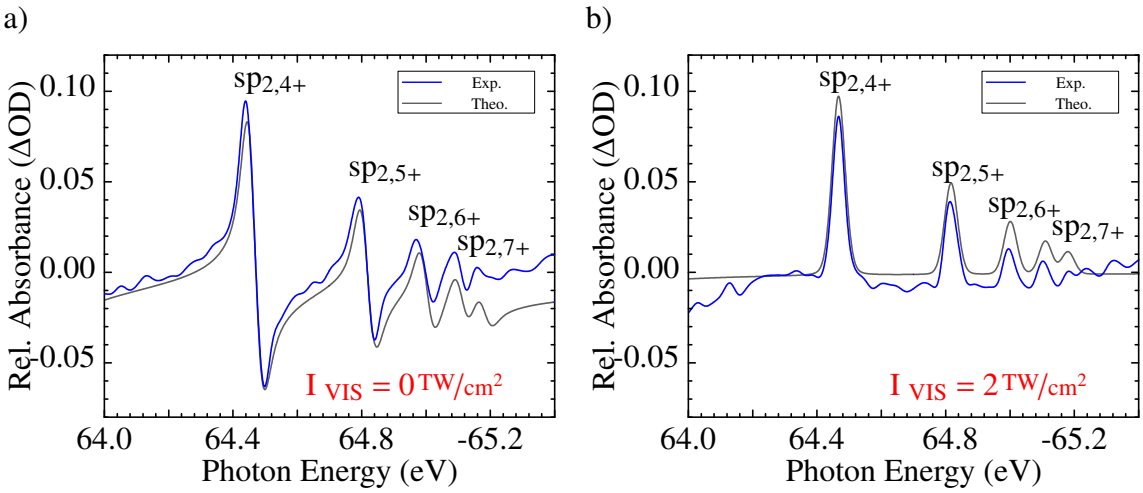

Figure 4.9: Transforming asymmetric Fano spectral absorption lines into symmetric Lorentzian absorption peaks in doubly-excited He. a): Unperturbed absorption spectrum of the $sp_{2,n+}$ series in helium. The well-known Fano absorption profiles are observed in the transmitted spectrum of a broad-band attosecond pulse in the absence of the VIS pulse. The blue solid line is a line out from Fig.4.2 at zero VIS intensity, while the solid black line is calculated using the values from Tab. C.2. b): The absorption spectrum of the $sp_{2,n+}$ series when coupled by the VIS pulse immediately after the excitation. The Fano absorption profiles are converted to Lorentzian profiles. The blue solid line is a line out from Fig.4.2 at a VIS intensity of $2\,\mathrm{TW/cm^2}$. The 7 fs VIS pulse follows the δ-like excitation with a time delay of 5 fs. The solid black line represents Lorentzians at the resonance positions of the original Fano lines, calculated from Tab. C.2.

4.3.1 Comparison of the calculated and measured absorbance for the $sp_{2,n+}$ series

The calculated photo-absorption cross sections for the $sp_{2,n+}$ series are based on the resonance energy ω_r, line width Γ and dipole-transition strength parameter $\mu^2_{(n)}$ for the doubly excited states which are listed in Tab. C.2 in appendix C.2. As the experimentally observed line width not only depends on the decay time, but also on the resolution of the recording spectrometer, the calculated cross sections are convoluted with a normalized Gaussian with a standard deviation of 20 meV for XUV photon energies around 60 eV (see page 36 in chapter 3.2.4).

For the following discussion of the phase control of the dipole response it is important that the q parameter in the amplitude factor (q^2+1) in Equ. 4.2 remains constant with $q = q_{\mathrm{orig}}$, as defined by the original resonance. As a direct consequence it is possible to achieve a situation where OD < 0, which corresponds to a gain of transmitted light at the resonance energy[5], which is not allowed for a field-free Fano resonance where OD ≥ 0 for all photon energies.

Figure 4.9 compares the measured (solid blue line) and the theoretical OD (solid grey line) for the doubly excited series. The spectrum in subplot a) shows the line profiles of

[5]More precisely: distributed around the resonance energy with a Lorentzian probability distribution.

the doubly excited series from $sp_{2,4+}$ to $sp_{2,7+}$ without the VIS laser pulse. The Fano line shapes are clearly visible. For the spectrum in Fig. 4.9 b) the VIS laser intensity was set to $2\,\mathrm{TW/cm^2}$. The asymmetric Fano line shapes have been altered to symmetric Lorentzian line shapes. The natural autoionization life time of the $sp_{2,4+}$ (a few hundred femtoseconds, see table 2.1) is much larger than the VIS pulse duration. Therefore the "phase kick" picture as described in section 4.2.1 is applicable. Using the $q(\varphi)$-mapping (see Equ. 4.3) we can calculate the change of the line shape parameter due to the "phase kick". As seen from Tab. 2.1 the states from $sp_{2,4+}$ to $sp_{2,7+}$ exhibit original (unperturbed) line shape parameters q_{orig} ranging from -2.55 to -2.58. This original line-shape parameters translates into phases φ_{orig} ranging between$0.240\pi \mathrel{\hat{=}} (0.75)\,\mathrm{rad}$ and $0.243\pi \mathrel{\hat{=}} (0.76)\,\mathrm{rad}$ using $\varphi_{\mathrm{orig}}(q_{\mathrm{orig}}) = 2\arg(q_{\mathrm{orig}} - \imath)$ (see Equ. 2.19). For the photo-absorption cross section of the $sp_{2,n+}$ series the VIS laser pulse causes a phase shift $\Delta\varphi$, which depends on its intensity. We assume that the laser does not, after its interaction, significantly alter neither the energy position of the absorption lines nor the population and the lifetime of each state. We therefore use the same parameters as for the unperturbed case, listed in Tab. C.2. In Fig. 4.9 b) the experimentally obtained OD for the doubly excited helium states under the influence of the VIS laser pulse with a peak intensity of $2\,\mathrm{TW/cm^2}$ is compared to the theoretical OD calculated by the Fano phase formalism shown above and convoluted with the spectrometer resolution. The laser-induced phase shift $\Delta\varphi$ is directly connected to the effective phase $\varphi(q)$ which then relates to the Fano asymmetry parameter. The phase shift $\Delta\varphi$ is calculated assuming a free electron in a 7 fs (FWHM) Gaussian laser pulse with central frequency $\omega_{\mathrm{Laser}} = 1.7\,\mathrm{eV}$ (corresponding to a wavelength of 730 nm). For the measurement of the doubly excited states a peak electric field strength of $\mathcal{E}_{\mathrm{Laser,Peak}} = 3.9 \cdot 10^9\,\mathrm{V/m}$ corresponding to a peak intensity of $2\,\mathrm{TW/cm^2}$ has been used. During the presence of the laser pulse the states experience a ponderomotive shift resulting in a total phase shift $\Delta\varphi = (-0.35 \pm 0.18)\pi \mathrel{\hat{=}} (-1.1 \pm 0.5)\mathrm{rad}$. This phase shift is added to the original phase φ_{orig}. The resulting phase $(-0.11 \pm 0.18)\pi$ is close to zero thus producing the Lorentzian absorption line, as shown in Fig. 4.9 b).

Driving a full 2π phase circle

In the previous paragraph we have shown how to switch a Fano line shape to a Lorentzian one (see Fig. 4.9) by the VIS intensity dependent phase shift $\Delta\varphi$. As the VIS laser intensity is continuously controlled by the iris aperture, so is the phase shift and we can smoothly transform the line shapes into each other. The most interesting line profiles obtained in this way for the doubly excited states of helium starting with the $sp_{2,5+}$ state are shown in Fig. 4.10.

Besides the natural Fano line shape for the case without coupling laser and the Lorentzian line shape obtained for an VIS intensity of $2\,\mathrm{TW/cm^2}$, we now also observe the inversion of the natural line shape at an intensity of $3\,\mathrm{TW/cm^2}$. Furthermore, a window resonance forms at an intensity of $4\,\mathrm{TW/cm^2}$, as shown in Fig. 4.10, where the optical density is purely negative for the $sp_{2,n+}$ states. Note, that the continuum absorption is subtracted, thus the overall absorbance is still positive. We will later show in section 4.3.3 how to turn this into a gain situation in the absence of continuum absorption.

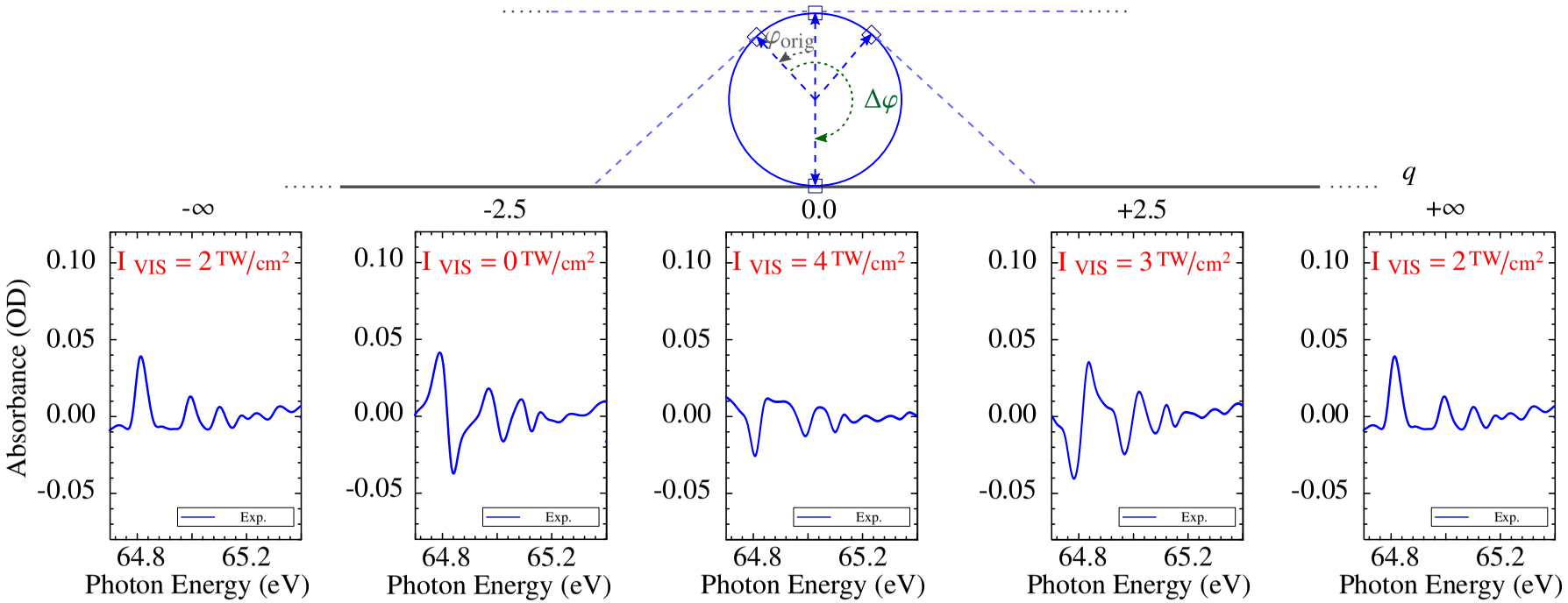

Figure 4.10: Mapping between the temporal response-function phase φ and Fano's q (line-shape asymmetry) parameter. The bijective mapping between the two parameters in the range from $[0, 2\pi]$ is illustrated in analogy to a 2D Riemann sphere (see Fig. 2.4)with a branch cut at 2π. The phase shift $\Delta\varphi$ by the laser is projected via the tangent to the q axis. In turn the unperturbed line shape parameter q_{orig} is mapped to a phase φ_{orig} The experimental proof for the validity of this Fano-phase formalism is shown in form of the measured line shapes of the doubly-excited $sp_{2,n+}$ series for $n \geq 5$ in helium. Shown below the q axis is a sequence of the full data set given in Fig. 4.2. Starting from the unperturbed asymmetric Fano spectral absorption line with $q_{\text{orig}}(sp_{2,5+}) = -2.54 \rightarrow \varphi_{\text{orig}} = 43.5°$ the "phase kick" $\Delta\varphi$ by the VIS laser pulse @ $I_{\text{VIS}} = 2\,\text{TW/cm}^2$ turns the line shapes into symmetric Lorentzian absorption peaks corresponding to $q \rightarrow -\infty$ and $q \rightarrow +\infty$. If the 7 fs VIS pulse is turned to a peak intensity of $3\,\text{TW/cm}^2$, the initial absorption profiles revert their original symmetry now showing a $q = +2.54$. At an intensity of $4\,\text{TW/cm}^2$ the "phase kick" $\Delta\varphi$ shifts the total dipole phase to π, resulting in the special case of a window resonance $q = 0$. If no continuum absorption is present, this can even lead to a gain of photons at the resonance energy (see chapter 4.1.1).

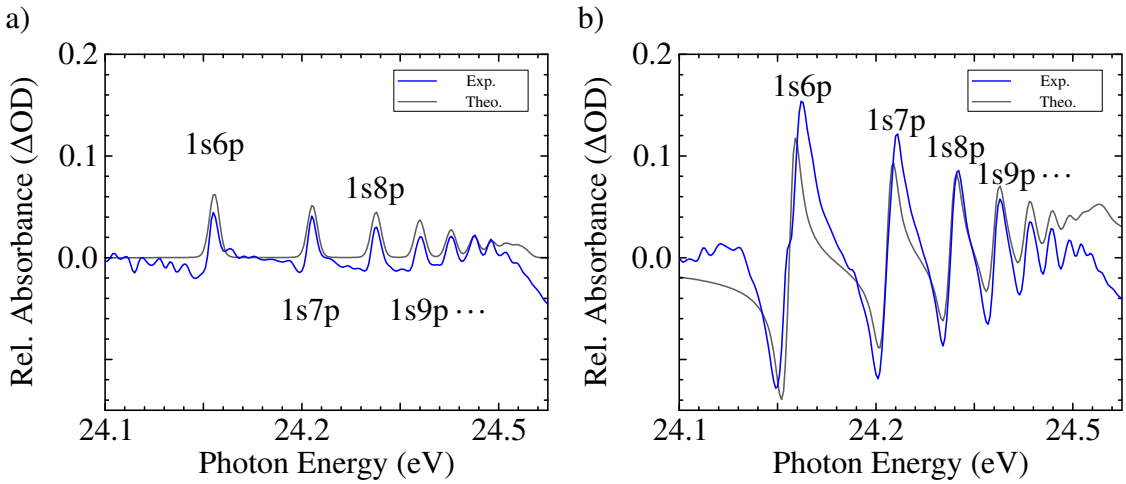

Figure 4.11: Transforming symmetric Lorentzian peaks into asymmetric Fano-like spectral absorption profiles in singly-excited He. a): Unperturbed absorption spectrum of the 1s*n*p series in helium. Lorentzian line shapes are measured in the attosecond-pulse absorption spectrum in the absence of the VIS laser pulse (blue solid line) and calculated using the values from Tab. C.3. b): The measured absorption spectrum (blue solid line) of the states when a VIS pulse at an intensity of 2.1 $\mathrm{TW/cm^2}$ follows immediately after the excitation. The initial Lorentzian absorption profiles are transformed to Fano-like profiles. The 7 fs VIS pulse follows the δ-like excitation with a time delay of 5 fs. The solid black line represents Fano profiles with expected laser-induced $q = 1.49$ at the resonance positions of the original Lorentzian resonances, calculated from Tab. C.3.

4.3.2 Comparison of the calculated and measured absorbance for the 1s*n*p series

To proof that the change of the line shape is really due to the AC Stark shift of the bound state, we now consider the singly excited 1s*n*p series in helium. These states have a natural Lorentzian absorption profile as they decay fully radiatively with no interfering continuum contribution [142]. To this end we expose the singly excited 1s*n*p series in helium to a VIS laser pulse of $4.0 \cdot 10^9\,\mathrm{V/m}$ peak electric field strength ($\hat{=}\ 2.1\,\mathrm{TW/cm^2}$). The subsequent phase shift should then result in an inverse transformation compared to Fig. 4.9 turning the symmetric Lorentzian lines into Fano-like line shapes.

In the absence of the VIS laser field, the well-known absorption spectrum of helium in the 1s*n*p series just below its first ionization threshold at 24.6 eV is measured as shown in Fig. 4.11 a). When the VIS pulse peak intensity is set to $2.1\,\mathrm{TW/cm^2}(\hat{=}\ 4.0 \cdot 10^9\,\mathrm{V/m})$, the symmetric Lorentzian line shapes are turned into asymmetric Fano line shapes, as shown in Fig. 4.11 b). The ponderomotive shift during the presence of the laser pulse is calculated to $\Delta\varphi = (-0.38 \pm 0.19)\pi\ \hat{=}\ (-1.2 \pm 0.6)$rad. As the original phase is zero, the resulting q parameter only depends on $\Delta\varphi$ and is calculated to $+1.49 \pm 0.6$, which is in agreement with the measured line shape in Fig. 4.11 b).

The line broadening in the measured data in Fig. 4.11 b) indicates a reduction of the original lifetime of the states (which is in the nanosecond regime). This reduction occurs due to single-photon ionization in the long-duration pedestals typically accompanying

few-cycle laser pulses (see chapter 2.6.1).

For the calculation of the line profiles of the singly-excited helium series as known from literature, the energy and dipole transition elements are used as listed in Tab. C.3 in Append. C.3. The line widths have been adapted due to broadening by the single-photon ionization in the VIS laser pedestal. For the detector resolution in the energy range from 20 eV to 25 eV, a Gaussian with a standard deviation of 5 meV was used to convolve the calculated profiles.

For the laser-manipulated profile shown in Fig. 4.11 b) the same energy positions and dipole transition elements were used as for the unperturbed case. For all states under the influence of the coupling VIS laser pulse q was set to +1.49.

Small additional line-shape modifications for the 1s6p line and lower-lying states are due to the onset of near-resonant couplings to other bound states. Their description is currently beyond the scope of the phase-shift model introduced in this section.

The ability to control the phase shift imprinted onto the discrete state by a short laser pulse of controlled intensity as shown here has relevance for a complementary understanding of other types of recently observed phase (or temporal) shifts in photoionization [143].

4.3.3 Transforming Absorption into Emission

In the previous sections we have shown how to change the absorption line shape from a Lorentzian into a Fano profile and *vice versa*. We will now extend this control even further by turning absorption into emission.

As we have seen in Fig. 4.10, it is possible to turn the line shapes into window resonances. When no continuum absorption is present, as e.g. for the case of singly excited helium, even a gain situation can be reached. In this case the necessary intensity is around $3\,\mathrm{TW/cm^2}$, as shown in Fig. 4.12, where the binned spectra of the XUV camera are shown for two different VIS pulse intensities. Note, that this is an absolute measurement, including the high harmonic light which passes through the helium target. If the VIS pulse intensity is (almost) zero[6], the Lorentzian absorption lines are visible as dips in the binned spectrum (green dots connected by the green solid line). The increase in the overall intensity towards the $N = 1$ ionization threshold is caused by the increase of the intensity of the high harmonic light passing through the sample, as shown in the full camera chip image in Fig.4.13. For the case of an VIS intensity of $3\,\mathrm{TW/cm^2}$, peaks appear at the energy positions of the 1snp states (blue dots connected by the blue solid line), while the intensity of the harmonic light between the energy positions of the states is lowered. The emission peaks feature Lorentzian line shapes. This means that it is not only possible to change

[6] Almost zero means that the iris is closed that only a a minimal amount of co-propagating VIS light passes the iris, thus ensuring a the line broadening of the 1snp profiles, so they can be resolved by the spectrometer (see section 4.1.1). At such low intensities no Autler-Townes splitting is observed.

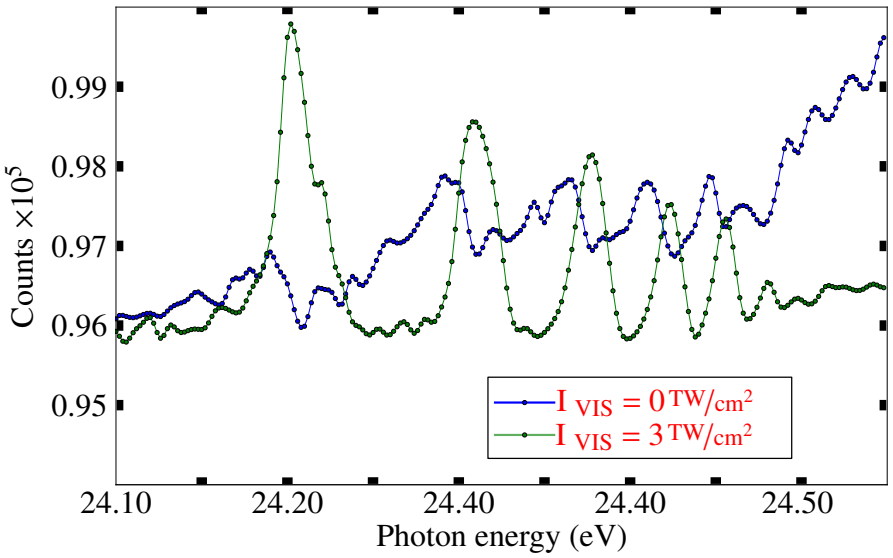

Figure 4.12: Software binning of an acquired XUV spectrum. Shown are the integrals along the vertical axes of the full chip camera pictures shown in Fig. 4.13 and Fig. 4.14. The camera pixels (blue and green dots respectively) have been connected by a spline interpolation as an guide to the eye. In the absence of the VIS pulse (blue dots) a pure Lorentzian absorption line is present. An increase the the overall intensity towards the $N = 1$ ionization threshold is visible due to the intensity increase of the generated harmonic light. If the VIS pulse is set to an intensity of $3\,^{\mathrm{TW}}/_{\mathrm{cm}^2}$, the previously absorbing lines turn into emission (green dots). The line profiles feature Lorentzian shapes and are energetically located at the resonances of the 1snp series.

the line profile, but also to control the sign of the absorption by varying only the phase φ. The mentioned gain is optically induced solely by modifying the phase of the dipole response. We point out that no additional amplitude control or even population inversion of the excited state was necessary.

To explain in more detail how this gain situation is achieved, we start from the singly excited 1snp states. For these states the spectral dipole response is a Lorentzian absorption line (with an unperturbed $\varphi_{\mathrm{orig}} = 0$) in the absence of the VIS pulse. By introducing the laser-controlled tunable phase $\Delta\varphi$ the time-dependent dipole response is described by (see Equ. 4.9)

$$\tilde{d}(t) \propto \mathrm{e}^{-(\Gamma/2)t+\imath(\omega_0 t+\Delta\varphi)} \tag{4.17}$$

resulting in a photo-absorption cross section

$$\sigma_{\mathrm{abs}} \propto \Im(d(\omega)) = \Im\left(\frac{-\epsilon}{1+\epsilon^2}\mathrm{e}^{\imath\Delta\varphi} + \imath\frac{1}{1+\epsilon^2}\mathrm{e}^{\imath\Delta\varphi}\right) \tag{4.18}$$

with the normalized frequency $\epsilon = \frac{(\omega-\omega_{\mathrm{r}})}{\Gamma/2}$ [2]. The absorption cross section σ_{abs} yields negative values when φ departs from zero, corresponding to the absence of the VIS pulse. This is because the negatively-valued (for $\epsilon > 0$) dispersive term $\frac{-\epsilon}{1+\epsilon^2}\mathrm{e}^{\imath\Delta\varphi}$ acquires an imaginary part for $\varphi \neq 0$. The interpretation of this mixing of the dispersive and the absorbing term as a function of φ will be discussed in the next section.

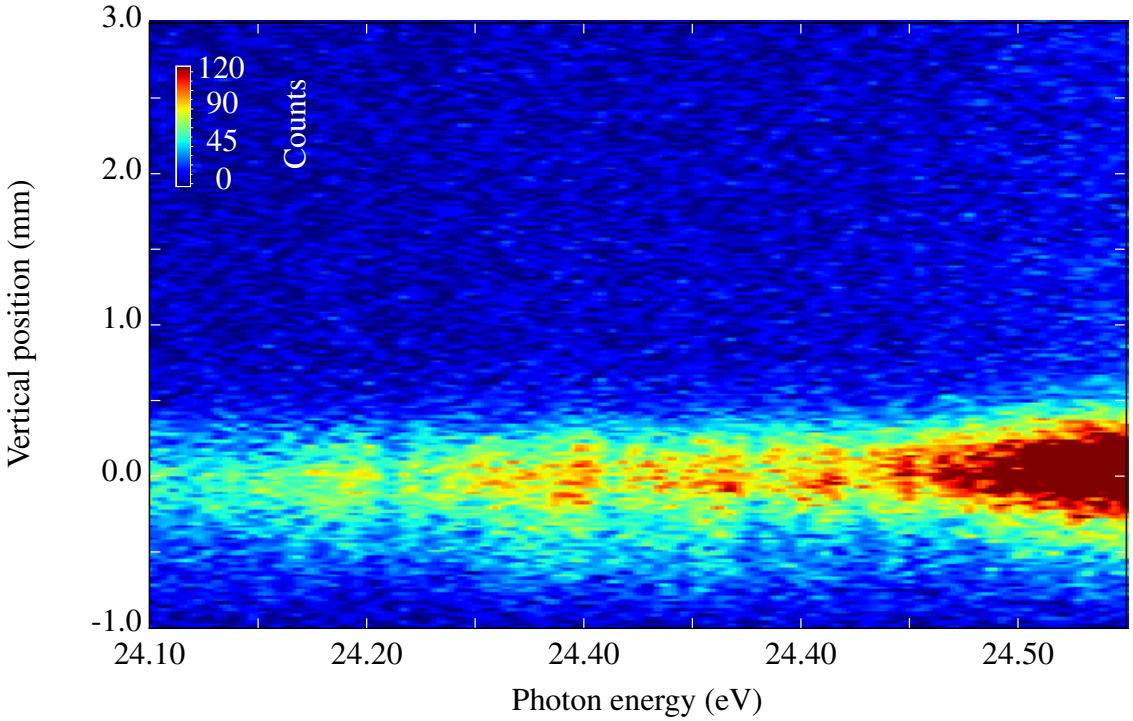

Figure 4.13: Full-chip camera picture of an unperturbed absorption measurement. The x-axis is calibrated in energy and the y-axis is calibrated in the spatial dimensions of the camera chip. The intense part around 0.0 mm height is the harmonic spectrum of the XUV pulse. The iris controlling the VIS laser intensity was closed in a way that the time-delayed VIS pulses did not perturbed the decay of the excited helium dipoles strongly. Nevertheless, a minimal amount of co-propagating VIS light ensures a broadening the lines, so they can be resolved by the spectrometer (see section 4.1.1).

In the beginning of this section, to confirm the laser control and the transformation of absorption into emission, we have shown a binned spectrum for the cases with and without the VIS laser pulse. We will now show the corresponding full camera images, spatially resolved across the vertical axis. In Fig. 4.13 the case without laser control is shown. The structure around the vertical position of 0 mm is the transmitted harmonic light, with the Lorentzian absorption dips at the energy position of the 1s*n*p states. We compare this spectrum to a spectrum where the VIS laser pulse is present (see Fig. 4.14). Note, that both figure have the same color scale. The presence of the laser field clearly enhances the XUV light intensity at the resonance positions of the singly-excited states of helium[7] which are, in the absence of the laser field, absorbing. The intensity of the transmitted harmonic spectrum around the vertical position of 0 mm in Fig. 4.14 decreased compared to to one in Fig. 4.13.

[7] In addition, the bright emission structures appearing at the resonance position of the 1s*n*p series, are spatially separated from the previously absorbing line profiles. This behavior is explained by a spatial gradient of the VIS pulse, as it can be produced by tilting the outer mirror (see section 3.2.2 and Fig. 3.6 therein).

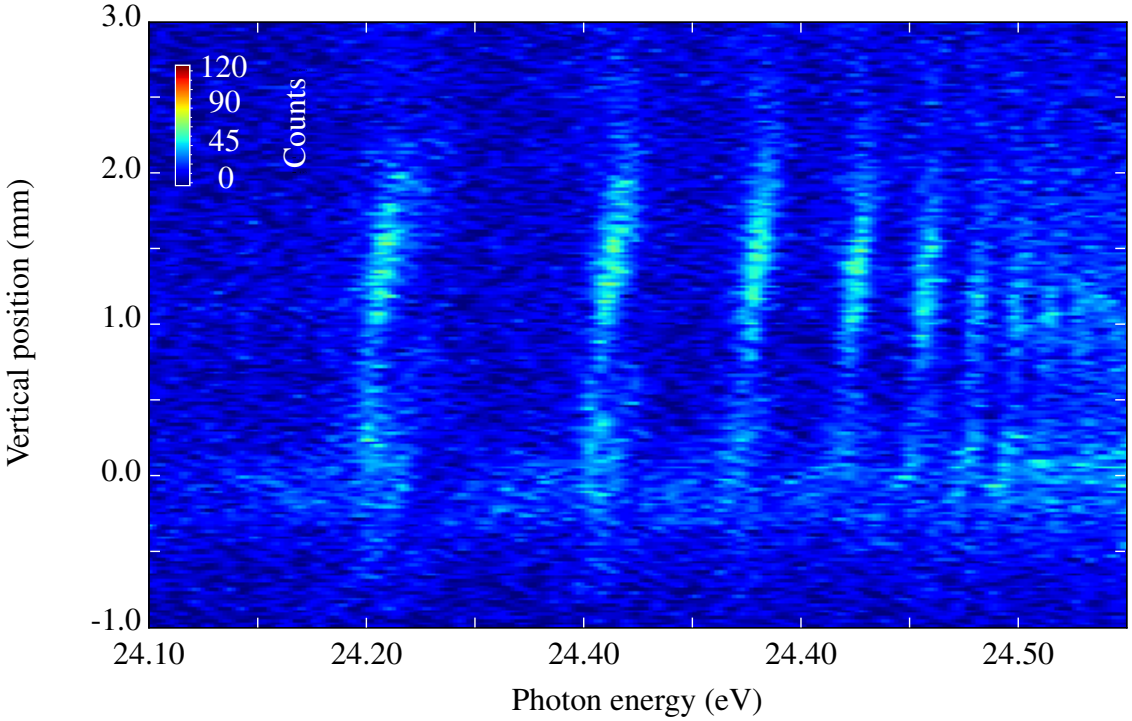

Figure 4.14: Full-chip camera picture. The x-axis is calibrated in energy and the y-axis is calibrated in the spatial dimensions of the camera chip. Similar to Fig. 4.13 the part around 0.0 mm height is the harmonic spectrum of the XUV pulse. The intensity of the VIS laser was set to 4.5 $^{TW}/_{cm^2}$. Clearly visible is the XUV light between 1 mm and 2 mm. The energy position of the emission lines corresponds to the energy position of the absorption lines recorded for the case of no VIS pulse (see Fig.4.13).

4.3.4 Physical Significance of the Phase φ

The phase $\Delta\varphi$ imprinted at the onset of the decay of an exited isolated state not embedded in any continuum states, directly results in a Fano-like absorption profile with asymmetry parameter $q(\Delta\varphi)$ as given by Equ. 4.3. The offset due to the background absorption in the spectral domain, which is given by the δ function in the time domain caused by the non-resonant continuum absorption, is then of course absent. Within the framework of the Fano phase formalism, the laser-induced phase shift $\Delta\varphi$ can thus be interpreted as an angle which determines the mixing between dispersion $[\Re d(\omega)]$ and absorption $[\Im d(\omega)]$. It is controlled by the VIS laser pulse. As a consequence, shifting the dipole response function by a phase $\varphi = \pi$, absorption is transformed into gain (as shown in Fig. 4.10 and also discussed in chapter 4.1.1) and positive dispersion is transformed into negative dispersion.

Using the formalism described above also other effects such as electromagnetically–induced transparency (EIT) [129, 130], lasing without inversion [144], slow and fast light [131], and other related effects, can be interpreted from a time-domain point of view, opening a different perspective.

Beyond the Short-Pulse Limit

Note, that up to now we only discussed the singly excited 1snp states and the $sp_{2,n+}$ states for $n \geq 4$. If the life time of a state is comparable to the pulse duration, neither of the two equations 4.7 and 4.9 applies. The dipole response can be calculated numerically (see [3, 145]). In this intermediate regime, Rabi cycling (see section 2.3) and ionization must be taken into account.

The 2s2p state has a lifetime of a few tens of femtoseconds, thus the condition of a kick-like phase change by the VIS pulse is not fulfilled and the analytic Fano-phase formalism fails to describe the line shape changes. The $sp_{2,3+}$ state exhibits a complicated mixture of the discussed non-resonant (ponderomotive) and resonant coupling via the $2p^2$ to the 2s2p state [3]. The resulting sub-cycle time-delay-dependent shifts of the 1s3p resonance have recently been observed in transient-absorption measurements [134]. This time-dependent dipole phase shifts and amplitude modulations are beyond the applicability of the simple Fano phase formalism, which focuses on a global change of the dipole phase φ at a constant time delay directly after excitation and relates it to the transformation of the Fano q parameter.

Beyond the constant time delay

Nevertheless in the limit of a kick-like VIS pulse after the excitation an analytic description can be found to explain the time dependent case. The derivation of this formula and its application will be presented in the next section.

4.3.5 Time Dependent Fano Phase Formalism

In the previous section the Fano-phase formalism was introduced, mapping the Fano asymmetry parameter q to a phase φ of the time-dependent dipole response function. This formalism was developed for a δ-like excitation and a subsequent "phase kick" by a VIS laser pulse right after the excitation. It is confirmed experimentally as the "phase kick" transforms the Fano absorption lines of the $sp_{2,n+}$ ($n \geq 4$) states in helium into Lorentzian lines. In a semiclassical picture the source for the phase change is the gain of ponderomotive energy by the electron. Alternatively, the phase change is understandable as a dressing of the bound $sp_{2,n+}$ states by the VIS laser. As the $sp_{2,n+}$ ($n \geq 4$) states are less than one VIS photon energy away from the $N = 2$ continuum, the laser-dressed states are embedded in this continuum. Note, that besides the dressing, which is adiabatically switched on and off, the VIS laser pulse has no effect on the system, in particular no population transfer takes place. Therefore, the Fano phase formalism presented in chapter 4.1 is formulated time independently. In contrast to the *non-resonant*, ponderomotive coupling presented in the previous sections, *resonant* coupling of two states transfers population and, thus, leads to transient effects (e.g. coherent superposition [146, 147], wave packets [47, 104, 148], etc.).

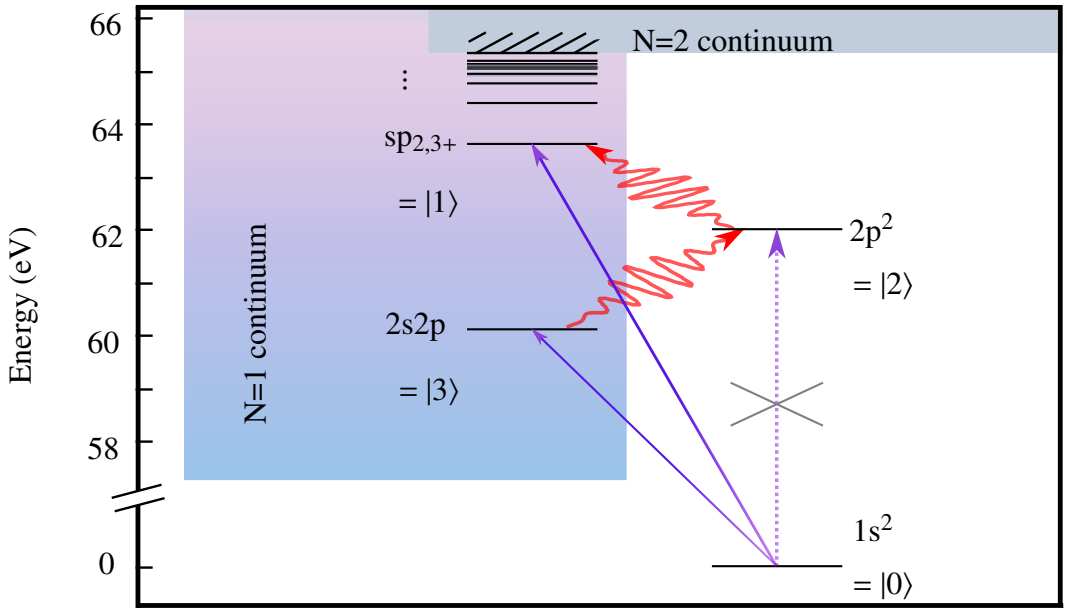

Figure 4.15: Doubly-excited states of helium and the embedded 3-level laser-coupled system. The XUV pulse coherently excites the dipole-allowed 2s2p and $sp_{2,3+}$ states (straight arrows), while the energetically intermediate $2p^2$ state cannot be accessed from the ground state $1s^2$. Both the 2s2p and $sp_{2,3+}$ states are resonantly coupled by two photons of a VIS pulse, via the $2p^2$ state. The VIS laser (photon energy $\hbar\omega_L \approx 1.7\,eV$) resonantly couples the lowest-lying dipole-allowed excited states $sp_{2,3+} = |1\rangle$ and $|2s2p\rangle = |3\rangle$ in a two-photon transition via the energetically intermediate $2p^2 = |2\rangle$ state, after their initial XUV excitation from the $1s^2 = |0\rangle$ ground state.

Resonant light–matter interactions have been intensively studied using long, monochromatic laser fields [130, 149, 150]. In the case of monochromatic light, i.e. electromagnetic fields that are δ-function-like in the spectral domain, it is hard to extract time-dependent information from the system under investigation. With the recent advent of attosecond pulse generation techniques the possibility to observe electronic behavior in the time domain has become feasible, triggering many theoretical predictions [43, 137, 151, 152]. Also, in the experiments presented in this work, we have used extremely short pulses with a large spectral bandwidth described as δ-like in the time domain, allowing for high temporal resolution. In consequence the experimentally obtained results call for a temporal interpretation. Especially, the resonant coupling and its consequences for the dipole response function must now be described in the time domain. The deeper understanding of the phase relations between the exciting field and the induced dipole response as well as the time dependent population transfer is of great interest to the field of atomic and molecular physics. Additionally, in this section the question will be addressed how the current technical inability to directly measure the amplitude and the phase of the XUV light field can be overcome. This section is based on our already published work [1] and will adhere closely to the publication.

In this section we investigate the temporal structure of the transition between the ground state and the $sp_{2,3+}$ state of helium. Using the VIS laser pulse subsequently following the excitation of the doubly excited $sp_{2,n+}$ states, we resonantly couple the $sp_{2,3+}$ and the 2s2p state. To illustrate the coupling between these states, Fig. 4.15 shows a zoom into the

energy region between 58 eV and 66 eV of the helium level scheme presented in Fig. 2.8. If considering solely the 2s2p and $sp_{2,3+}$ states with an energy spacing $\Delta\omega_{1,3} = 3.51\,\text{eV}$, the coupling would need an intense laser beam to achieve the two-photon absorption, as a direct transition is dipole forbidden. It is a fortunate coincidence that the even-parity state $2p^2$ at 62.06 eV couples resonantly to both states within the bandwidth of our laser pulse. Consequently, the coupling between the $sp_{2,3+}$ state, which is called $|1\rangle$ from now on, and the 2s2p state–which we will call $|3\rangle$–is resonantly enhanced by the $2p^2$ state. The $2p^2$ state–which is called $|2\rangle$ in the following–is not accessible via dipole excitation from the ground state $1s^2$ ($|0\rangle$) due to dipole selection rules.

We are now focusing on the time-dependent dipole response $\tilde{d}_{10}(t)$ originating from the superposition of states $|1\rangle$ and $|0\rangle$. Not only phase modifications of $\tilde{d}_{10}(t)$, as discussed in the previous sections. but also amplitude modifications of $\tilde{d}_{10}(t)$ give rise to changes in the spectroscopic line shape. This effect is illustrated in Fig. 4.16, showing the time-dependent atomic dipole moment $\tilde{d}(t)$ after δ-like XUV excitation at time t = 0. As previously mentioned, the duration of the VIS laser pulse is 7 fs while one cycle of the dipole oscillation is around 60 as. Therefore, the oscillation period of $\tilde{d}(t)$ in Fig. 4.16 is enlarged by approximately three orders of magnitude. The exponentially decreasing envelope, due to the fact that the system autoionizes and therefore decays with a lifetime of $\approx 80\,\text{fs}$, is to scale with the depicted VIS pulse duration.

The observed spectral response, or correspondingly the absorption (OD) [see inset of Fig. 4.16], depends not only on the intensity but also on the time delay of the VIS pulse, which resonantly couples the autoionizing states $|1\rangle$ and $|3\rangle$. The time delay between the XUV and the VIS pulse is varied within 10 fs, corresponding to 10% of the lifetime of state $|1\rangle$. The general assumption that the perturbation by the VIS pulse is considered to be instantaneous is therefore still fulfilled.

In chapter 2 we introduced an effective two-level system, which we will now use to understand the few-level coupling in detail for the case of a short laser pulse. Afterwards we extend this model to a multilevel Ξ system. We consider a general two-level model system consisting of two excited states $|1\rangle$ and $|2\rangle$. Their energy spacing in atomic units is denoted by $\Delta\omega_{12} \approx \omega_L$. As they shall be coupled by a single photon transition, we choose the states to have opposite parity. Due to dipole selection rules, only $|1\rangle$ is initially populated at $t = 0$ (by the XUV pulse) while $|2\rangle$ remains empty. After the excitation, the wavefunction $\Psi(t)$ of the system is expressed as the sum of the two populated states:

$$\Psi(t = 0) \propto a_0|0\rangle - \imath a_1|1\rangle. \tag{4.19}$$

The coefficient of the ground state $a_0 \approx 1$ for all times, assuming a weak excitation (as it is the case for the XUV pulse in our experiment). The complex expansion coefficient a_1 can be parametrized as $A_1 e^{\imath\varphi_1}$. The $sp_{2,3+} \hat{=} |1\rangle$ state is embedded in the $N = 1$ continuum, thus exhibiting a phase shift of $\varphi = 0.24\pi$ (see section 4.3.1). Due to this phase shift the spectral dipole response of the $sp_{2,3+}$ state features a Fano line shape. We now associate the phase φ_1 of the coefficient with the phase $\varphi = 0.24\pi$. Consequently, by using the mapping $q_i = -\cot(\varphi_i/2)$ given in Equ. 4.3 the asymmetry parameter q_1 assumes its literature value of −2.58. To describe the interaction with the VIS pulse, near-resonantly coupling the

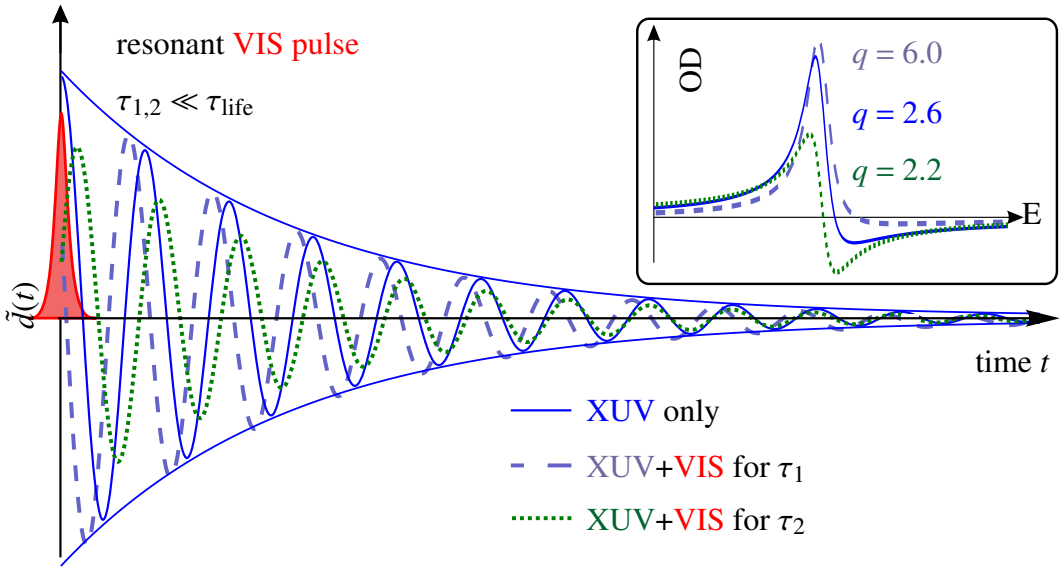

Figure 4.16: The time-dependent atomic dipole moment $\tilde{d}(t)$, after δ-like XUV excitation at time t = 0. The VIS laser pulse (red shading) duration is scaled to the time of the decay of the dipole moment. The oscillation period of the dipole moment is enlarged by three orders of magnitude. The observed spectral response [optical density (OD)], see inset, depends on the intensity and time delay of a VIS pulse, which resonantly couples the autoionizing states $|1\rangle$ and $|3\rangle$. The time delay τ_i is much smaller than the lifetime of the state τ_{life}. Therefore, the interaction with the VIS pulse can still be considered as instantaneous on the time scale of the decay.

states $|1\rangle \hat{=} \text{sp}_{2,3+}$ and $|2\rangle \hat{=} 2\text{p}^2$, we use second-order perturbation theory (see chapter 2.2 and Append. B.5). The dipole transition from 2p^2 state to the ground state is forbidden because of their parity. The lifetime of the 2p^2 state is around 100 ps [153, 154] and therewith much larger than the lifetime of the $\text{sp}_{2,3+}$ state. The life time of the $\text{sp}_{2,3+}$ state, by contrast, is 80 fs [155]. Nevertheless, as the VIS pulse is significantly shorter than the life time of both states, we approximate it by an infinitesimally short interaction, a δ-like pulse. After the coupling of the two states the coefficient a_1 of $|1\rangle$ is changed to

$$a_1' = a_1 + a_{\text{self}}. \tag{4.20}$$

The second term

$$a_{\text{self}} = A_{\text{self}} \cdot \text{e}^{\imath(\varphi_1+\pi)} \propto -a_1 \cdot E_{\text{VIS}}^2 \cdot \left|\mu_{12}\right|^2 \tag{4.21}$$

describes the two-photon laser coupling to state $|2\rangle$ and back to $|1\rangle$, and depends on the square of the coupling electric field strength $\mathcal{E}_{\text{VIS}}$ and the squared absolute value of the dipole-transition matrix element μ_{12} between the states $|1\rangle$ and $|2\rangle$. As the coefficient a_{self} refers to a two-photon process in perturbation theory, it is much smaller than the coefficient a_1. Note that a_{self} is π out of phase with the original excitation a_1, corresponding to a small loss of population from state $|1\rangle$ to $|2\rangle$.

Having the formulas for the two-level coupling at hand, we extend the theory to three levels. Therefore we include the third $|3\rangle$, located energetically below $|2\rangle$ with an energy spacing of $\Delta\omega_{23} \approx \Delta\omega_{12} \approx \omega_{\text{L}}$ (see Fig. 4.15). The VIS laser pulse couples $|3\rangle$ to $|1\rangle$ by a two-photon transition via $|2\rangle$. The excitation at time $t = 0$ coherently excites states $|1\rangle$ and

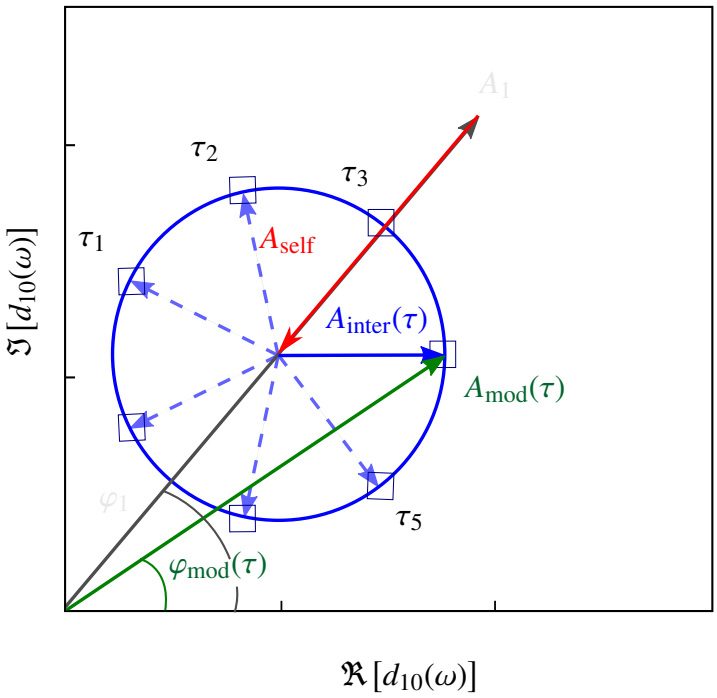

Figure 4.17: Graphical representation of the complex amplitude of an excited state $\hat{=}|1\rangle$, resonantly coupled by δ-like pulsed laser interaction to two other levels: a (dark) initially non-populated intermediate state $\hat{=}|2\rangle$, and a coherently excited (bright) state $\hat{=}|3\rangle$. In second-order perturbation theory, the amplitude contribution for transition in and out of the dark state A_{self} is phase shifted by π with respect to the original excitation amplitude A_1, resulting in an amplitude reduction due to population transfer. The contribution of the coherently-excited bright state A_{inter} describes a circle in the complex plane as a function of time delay due to the energy difference between the states and their corresponding field-free time-dependent phase evolution.

$|3\rangle$. Again, using second-order perturbation theory we find that the expansion coefficient of $|1\rangle$ after the VIS interaction picks up a third term arising from the inter-state coupling, complementing Equ. (4.20) to

$$a'' = a_1 + a_{\text{self}} + a_{\text{inter}}(\tau). \tag{4.22}$$

The third contribution

$$\begin{aligned} a_{\text{inter}}(\tau) &= A_{\text{inter}} \cdot \mathrm{e}^{\imath(\varphi_3+\pi+\Delta\omega_{13}\tau)} \\ &\propto a_3 \cdot E_{\text{VIS}}^2 \cdot \mu_{32}\mu_{21} \cdot \mathrm{e}^{\imath\Delta\omega_{13}\tau} \end{aligned} \tag{4.23}$$

depends on the time delay τ between the XUV excitation and the VIS coupling pulse. The reason for this time-delay dependence is that both coherently excited states $|1\rangle$ and $|3\rangle$ evolve in time with a relative phase, because of their different energies. Consequently, state $|3\rangle$, which is coherently excited with the initial coefficient a_3 by the same XUV pulse as $|1\rangle$, has the relative phase $\Delta\omega_{13}\tau$ compared to state $|1\rangle$.

We now use a'' as the coefficient for state $|1\rangle$ in the wavefunction of this effective 3-level system and calculate the dipole response for the natural decay from the excited state $|1\rangle$ to

the ground state $\tilde{d}_{10}(t)$. The time-dependent dipole response $\tilde{d}_{10}(t)$ lies in the XUV energy regime and is after the VIS interaction given by

$$\tilde{d}_{10}(t) = \langle \Psi(t)|r|\Psi(t)\rangle \propto A_{\text{mod}} e^{\imath\varphi_{\text{mod}}} \cdot e^{-\frac{\Gamma}{2}t + \imath\Delta\omega_{01}t} + c.c. \tag{4.24}$$

with the natural decay rate $\Gamma = 1/\tau_{\text{life}}$ for $t > 0$ and $c.c.$ denoting the complex conjugate of the first term. The complex prefactor $A_{\text{mod}} e^{\imath\varphi_{\text{mod}}}$ is proportional to the expansion coefficient a'', using Eqs. (4.21 and 4.23). As we recall from section 3.4.1, the Fourier transform of $\tilde{d}_{10}(t)$, given by $d_{10}(\omega)$, is proportional to the background-corrected Fano absorption cross section.

$$\sigma_{\text{Fano}}(\omega) - 1 \propto \Im[d_{10}(\omega)] \propto \Im\left[A_{\text{mod}} e^{\imath\varphi_{\text{mod}}} \frac{\imath - \epsilon(\omega)}{1 + \epsilon^2(\omega)}\right] \tag{4.25}$$

with the reduced energy $\epsilon = {}^{2(\omega-\Delta\omega_{01})}/_{\Gamma}$. Due to the linearity of the Fourier transformation, the three contributions to the quantum-state coefficient a'' also contribute additively in the complex factor

$$\begin{aligned} A_{\text{mod}}(\tau) e^{\imath\varphi_{\text{mod}}(\tau)} = {} & A_1 e^{\imath\varphi_1} + A_{\text{self}} e^{\imath(\varphi_1+\pi)} \\ & + A_{\text{inter}} e^{\imath(\varphi_3+\pi+\Delta\omega_{13}\tau)}, \end{aligned} \tag{4.26}$$

which governs the line shape of the measured absorption spectrum (see Equ. 4.25). Since $A_{\text{mod}}(\tau)$ depends explicitely on the time delay τ between the XUV and the VIS pulse, the absorption spectrum $\sigma(\omega)$ also varies as a function of τ.

The individual contributions and the total sum to the complex dipole response are represented graphically by a phasor addition in the complex plane (see Fig. 4.17). While the first two contributions in Equ. 4.26 are π out of phase relative to each other and independent of τ, the third contribution is fixed in amplitude A_{inter} but varies in phase $\varphi_{\text{inter}}(\tau)$. This causes the phasor sum to circle around a fixed center point in the complex plane as the time delay is varied.

4.4 Application of the Generalized Fano Phase Formalism

In the last section we developed a model to describe the time-delay dependent changes in the Fano line shape by interaction with the VIS pulse. This model allows to extract dynamical modifications of the amplitude and phase of the near-resonantly coupled doubly-excited states in helium. We therefore apply the model to measured absorption spectra across the $sp_{2,3+}$ state in helium for different time delays and intensities of the VIS coupling pulse.

For high VIS peak intensities, it has been found [135] that additional effects change the line profiles and their respective energy position (e.g. AC Stark shifts). Also the line width

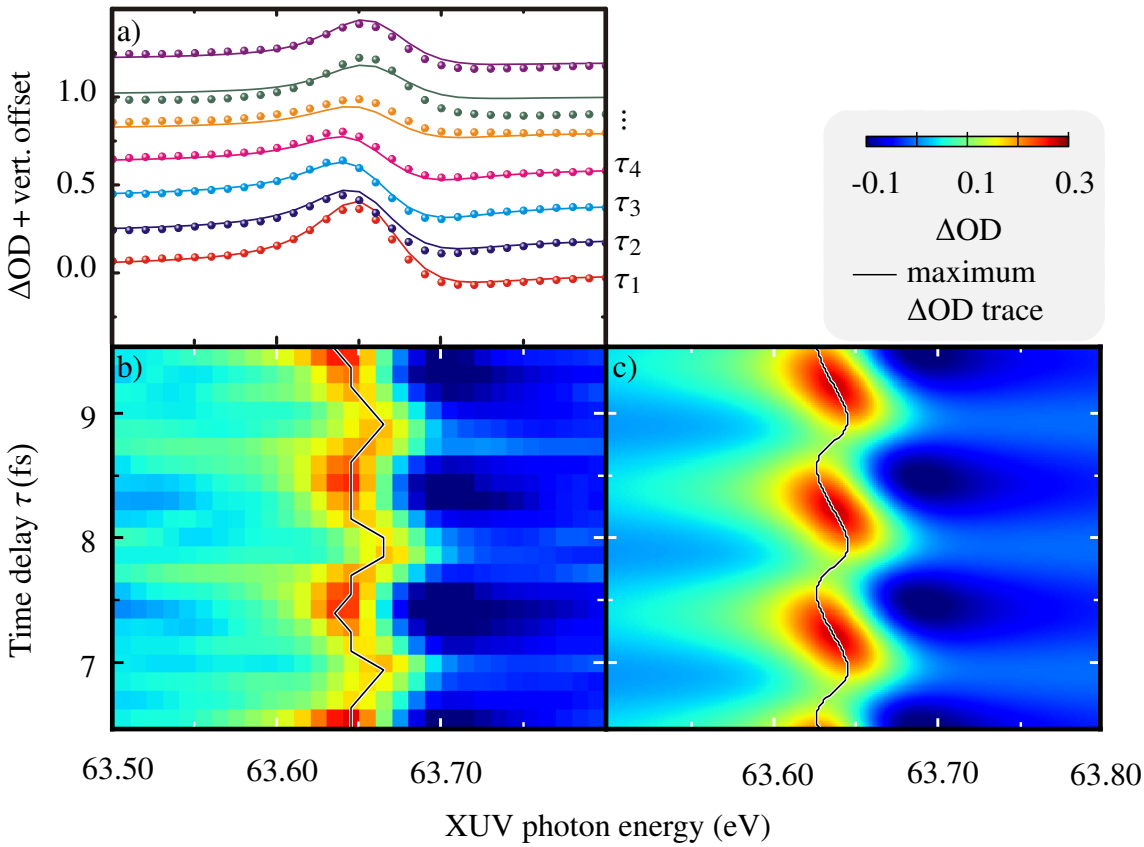

Figure 4.18: a) Measured (dots) Fano resonance absorption spectrum [optical density (OD)] near the He $1s^2 \rightarrow sp_{2,3+}$ transition. The resonant line shape changes with time delay τ from 8.6 fs to 9.8 fs of the VIS pulse following the XUV excitation. The VIS intensity was set to 0.5×10^{12} W/cm^2. Analytical formula [Eqs. (4.25-4.26)] (solid lines) for a fixed resonance-energy position. b) Measured absorption spectra for varying time delay. c) Analytically calculated absorption spectra [Eqs. (4.25-4.26)] after convolution with the spectrometer resolution (20 meV). The maxima of each of the spectra are also highlighted by the black solid oscillatory trace. The oscillation of the maxima is due to a line-shape change while the resonance energy remains constant.

of the states can be affected, as the intensity of the long-lasting pedestal also increases. To rule out these additional effects we go to intensities below 1.4 TW/cm^2. As the laser-induced phase depends on the peak intensity, also the maximal value for the phase shift $\Delta\varphi$ is reduced. Still it is possible to trace the half laser cycle periodicity of the line shape changes, as presented in Fig. 4.18 a) and b) (dots represent the measured data), which show a zoom near the $sp_{2,3+}$ state of a set of time–delay-dependent absorption spectra. Fig. 4.18 b) shows the absorption spectrum over a time-delay range of 4 fs. It is the same data set as Fig. 4.6, where the VIS intensity was set to 0.5×10^{12} W/cm^2. This spectrum is modified with a period corresponding to approximately half the optical cycle of the VIS pulse. Interestingly, a small shift of as a function of τ is observed, as indicated by the black solid oscillating trace connecting the maxima of each spectrum. The shift of the absorption maximum is due to the modifications of the line-shape asymmetry, as the line

outs in Fig. 4.18 a) show. This is explained by a "phase kick" of the dipole response by the VIS laser pulse, as discussed in the time-dependent Fano phase mechanism presented in the previous chapter. As a result of the "phase kick", the spectral position of the absorption maximum varies as the line shape changes from an asymmetric, Fano-like profile to a more symmetric, close-to-Lorentzian profile, while the resonance energy and width remain constant. From an entirely different perspective, the experimental results and their interpretation are also of general importance for the budding field of attosecond transient absorption spectroscopy [109, 156–158]. In the absence of line-shape information at high spectral resolution, such a shift could be confused with a time-dependent energy-level shift, creating an important caveat for transient-absorption spectroscopy.

In the next step we use the understanding of the time-dependent Fano phase mechanism and the resonant coupling therein to extract the time-dependent relative phases. If we insert the experimental parameters (e.g. VIS pulse intensity, time-delay, etc.) and the literature values for the 2s2p, the $2p^2$ and the $sp_{2,3+}$ state (i.e. energy position, q_{orig}, Γ) in the model described in the previous section, we obtain the spectra presented in Fig. 4.18 c).

Both, the experimental data set in Fig. 4.18 b) and the theoretical data set in Fig. 4.18 c) show the same overall behavior. The maxima shift with the same frequency. Nevertheless in the theoretical data, the slope for the shift from high energies to low energies is smaller than for the opposite direction. In the experimental data, despite the lower resolution, we can state, that this behavior is not observed. To check the agreement between the theoretical predicted and measured line shapes, the line outs, corresponding to the measured data (dots), are additionally plotted in Fig. 4.18 a) as solid lines. For certain time-delays, both curves do not agree very well, while for others the agreement is almost perfect.

As the model, fed by the experimental parameters and literature values, can not explain the differences between the theoretical to the experimental line shapes present for some time-delays [see 4.18 a)], we now take a second approach to determine the experimentally measured time-delay dependent amplitude and phase changes. Therefore, a sequence of absorption line shapes to the state $sp_{2,3+}=|1\rangle$ is fitted using the background–absorption-free Fano cross section in phase representation (see Equ. 4.25)

$$\sigma_{\mathrm{Fano}}(\omega) \propto \Im\left[A_{\mathrm{mod}} e^{\imath\varphi_{\mathrm{mod}}} \frac{\imath - \epsilon(\omega)}{1+\epsilon^2(\omega)}\right] \tag{4.27}$$

For this fit, the amplitude A_{mod} and phase φ_{mod} were left as free parameters (see Fig. 4.17), while μ_{12}, μ_{23}, μ_{13}, Γ_i, ω_i ($i \in [1,2,3]$) were fixed to tabulated values [159]. We, thus, assign an amplitude and a phase value to each given time delay and laser intensity.

In Fig. 4.19 $A_{\mathrm{mod}} e^{\imath\varphi_{\mathrm{mod}}}$ is plotted in the complex plane for half a VIS laser cycle. Half a VIS cycle is scanned by seven time-delay steps, the eighth step is then the same as step one. To prove that this is the case for the fit, eight complex coefficients, subsequent in time-delay are plotted for every intensity. The direction of rotation for the complex A_{inter} is indicated by the grey solid arrow, spanning over the first three complex coefficients (sorted by time-delay). Interestingly, we observe an elliptical shape of the curve rather

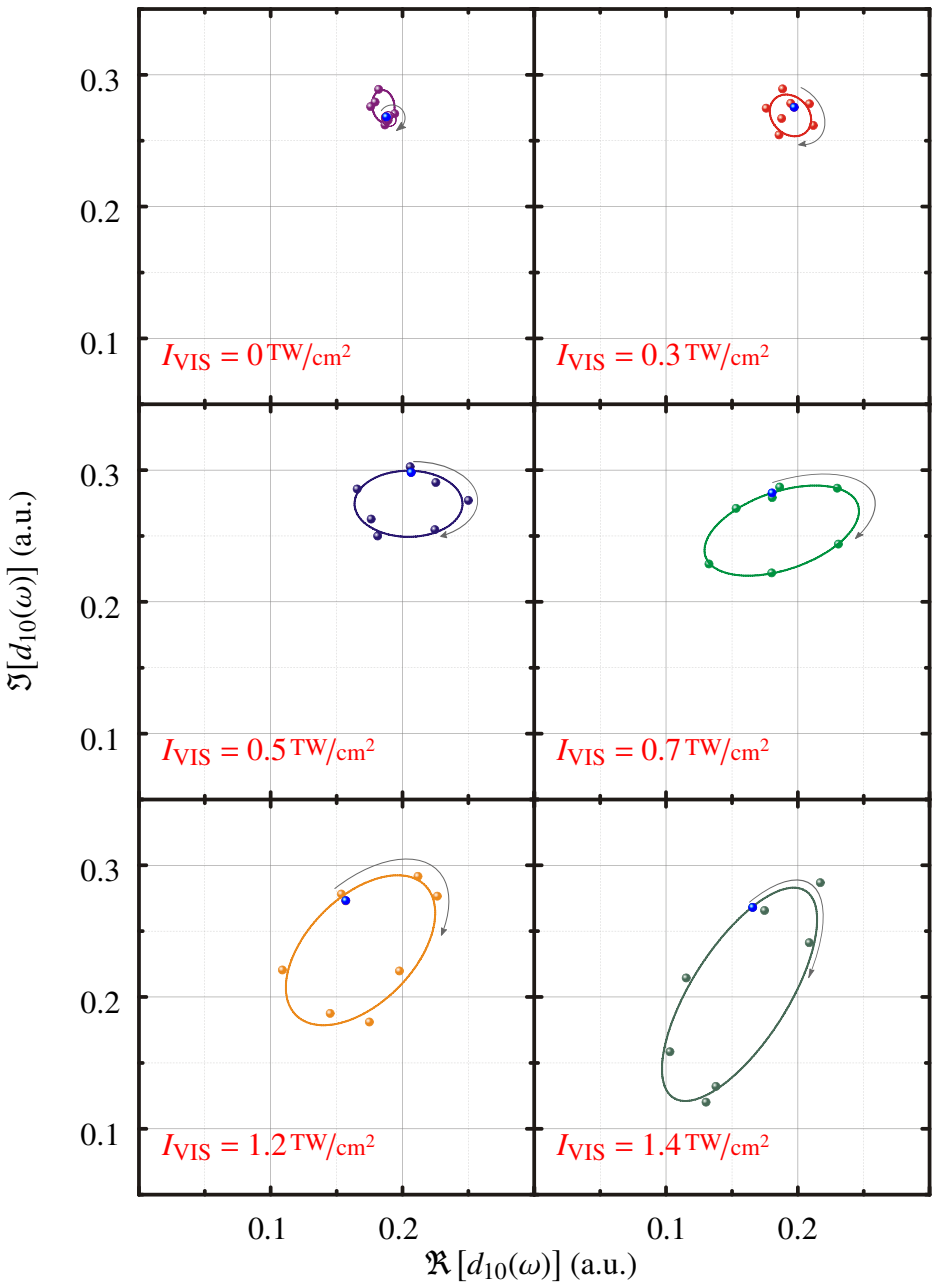

Figure 4.19: Spectral dipole amplitudes and phases as a function of the VIS intensity and time delay. Each subplot represents a complex plane in which the time-delay evolution of the dipole moment is shown. The dots show the experimental data, the solid lines are ellipsoidal fits. One half cycle of the VIS pulse corresponds to 7 data points. The eighth data point is plotted to show that the ellipse starts again after one VIS half-cycle. The first data point of each plot is highlighted in blue, the order of the subsequent time-delay dependent complex values is indicated by the grey arrow (clockwise for increasing time delay). The time delay τ ranges from 9.8 fs to 11.0 fs. By extracting the circle radius and center as a function of VIS intensity, the different resonant coupling pathways can be separated [as shown in Fig. 4.20a) and b)]. With increasing intensity and correspondingly larger radius approaching the size of the initial amplitude, the circles become more and more elliptical.

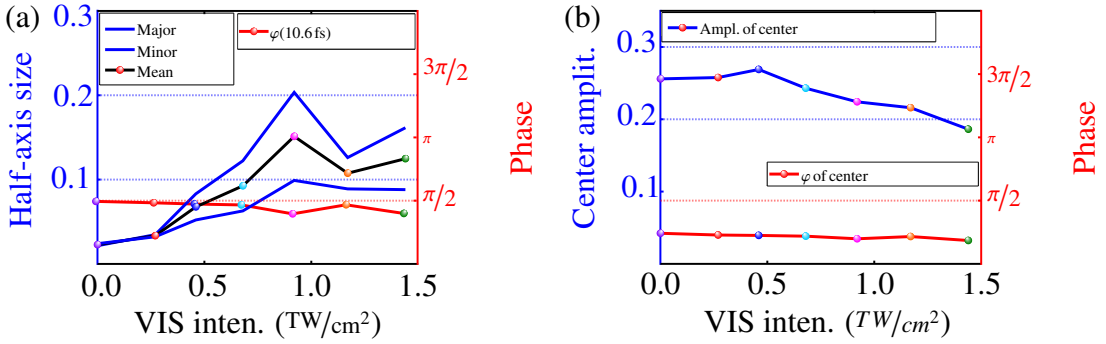

Figure 4.20: a) Length of the semi-major and semi-minor axis of each ellipse (blue curves and left vertical axis), the corresponding mean value (black curve and left vertical axis) and the phase of the point (red curve and right vertical axis) at fixed time delay 10.6 fs , relative to the center point, for each measured VIS intensity. b) The absolute value of the complex-valued center point of each ellipse (blue curve and left vertical axis) and the corresponding phase (red curve and right vertical axis) for each measured VIS intensity. The center point of the ellipse changes its position due to population transfer with increasing VIS intensity. The phase of the center point remains approximately constant for all VIS intensities.

than the circle that was intuitively expected from our model. The elliptical shapes change with increasing VIS pulse intensity I_{VIS}. To quantify this change we fit the ellipses using a fit algorithm adapted from the one developed by Gabriel Taubin [160][8]. With this algorithm it is possible to fit an ellipse using 6 sampling points. After finding the ellipse with the least mean square error we extract the center point, the length of the ellipses semi-major axis l_{maj} and the length of its semi-minor axis l_{min}.

Comparing the fitted ellipses in Fig. 4.19, we observe, that the eccentricity

$$c_{ecc} = \frac{\sqrt{l_{\mathrm{maj}}^2 - l_{\mathrm{min}}^2}}{l_{\mathrm{maj}}} \in [0, 1) \tag{4.28}$$

approaches the limit of 1 for increasing intensities, while a circle exhibits an eccentricity $c_{ecc} = 0$.

In addition to the fact that the eccentricity increases as a function of the VIS intensity, the center point of the ellipse moves closer to the origin [see Fig. 4.20 a)] as expected from population transfer expressed by the contribution a_{self}. We can interpret the elliptical shape as the superposition of two counter-rotating contributions to the complex coefficient in the observed state $|1\rangle$. A second laser-coupled state energetically above $|1\rangle$, coherently excited by the XUV pulse, would add this counter-rotating contribution by the same reasoning as given above for the lower-lying $|3\rangle$ state. In fact, the $N = 2$ continuum in helium (see Fig. 4.15) can contribute by a two-photon transition into state $|1\rangle$, providing such a counter-rotating term.

From the second-order perturbative two-photon inter-state population transfer (as discussed for the circle above, see Fig. 4.17 and Equ. 4.23) an increase of the ellipse half-

[8]This algorithm is among the most accurate non-iterative ellipse fit algorithms, only surpassed by a recently published algorithm [161], which requires more sampling points.

axis size is expected with increasing VIS intensity. This tendency is confirmed for the measured ellipse (semi-major and semi-minor) axes [Fig. 4.20b)].

Chapter 5

Conclusion

In this work, we investigate the behavior of the coupling dynamics of autoionizing states by perturbed polarization decay and therefore combine a few milli-electronvolt spectral resolution and an attosecond temporal resolution. We laser-control the absorption of the states on a sub–laser-cycle timescale and, by phase-resolved interferometry, retrieve the involved different few-photon quantum pathways using laser pulses at controlled time delay and intensity. We developed a Fano-phase mechanism describing the correspondence between the dipole-response phase φ and the line-shape asymmetry q and introduced the concept of a "phase kick", an abrupt change in the dipole emission phase induced by the short-pulsed laser via *non-resonant* ponderomotive coupling on the onset of the dipole's decay. Moreover, we generalized the model of the Fano-phase mechanism to the measurement of time-dependent phases and amplitudes induced by short-pulsed *resonant* laser coupling.

For the Fano-phase approach we interpret the absorption line shapes of spectroscopic measurements in the time-domain picture as the interference between the transmitted (XUV) light and the light emitted by the decay of the induced polarization. Thus, the relative phase information is also encoded in spectral line shapes. For this temporal interpretation, we derived the mapping between the q parameter and the relative phase between the two interfering light fields to

$$\varphi(q) = 2\arg(q - \imath) \Leftrightarrow q(\varphi) = -\cot(\varphi/2)\,. \tag{5.1}$$

We highlighted the important implication of this mapping (Equ. 5.1) that any phenomenon shifting the dipole response of a system out of phase with an initial excitation can be used to modify the q parameter.

To experimentally prove the concept we use XUV light passing through a helium gas target to populate the singly excited 1snp states (with bound–bound transitions only) and the doubly excited $\mathrm{sp}_{2,n+}$ states embedded in the $N = 1$ continuum (with both bound–bound and bound–continuum transitions) and control their absorption profiles by a subsequent short-pulsed VIS laser. By setting a fixed time-delay and controlling the intensity,

we show how an asymmetric Fano line shape is turned into a symmetric Lorentzian one and *vice versa* (Fig. 5.1). We show that it is even possible to turn an original absorption of light into an emission line.

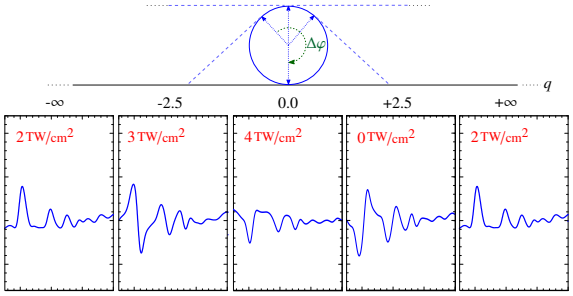

Figure 5.1: Illustration of the laser-induced "phase kick" $\Delta\varphi$ and the mapping on q as well as the experimental proof by the corresponding measured line shapes. Full picture on page 63.

Identifying the intensity-dependent *non-resonant* ponderomotive shift by the VIS laser pulse as a source for a change in the phase φ, we experimentally confirmed the Fano-phase approach.

In addition, we expanded the Fano-phase formalism to the *resonant* coupling of two states. This model was confirmed for the example of doubly-excited states in helium resonantly coupled by a two VIS-photon transition. In this measurement, we turned an asymmetric Fano line shape into a symmetric Lorentzian one within a quarter of the VIS period (≈500 attoseconds). Population can be transferred for the resonant-coupling case, depending on the time delay between the exciting XUV and the VIS pulse altering the spectral amplitude and phase of the light compared to the light from the unperturbed decay. Using the generalized model of the Fano-phase formalism, we extracted the amplitude modifications A_{mod} and phase modifications φ_{mod} by the VIS laser and thereby achieved the separation of different few-photon quantum pathways (Fig. 5.2) that are involved in the coupling dynamics of the autoionizing states.

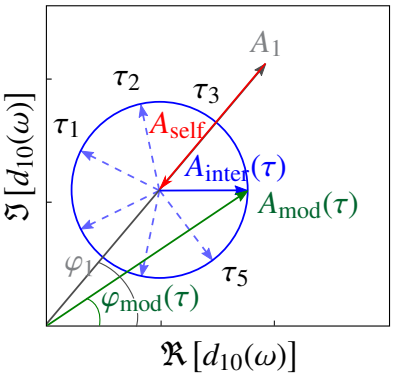

Figure 5.2: Illustration of the separation of different pathways. Full picture on page 73.

Higher-precision measurements and the analysis of the exact variation of the different phase contributions with laser control will help to better understand the laser coupling of autoionizing states to other bound or continuum states. Resonant electronic processes have recently been considered in a theoretical treatment [151]. The authors considered a single XUV pulse coherently exciting the $\mathrm{sp}_{2,n+}$ series in helium. They found the autoionized electrons appearing periodically in the continuum as bursts separated by ≈ 1.2 fs. The energy level spacing between the states 2s2p and $\mathrm{sp}_{2,3+}$ $\Delta\omega_{1,3} = 3.51\,\mathrm{eV}$ corresponds to ≈ 1.2 fs. In that publication the authors propose the possibility to observe this beating in time by measuring the yield of excited ($N = 2$) ions with a time-delayed VIS pulse similar to the one used in our absorption measurement. In a future upgrade, the setup used in this work could be adapted to also measure ions and electrons and show this control over the suppression of autoionization.

The understanding of the connection between the line-shape asymmetry and the phase of dipole response (Equ. 5.1) can be applied to laser coupling of states, but can also be used to quantify interactions of any nature. This leads to a deeper understanding of light-matter interaction, especially when the coupling mechanisms are more complex

than just a ponderomotive coupling which is considered here to introduce the principle. There is no reason why the mechanism should not be applicable to molecules, or excitons in condensed phase or mesoscopic materials. This understanding yields answers to the question to what extent absorption could be controlled, in particular regarding effects such as electromagnetically-induced transparency [129, 162] and lasing without inversion[1] [144, 163], which can be explained as phase shifts of the light field.

In addition, the general Fano phase mechanism does not depend on the actual transition frequency, but only on the assumption that the "phase kick" is applied right at the onset of the decay. Consequently, it could be applied to hard-x-ray or even γ-ray transitions with much longer life times. One example would be the well-known Mössbauer transition in ^{57}Fe with a lifetime $> 100\,$ns. For such extremely slow decays, the inversion of the absorption line into an emission line by a phase flip could also be achieved for example by the physical displacement of a solid-state absorber [164] or a nanosecond-pulsed magnetic field, using the Zeeman shift. The δ-like excitation could be realized by a short-pulsed free-electron laser or a sub-nanosecond synchrotron pulse. With this development, frequency standards in the hard x-ray regime can be defined and pulse shaping in the hard x-ray regime is within reach. Moreover, as we already saw signs of lasing without inversion in the XUV, an effective x-ray laser could be realized, as it was originally proposed for a helium-positronium mixture by Dietrich Marcuse [165].

[1] Lasing without inversion was originally proposed for a helium system.

Appendix A

Atomic units

Atomic units are used in this thesis. In the following, the most important physical constants in atomic units are presented, adapted from [128]. In the definition of the atomic units, the reduced Planck constant $\hbar$, the electron mass m_e, the elementary charge e, and the Coulomb constant $(4\pi\epsilon_0)^{-1}$ of the electric force are all set to unity ($\hbar = m_e = e = (4\pi\epsilon_0)^{-1} = 1$). Using this definition, e.g. the energy and frequency of a photon are related via $E = \omega$, or the energy and momentum of an electron are connected via $E = p^2/2$. A list of conversion factors (for the most important physical constants used in this work) between atomic units and the international system of units (SI) is given in the table below. The atomic unit of intensity is proportional to the square of the atomic unit of the electric

Table A.1: Physical quantities expressed in atomic units, with data taken from [17] which was updated in 2010.

1 atomic unit of	SI value
energy	$(27.211\,385\,05 \pm 0.000\,000\,60)$ eV
time	$(24.188\,843\,265\,02 \pm 0.000\,000\,000\,12) \cdot 10^{-18}$ s
length	$(0.529\,177\,210\,92 \pm 0.000\,000\,000\,17)$ Å
electric field strength	$(5.142\,206\,52 \pm 0.000\,000\,11) \cdot 10^{9}$ V/cm
intensity	$(3.509\,445\,21 \pm 0.000\,000\,15) \cdot 10^{16}$ W/cm^2

field strength: $I_{\text{a.u.}} = 1/2 \cdot c \cdot \mathcal{E}^2_{\text{a.u.}}$. The used definition allows for an easy conversion between atomic units of the electric field strength and SI units of the laser intensity which is used in the experiment. For example $\mathcal{E} = 0.01$ a.u. then translates to $I = 3.509\,\text{TW/cm}^2$. The speed of light in atomic units is just the inverse of the fine structure constant $c = \alpha^{-1}$, where

$$\alpha^{-1} = 137.035999074 \pm 0.000000044.$$

Appendix B

Time-Dependent Perturbation Theory of the Dipole Response

B.1 A Simple Picture of the Dipole Response

An decaying dipole is mathematically described by the (complex) amplitude A and two exponential functions.

$$d(t) \propto A \cdot \mathrm{e}^{-\Gamma/2t} \cdot \mathrm{e}^{\imath\omega_D t}\Theta(t) \tag{B.1}$$

The decay rate Γ is inversely proportional to the expectation value of the lifetime $\tau = \langle t \rangle$. By using Fourier transformation one can calculate the spectral response of the dipole.

$$\widetilde{d}(\omega) \propto {}^1\!/_{2\pi} \int \mathrm{e}^{-\Gamma/2t} \cdot \mathrm{e}^{\imath(\omega_D-\omega)t}\Theta(t)dt \tag{B.2}$$

$$= \frac{-1}{2\pi\left(\Gamma/2 + \imath(\omega - \omega_D)\right)} \tag{B.3}$$

B.2 Time-Dependent Dipole Response in Beer-Lambert's Law

Absorption in a medium is described by the ratio of the intensity of transmitted light I_T to incident light I_0 [166–168]. The intensity of the transmitted light decreases exponentially with the density of the medium, the traveled distance inside the medium and the frequency-dependent cross section. In equation B.5 we apply the dipole approximation.

$$I_\mathrm{T} = I_0 \cdot \mathrm{e}^{-\sigma(\omega)\rho l} \tag{B.4}$$

$$
\begin{aligned}
I_0 \cdot \mathrm{e}^{-\sigma(\omega)\rho l} &= \left(\frac{E(t) \cdot \cos\left(\omega t + \Re[k]x\right) e^{-\Im[k]l)}}{2\sqrt{\mu_0/\epsilon_r}} \right)^2 \\
&= \left(\frac{E(t) \cdot \cos\left(\omega t + \Re[k]l\right)}{2\sqrt{\mu_0/\epsilon_r}} \right)^2 \mathrm{e}^{-2\Im[k]l} \\
\Leftrightarrow e^{-\sigma(\omega)\rho l} &= \mathrm{e}^{-2\Im[k]l} \\
\Leftrightarrow \sigma(\omega)\rho &= 2\Im\left[k\right] \\
\Leftrightarrow \sigma(\omega)\rho &= 2\Im\left[\frac{\omega}{c} n(\omega)\right] = 2\Im\left[\frac{\omega}{c}\sqrt{\epsilon_r(\omega)}\right] = 2\Im\left[\frac{\omega}{c}\sqrt{1+\chi_e(\omega)}\right] \\
&= 2\Im\left[\frac{\omega}{c}\left(\sqrt{1+\Re[\chi_e(\omega)]} + \frac{\imath\Im[\chi_e(\omega)]}{2\sqrt{1+\Re[\chi_e(\omega)]}} + O(\Im[\chi_e]^2)\right)\right] \\
&= 2\Im\left[\frac{\omega}{c}\left(\sqrt{1+\Re[\chi_e(\omega)]} + \frac{\imath\Im[\chi_e(\omega)]}{2}\left(1 - \frac{\Re[\chi_e(\omega)]}{2} + O(\Re[\chi_e]^2)\right)\right.\right. \\
&\qquad \left.\left. + O(\Im[\chi_e]^2)\right)\right] \\
&= 2\Im\left[\frac{\omega}{c}\left(\sqrt{1+\Re[\chi_e(\omega)]} + \frac{\imath\Im[\chi_e(\omega)]}{2} + O(\Re[\chi_e]\Im[\chi_e]) + O(\Re[\chi_e]^2)\right.\right. \\
&\qquad \left.\left. + O(\Im[\chi_e]^2)\right)\right] \\
&\approx 2\Im\left[\frac{\omega}{c}\left(\sqrt{1+\Re[\chi_e(\omega)]} + \frac{\imath\Im[\chi_e(\omega)]}{2}\right)\right] \\
&= \frac{\omega}{c}\Im[\chi_e(\omega)] = \frac{\omega}{c}\Im\left[\frac{\rho\langle d(\omega)\rangle}{\epsilon_0 E(\omega)}\right] = \frac{\rho\omega}{\epsilon_0 c}\Im\left[\frac{\mathscr{F}\left[\left\langle \tilde{d}(t)\right\rangle\right]}{\mathscr{F}\left[\tilde{E}(t)\right]}\right]
\end{aligned}
\tag{B.5}
$$

Here the dipole approximation is used to cut the Taylor expansion after the first term and express the electric susceptibility as $\chi_e(\omega) = \frac{\rho\langle d(\omega)\rangle}{\epsilon_0 E(\omega)}$, where $\langle d(\omega)\rangle$ is the expectation value for the dipole moment, ϵ_0 the electric permittivity of free space, ρ is the inverse unit volume and $E(\omega)$ the electric field. The dipole approximation is justified since the typical photon energies in our experiment are in the order of 10 eV to 100 eV. Hence, a typical wave vector of the photon is $\left|\vec{k}\right| = 1/\lambda = \omega/2\pi c \approx 10^{-3}\frac{1}{\text{Å}}$ while the typical length scale for the electronic state $\left|\vec{r}\right| \approx 1\,\text{Å}$. Therefore the exponential factor in the vector potential can be Taylor expanded as $\exp\left[-\imath\vec{k}\cdot\vec{r}\right] = 1 - \imath\vec{k}\cdot\vec{r} + O((\vec{k}\cdot\vec{r})^2)$ The first term in the expression produces results that are equivalent to the radiation from an oscillating classical electric dipole. The dipole approximation restricts considerations to the case of vanishing orbital angular momenta $\Delta l = 0$. This follows from the assumption that the typical length scale for the electronic state is negligible compared with the scale over which the vector potential varies. Then the vector potential around the atom only describes photons with zero external angular momentum.

$$\Leftrightarrow \sigma(\omega) = \frac{\omega}{c\epsilon_0}\Im\left[\frac{\mathscr{F}[\langle\psi(t)|(-er)|\psi(t)\rangle]}{\mathscr{F}\left[\tilde{E}(t)\right]}\right] \tag{B.6}$$

$$\begin{aligned}
&= \frac{\omega}{c\epsilon_0}\Im\Bigg[\frac{1}{\mathscr{F}\left[\tilde{E}(t)\right]}\mathscr{F}\Bigg[\Big(c_0^*(t)\mathrm{e}^{\imath\omega_0 t}\langle\varphi_0| + c_1^*(t)\mathrm{e}^{\imath\omega_1 t}\langle\varphi_1| + c_2^*(t)\mathrm{e}^{\imath\omega_2 t}\langle\varphi_2| \\
&\qquad + c_3^*(t)\mathrm{e}^{\imath\omega_3 t}\langle\varphi_3|\Big)\Big(-er\Big)\Big(c_0(t)\mathrm{e}^{-\imath\omega_0 t}|\varphi_0\rangle + c_1(t)\mathrm{e}^{-\imath\omega_1 t}|\varphi_1\rangle \\
&\qquad + c_2(t)\mathrm{e}^{-\imath\omega_2 t}|\varphi_2\rangle + c_3(t)\mathrm{e}^{-\imath\omega_3 t}|\varphi_3\rangle\Big)\Bigg]\Bigg] \\
&= \frac{\omega}{c\epsilon_0}\Im\Bigg[\frac{1}{\mathscr{F}\left[\tilde{E}(t)\right]}\mathscr{F}\Bigg[2\Re\Big[c_0^*(t)c_1(t)\mathrm{e}^{\imath(\omega_0-\omega_1)t}\langle\varphi_0|(-er)|\varphi_1\rangle \\
&\qquad + c_0^*(t)c_3(t)\mathrm{e}^{\imath(\omega_0-\omega_3)t}\langle\varphi_0|(-er)|\varphi_3\rangle \\
&\qquad + c_2^*(t)c_1(t)\mathrm{e}^{\imath(\omega_2-\omega_1)t}\langle\varphi_2|(-er)|\varphi_1\rangle \\
&\qquad + c_2^*(t)c_3(t)\mathrm{e}^{\imath(\omega_2-\omega_3)t}\langle\varphi_2|(-er)|\varphi_3\rangle\Big]\Bigg]\Bigg] \\
&= \frac{\omega}{c\epsilon_0}\Im\Bigg[\frac{1}{\mathscr{F}\left[\tilde{E}(t)\right]}\mathscr{F}\Bigg[2\Re\Big[c_0^*(t)c_1(t)\mathrm{e}^{\imath(\omega_0-\omega_1)t}\mu_{01} + c_0^*(t)c_3(t)\mathrm{e}^{\imath(\omega_0-\omega_3)t}\mu_{03} \\
&\qquad + c_2^*(t)c_1(t)\mathrm{e}^{\imath(\omega_2-\omega_1)t}\mu_{21} + c_2^*(t)c_3(t)\mathrm{e}^{\imath(\omega_2-\omega_3)t}\mu_{23}\Big]\Bigg]\Bigg]
\end{aligned} \tag{B.7}$$

B.3 Time-Dependent Perturbation Theory

We now apply Schrödingers equation and the dipole approximation to determine the coefficients $c_i(t)$.

$$\mathcal{H} = \mathcal{H}_0 + \mathcal{H}_I = \mathcal{H}_0 - e\mathcal{E}_{\text{Laser}}(t)r \tag{B.8}$$

$$|\psi\rangle = c_0(t)\mathrm{e}^{-\imath\omega_0 t}|\varphi_0\rangle + c_1(t)\mathrm{e}^{-\imath\omega_1 t}|\varphi_1\rangle + c_2(t)\mathrm{e}^{-\imath\omega_2 t}|\varphi_2\rangle + c_3(t)\mathrm{e}^{-\imath\omega_3 t}|\varphi_3\rangle \tag{B.9}$$

$$\imath\hbar\partial_t|\psi\rangle = (\mathcal{H}_0 + \mathcal{H}_I)|\psi\rangle \tag{B.10}$$

$$
\begin{aligned}
c_0^*(t)\,\mathrm{e}^{\imath\omega_0 t}\langle\varphi_0|\imath\hbar\partial_{t'}|\psi\rangle &= c_0^*(t)\,\mathrm{e}^{\imath\omega_0 t}\langle\varphi_0|\,(\mathcal{H}_0+\mathcal{H}_I)\Big(c_0(t')\mathrm{e}^{-\imath\omega_0 t'}|\varphi_0\rangle \\
&\quad +c_1(t')\mathrm{e}^{-\imath\omega_1 t'}|\varphi_1\rangle + c_2(t')\mathrm{e}^{-\imath\omega_2 t'}|\varphi_2\rangle + c_3(t')\mathrm{e}^{-\imath\omega_3 t'}|\varphi_3\rangle\Big) \\
\imath\hbar\langle\varphi_0|\partial_{t'}|\psi\rangle &= \mathcal{E}_0 c_0(t')e^{-\imath\omega_0 t'}\langle\varphi_0|\varphi_0\rangle \\
&\quad +\mathcal{E}_{\mathrm{Laser}}(t')c_0(t')\mathrm{e}^{-\imath\omega_0 t'}\langle\varphi_0|(-er)|\varphi_0\rangle \\
&\quad +\mathcal{E}_{\mathrm{Laser}}(t')c_1(t')\mathrm{e}^{-\imath\omega_1 t'}\langle\varphi_0|(-er)|\varphi_1\rangle \\
&\quad +\mathcal{E}_{\mathrm{Laser}}(t')c_2(t')\mathrm{e}^{-\imath\omega_2 t'}\langle\varphi_0|(-er)|\varphi_2\rangle \\
&\quad +\mathcal{E}_{\mathrm{Laser}}(t')c_3(t')\mathrm{e}^{-\imath\omega_3 t'}\langle\varphi_0|(-er)|\varphi_3\rangle \\
\partial_{t'}\langle\varphi_0|\psi\rangle &= -\imath/\hbar\Big(\mathcal{E}_0 c_0(t')\mathrm{e}^{-\imath\omega_0 t'} \;+\mathcal{E}_{\mathrm{Laser}}(t')c_1(t')\mathrm{e}^{-\imath\omega_1 t'}\mu_{01} \\
&\qquad +\mathcal{E}_{\mathrm{Laser}}(t')c_2(t')\mathrm{e}^{-\imath\omega_2 t'}\underbrace{\mu_{02}}_{\equiv 0} \\
&\qquad +\mathcal{E}_{\mathrm{Laser}}(t')c_3(t')\mathrm{e}^{-\imath\omega_3 t'}\mu_{03}\Big) \\
\frac{\partial}{\partial t'}c_0(t')\mathrm{e}^{-\imath\omega_0 t'}\langle\varphi_0|\varphi_0\rangle &= -\imath/\hbar\Big(\mathcal{E}_0 c_0(t')\mathrm{e}^{-\imath\omega_0 t'} \;+\mathcal{E}_{\mathrm{Laser}}(t')c_1(t')\mathrm{e}^{-\imath\omega_1 t'}\mu_{01} \\
&\qquad +\mathcal{E}_{\mathrm{Laser}}(t')c_3(t')\mathrm{e}^{-\imath\omega_3 t'}\mu_{03}\Big) \\
\mathrm{e}^{-\imath\omega_0 t'}\frac{\partial c_0(t')}{\partial t'} - \imath\omega_0 c_0(t')\mathrm{e}^{-\imath\omega_0 t'} &= -\imath\omega_0 c_0(t')\mathrm{e}^{-\imath\omega_0 t'} - \imath/\hbar\Big(\;\mathcal{E}_{\mathrm{Laser}}(t')c_1(t')\mathrm{e}^{-\imath\omega_1 t'}\mu_{01} \\
&\qquad +\mathcal{E}_{\mathrm{Laser}}(t')c_3(t')\mathrm{e}^{-\imath\omega_3 t'}\mu_{03}\Big) \\
\mathrm{e}^{-\imath\omega_0 t}\mathrm{d}c_0 &= -\imath/\hbar\Big(\mathcal{E}_{\mathrm{Laser}}(t')c_1(t')\mathrm{e}^{-\imath\omega_1 t'}\mu_{01} \\
&\qquad +\mathcal{E}_{\mathrm{Laser}}(t')c_3(t')\mathrm{e}^{-\imath\omega_3 t'}\mu_{03}\Big)\mathrm{d}t' \\
c_0(t) &= -\imath/\hbar\int_{-\infty}^{t}\Big(\mathcal{E}_{\mathrm{Laser}}(t')c_1(t')\mathrm{e}^{-\imath(\omega_1-\omega_0)t'}\mu_{01} \\
&\qquad +\mathcal{E}_{\mathrm{Laser}}(t')c_3(t')\mathrm{e}^{-\imath(\omega_3-\omega_0)t'}\mu_{03}\Big)\mathrm{d}t' \qquad \text{(B.11)} \\
c_1(t) &= -\imath/\hbar\int_{-\infty}^{t}\Big(\mathcal{E}_{\mathrm{Laser}}(t')c_0(t')\mathrm{e}^{-\imath(\omega_0-\omega_1)t'}\mu_{10} \\
&\qquad +\mathcal{E}_{\mathrm{Laser}}(t')c_2(t')\mathrm{e}^{-\imath(\omega_2-\omega_1)t'}\mu_{12}\Big)\mathrm{d}t' \qquad \text{(B.12)} \\
c_2(t) &= -\imath/\hbar\int_{-\infty}^{t}\Big(\mathcal{E}_{\mathrm{Laser}}(t')c_1(t')\mathrm{e}^{-\imath(\omega_1-\omega_2)t'}\mu_{21} \\
&\qquad +\mathcal{E}_{\mathrm{Laser}}(t')c_3(t')\mathrm{e}^{-\imath(\omega_3-\omega_2)t'}\mu_{23}\Big)\mathrm{d}t' \qquad \text{(B.13)} \\
c_3(t) &= -\imath/\hbar\int_{-\infty}^{t}\Big(\mathcal{E}_{\mathrm{Laser}}(t')c_0(t')\mathrm{e}^{-\imath(\omega_0-\omega_3)t'}\mu_{30} \\
&\qquad +\mathcal{E}_{\mathrm{Laser}}(t')c_2(t')\mathrm{e}^{-\imath(\omega_2-\omega_3)t'}\mu_{32}\Big)\mathrm{d}t' \qquad \text{(B.14)}
\end{aligned}
$$

B.4 Solving First Order Perturbation Theory for One-XUV-Photon Transitions

The excitation for the direct one-XUV-photon transitions c_1 and c_3 are given as a perturbative solution, including the subsequent evolution as a function of time t. The XUV-Field here is assumed to be centered at t=0. The spectrum of the pulse does not cover the low frequency part (this will be covered by a second pulse in the visible range and is established in the experiment using a aluminum filter), so $c_2 = 0$. The whole population is in the ground state for negative times, $c_0(t < 0) = 1$. Since the state $|\varphi_1\rangle$ will decay into $|\varphi_0\rangle$ via dipole interaction with a lifetime $\tau_1 = 1/\Gamma_1$. Therefor a factor $\mathrm{e}^{\frac{-\Gamma_1}{2}t}$ appears additionally.

$$c_1(t) = (-\imath/\hbar)\,\mathrm{e}^{\frac{-\Gamma_1}{2}t} \int_{-\infty}^{t} \mu_{10}\mathcal{E}_{\mathrm{XUV}}(t')c_0(t')\mathrm{e}^{-\imath(\omega_0-\omega_1)t'}\,\mathrm{d}t' \tag{B.15}$$

$$c_3(t) = (-\imath/\hbar)\,\mathrm{e}^{-\frac{\Gamma_3}{2}t} \int_{-\infty}^{t} \mu_{30}\mathcal{E}_{\mathrm{XUV}}(t')c_0(t')\mathrm{e}^{-\imath(\omega_0-\omega_3)t'}\,\mathrm{d}t' \tag{B.16}$$

B.5 Solving Higher-Order Perturbation Theory for Three-Photon Transitions

After the excitation with one XUV-photon two transition by the VIS-field at t= τ following via the intermediate state $|\varphi_2\rangle$. For an intense few-cycle visible laser pulse, absorbing or emitting one photon can occur at the rising edge and again in the falling edge or somewhere in between. This leads to an additional phase which is picked up during the time in the intermediate state $|\varphi_2\rangle$. Since the duration of the VIS-field is short compared to the lifetime, we for now ignore this additional time in the intermediate state and assume an instantaneous absorption of two VIS-photons. This leads to the following description of the electric field: $\mathcal{E}_{\mathrm{Laser}} = \mathcal{E}_{\mathrm{XUV}}\delta(t-t_1) + \mathcal{E}_{\mathrm{VIS}}\delta(t-t_2) + \mathcal{E}_{\mathrm{VIS}}\delta(t-t_2)$. We choose the arrival time of the XUV-pulse $t_1 = 0$ and $t_2 = \tau - t_1$ with the time delay to the two other pulses τ and get: $\mathcal{E}_{\mathrm{Laser}} = \mathcal{E}_{\mathrm{XUV}}\delta(t) + \mathcal{E}_{\mathrm{VIS}}\delta(t-\tau) + \mathcal{E}_{\mathrm{VIS}}\delta(t-\tau)$. For population ending

up in $|\varphi_1\rangle$ or $|\varphi_3\rangle$ before decaying into the ground state, we have 3 contributions each:

$$c_1(t) = \left(-\imath/\hbar\right)\int_{-\infty}^{t}\left(\mathcal{E}_{\mathrm{XUV}}\delta(t') + \mathcal{E}_{\mathrm{VIS}}\delta(t'-\tau) + \mathcal{E}_{\mathrm{VIS}}\delta(t'-\tau)\right) \tag{B.17}$$
$$\mathrm{e}^{-\frac{\Gamma_1}{2}(t')}\left[c_0(t')\mu_{10}\mathrm{e}^{-\imath(\omega_0-\omega_1)t'} + c_2(t')\mu_{12}\mathrm{e}^{-\imath(\omega_2-\omega_1)t'}\right]\mathrm{d}t'$$

$$= \left(-\imath/\hbar\right)\mathrm{e}^{-\frac{\Gamma_1}{2}(t)}\int_{-\infty}^{t}\left(\mathcal{E}_{\mathrm{XUV}}\delta(t') + \mathcal{E}_{\mathrm{VIS}}\delta(t'-\tau) + \mathcal{E}_{\mathrm{VIS}}\delta(t'-\tau)\right)$$
$$\left[1\cdot\mu_{10}\mathrm{e}^{-\imath(\omega_0-\omega_1)t'} + \left(-\imath/\hbar\right)\mathrm{e}^{-\frac{\Gamma_2}{2}(t')}\int_{-\infty}^{t'}\left(\mathcal{E}_{\mathrm{XUV}}\delta(t'') + \mathcal{E}_{\mathrm{VIS}}\delta(t''-\tau) + \mathcal{E}_{\mathrm{VIS}}\delta(t''-\tau)\right)\right.$$
$$\left.\left\{c_1(t'')\mu_{21}\mathrm{e}^{-\imath(\omega_1-\omega_2)t''} + c_3(t'')\mu_{23}\mathrm{e}^{-\imath(\omega_3-\omega_2)t''}\right\}\mathrm{d}t''\mu_{12}\mathrm{e}^{-\imath(\omega_2-\omega_1)t'}\right]dt' \tag{B.18}$$

$$= \left(-\imath/\hbar\right)\mathrm{e}^{-\frac{\Gamma_1}{2}(t)}\int_{-\infty}^{t}\left(\mathcal{E}_{\mathrm{XUV}}\delta(t') + \mathcal{E}_{\mathrm{VIS}}\delta(t'-\tau) + \mathcal{E}_{\mathrm{VIS}}\delta(t'-\tau)\right)$$
$$\left[1\cdot\mu_{10}\mathrm{e}^{-\imath(\omega_0-\omega_1)t'} + \left(-\imath/\hbar\right)\mathrm{e}^{-\frac{\Gamma_2}{2}(t')}\int_{-\infty}^{t'}\left(\mathcal{E}_{\mathrm{XUV}}\delta(t'') + \mathcal{E}_{\mathrm{VIS}}\delta(t''-\tau) + \mathcal{E}_{\mathrm{VIS}}\delta(t''-\tau)\right)\right.$$
$$\left\{\left(-\imath/\hbar\right)\mathrm{e}^{-\frac{\Gamma_1}{2}(t'')}\int_{-\infty}^{t''<\tau}\left(\mathcal{E}_{\mathrm{XUV}}\delta(t''') + \mathcal{E}_{\mathrm{VIS}}\delta(t'''-\tau) + \mathcal{E}_{\mathrm{VIS}}\delta(t'''-\tau)\right)\right.$$
$$\left.\left(c_0(t''')\mu_{10}\mathrm{e}^{-\imath(\omega_0-\omega_1)t'''} + c_2(t''')\mu_{12}\mathrm{e}^{-\imath(\omega_2-\omega_1)t'''}\right)\mathrm{d}t'''\mu_{21}\mathrm{e}^{-\imath(\omega_1-\omega_2)t''}\right.$$
$$+\left(-\imath/\hbar\right)\mathrm{e}^{-\frac{\Gamma_3}{2}(t'')}\int_{-\infty}^{t''<\tau}\left(\mathcal{E}_{\mathrm{XUV}}\delta(t''') + \mathcal{E}_{\mathrm{VIS}}\delta(t'''-\tau) + \mathcal{E}_{\mathrm{VIS}}\delta(t'''-\tau)\right)$$
$$\left.\left(c_0(t''')\mu_{30}\mathrm{e}^{-\imath(\omega_0-\omega_3)t'''} + c_2(t''')\mu_{32}\mathrm{e}^{-\imath(\omega_2-\omega_3)t'''}\right)\mathrm{d}t'''\mu_{23}\mathrm{e}^{-\imath(\omega_3-\omega_2)t''}\right\}\mathrm{d}t''$$
$$\left.\mu_{12}\mathrm{e}^{-\imath(\omega_2-\omega_1)t'}\right]\mathrm{d}t' \tag{B.19}$$

$$= \left(-\imath/\hbar\right)\mathrm{e}^{-\frac{\Gamma_1}{2}(t)} \int_{-\infty}^{t} \left(\mathcal{E}_{\mathrm{XUV}}\delta(t') + \mathcal{E}_{\mathrm{VIS}}\delta(t'-\tau) + \mathcal{E}_{\mathrm{VIS}}\delta(t'-\tau)\right) \Bigg[1 \cdot \mu_{10}\mathrm{e}^{-\imath(\omega_0-\omega_1)t'} \tag{B.20}$$

$$+ \left(-\imath/\hbar\right)\mathrm{e}^{-\frac{\Gamma_2}{2}(t')} \int_{-\infty}^{t'} \left(\mathcal{E}_{\mathrm{XUV}}\delta(t'') + \mathcal{E}_{\mathrm{VIS}}\delta(t''-\tau) + \mathcal{E}_{\mathrm{VIS}}\delta(t''-\tau)\right)$$

$$\Bigg\{ \left(-\imath/\hbar\right)\mathrm{e}^{-\frac{\Gamma_1}{2}(t'')}\mathcal{E}_{\mathrm{XUV}} \Bigg(c_0(t''<\tau)\mu_{10}\mathrm{e}^{-\imath(\omega_0-\omega_1)t''} + c_2(t''<\tau)\mu_{12}$$

$$\mathrm{e}^{-\imath(\omega_2-\omega_1)t''} \Bigg) \mu_{21}\mathrm{e}^{-\imath(\omega_1-\omega_2)t''}$$

$$+ \left(-\imath/\hbar\right)\mathrm{e}^{-\frac{\Gamma_3}{2}(t'')}\mathcal{E}_{\mathrm{XUV}} \Bigg(c_0(t''<\tau)\mu_{30}\mathrm{e}^{-\imath(\omega_0-\omega_3)t''}$$

$$+ c_2(t''<\tau)\mu_{32}\mathrm{e}^{-\imath(\omega_2-\omega_3)t''} \Bigg) \mu_{23}\mathrm{e}^{-\imath(\omega_3-\omega_2)t''}$$

$$\Bigg\} \mathrm{d}t''\mu_{12}\mathrm{e}^{-\imath(\omega_2-\omega_1)t'} \Bigg] \mathrm{d}t'$$

$$= \left(-\imath/\hbar\right)\mathrm{e}^{-\frac{\Gamma_1}{2}(t)} \int_{-\infty}^{t} \left(\mathcal{E}_{\mathrm{XUV}}\delta(t') + \mathcal{E}_{\mathrm{VIS}}\delta(t'-\tau) + \mathcal{E}_{\mathrm{VIS}}\delta(t'-\tau)\right) \Bigg[1 \cdot \mu_{10}\mathrm{e}^{-\imath(\omega_0-\omega_1)t'} \tag{B.21}$$

$$+ \left(-\imath/\hbar\right)^2\mathrm{e}^{-\frac{\Gamma_2}{2}(t')} \int_{-\infty}^{t'} \left(\mathcal{E}_{\mathrm{XUV}}\delta(t'') + \mathcal{E}_{\mathrm{VIS}}\delta(t''-\tau) + \mathcal{E}_{\mathrm{VIS}}\delta(t''-\tau)\right)$$

$$\Bigg\{ \mathrm{e}^{-\frac{\Gamma_1}{2}(t'')}\mathcal{E}_{\mathrm{XUV}}\mu_{21}\mu_{10}\mathrm{e}^{-\imath(\omega_0-\omega_2)t''} + \mathrm{e}^{-\frac{\Gamma_3}{2}(t'')}\mathcal{E}_{\mathrm{XUV}}\mu_{23}\mu_{30}\mathrm{e}^{-\imath(\omega_0-\omega_2)t''} \Bigg\} \mathrm{d}t''$$

$$\mu_{12}\mathrm{e}^{-\imath(\omega_2-\omega_1)t'} \Bigg] \mathrm{d}t'$$

$$= \left(-\imath/\hbar\right)\mathrm{e}^{-\frac{\Gamma_1}{2}(t)} \int_{t'-\epsilon}^{t} \left(\mathcal{E}_{\mathrm{XUV}}\delta(t') + \mathcal{E}_{\mathrm{VIS}}\delta(t'-\tau) + \mathcal{E}_{\mathrm{VIS}}\delta(t'-\tau)\right)$$

$$\Bigg[1 \cdot \mu_{10}\mathrm{e}^{-\imath(\omega_0-\omega_1)t'} + \left(-\imath/\hbar\right)^2\mathrm{e}^{-\frac{\Gamma_2}{2}(t')} \int_{t''>0}^{t'=t''+\epsilon} \left(\mathcal{E}_{\mathrm{XUV}}\delta(t'') + \mathcal{E}_{\mathrm{VIS}}\delta(t''-\tau) + \mathcal{E}_{\mathrm{VIS}}\delta(t''-\tau)\right)$$

$$\Bigg\{ \mathrm{e}^{-\frac{\Gamma_1}{2}(t'')}\mathcal{E}_{\mathrm{XUV}}\mu_{21}\mu_{10}\mathrm{e}^{-\imath(\omega_0-\omega_2)t''} + \mathrm{e}^{-\frac{\Gamma_3}{2}(t'')}\mathcal{E}_{\mathrm{XUV}}\mu_{23}\mu_{30}\mathrm{e}^{-\imath(\omega_0-\omega_2)t''}$$

$$\Bigg\} \mathrm{d}t''\mu_{12}\mathrm{e}^{-\imath(\omega_2-\omega_1)t'} \Bigg] \mathrm{d}t'$$

(B.22)

$$
\begin{aligned}
c_1(t) = \; & \left(-\imath/\hbar\right) \int_{-\infty}^{t} \mu_{10}\mathcal{E}_{\mathrm{XUV}}\delta(t')\mathrm{e}^{-\frac{\Gamma_1}{2}(t')}\mathrm{e}^{-\imath(\omega_1-\omega_0)t'}\,\mathrm{d}t' \\
& +\left(-\imath/\hbar\right)^3 \int_{-\infty}^{t}\int_{-\infty}^{t'}\int_{-\infty}^{t''} \mu_{12}\mathcal{E}_{\mathrm{VIS}}\delta(t'-\tau)\mathrm{e}^{-(\frac{\Gamma_2}{2}+\frac{\Gamma_1}{2})t'}\mathrm{e}^{-\imath(\omega_1-\omega_2)t'} \\
& \qquad \mu_{21}\mathcal{E}_{\mathrm{VIS}}\delta(t''-\tau)\mathrm{e}^{-(\frac{\Gamma_2}{2}+\frac{\Gamma_1}{2})t''}\mathrm{e}^{-\imath(\omega_2-\omega_1)t''} \\
& \qquad \mu_{10}\mathcal{E}_{\mathrm{XUV}}\delta(t''')\mathrm{e}^{-\frac{\Gamma_1}{2}t'''}\mathrm{e}^{-\imath(\omega_1-\omega_0)t'''}\,\mathrm{d}t'''\mathrm{d}t''\mathrm{d}t' \\
& +\left(-\imath/\hbar\right)^3 \int_{-\infty}^{t}\int_{-\infty}^{t'}\int_{-\infty}^{t''} \mu_{12}\mathcal{E}_{\mathrm{VIS}}\delta(t'-\tau)\mathrm{e}^{-(\frac{\Gamma_2}{2}+\frac{\Gamma_1}{2})t'}\mathrm{e}^{-\imath(\omega_1-\omega_2)t'} \\
& \qquad \mu_{23}\mathcal{E}_{\mathrm{VIS}}\delta(t''-\tau)\mathrm{e}^{-(\frac{\Gamma_2}{2}+\frac{\Gamma_3}{2})(t''}\mathrm{e}^{-\imath(\omega_2-\omega_3)t''} \\
& \qquad \mu_{30}\mathcal{E}_{\mathrm{XUV}}\delta(t''')\mathrm{e}^{-\frac{\Gamma_3}{2}t'''}\mathrm{e}^{-\imath(\omega_3-\omega_0)t'''}\,\mathrm{d}t'''\mathrm{d}t''\mathrm{d}t'
\end{aligned}
\tag{B.23}
$$

$$
\begin{aligned}
= \; & \left(-\imath/\hbar\right)\mu_{10}\mathcal{E}_{\mathrm{XUV}} \\
& +\left(\imath/\hbar^3\right)\mu_{12}\mu_{21}\mu_{10}\mathcal{E}_{\mathrm{XUV}}E_{\mathrm{VIS}}^2\mathrm{e}^{-(\Gamma_2+\Gamma_1)\tau}\Theta(t-\tau) \\
& +\left(\imath/\hbar^3\right)\mu_{12}\mu_{23}\mu_{30}\mathcal{E}_{\mathrm{XUV}}E_{\mathrm{VIS}}^2\mathrm{e}^{-(\frac{\Gamma_3}{2}+2\frac{\Gamma_2}{2}+\frac{\Gamma_1}{2})\tau}\mathrm{e}^{-\imath(\omega_1-\omega_3)\tau}\Theta(t-\tau)
\end{aligned}
\tag{B.24}
$$

$$
\begin{aligned}
c_3(t) = \; & \left(-\imath/\hbar\right)\mu_{30}\mathcal{E}_{\mathrm{XUV}} \\
& +\left(\imath/\hbar^3\right)\mu_{32}\mu_{23}\mu_{30}\mathcal{E}_{\mathrm{XUV}}E_{\mathrm{VIS}}^2\mathrm{e}^{-(\Gamma_2+\Gamma_3)\tau}\Theta(t-\tau) \\
& +\left(\imath/\hbar^3\right)\mu_{32}\mu_{21}\mu_{10}\mathcal{E}_{\mathrm{XUV}}E_{\mathrm{VIS}}^2\mathrm{e}^{-(\frac{\Gamma_3}{2}+2\frac{\Gamma_2}{2}+\frac{\Gamma_1}{2})\tau}\mathrm{e}^{-\imath(\omega_3-\omega_1)\tau}\Theta(t-\tau)
\end{aligned}
\tag{B.25}
$$

In the following we only treat cases in which the coupling VIS pulses arrive within 2 cycles of light after the XUV excitation. Also both VIS photons will be absorped simultaneously, therefor leaving no time for the state $|2\rangle$ to evolve, canveling out all factors $\mathrm{e}^{\Gamma_2/2t}$. The resulting coefficients are

$$
\begin{aligned}
c_1(t) = \; & \left(-\imath/\hbar\right)\mu_{10}\mathcal{E}_{\mathrm{XUV}} \\
& +\left(\imath/\hbar^3\right)\mu_{12}\mu_{21}\mu_{10}\mathcal{E}_{\mathrm{XUV}}E_{\mathrm{VIS}}^2\mathrm{e}^{-\Gamma_1\tau} \\
& +\left(\imath/\hbar^3\right)\mu_{12}\mu_{23}\mu_{30}\mathcal{E}_{\mathrm{XUV}}E_{\mathrm{VIS}}^2\mathrm{e}^{-(\frac{\Gamma_3}{2}+\frac{\Gamma_1}{2})\tau}\mathrm{e}^{-\imath(\omega_1-\omega_3)\tau}
\end{aligned}
\tag{B.26}
$$

$$
\begin{aligned}
c_3(t) = \; & \left(-\imath/\hbar\right)\mu_{30}\mathcal{E}_{\mathrm{XUV}} \\
& +\left(\imath/\hbar^3\right)\mu_{32}\mu_{23}\mu_{30}\mathcal{E}_{\mathrm{XUV}}E_{\mathrm{VIS}}^2\mathrm{e}^{-\Gamma_3\tau} \\
& +\left(\imath/\hbar^3\right)\mu_{32}\mu_{21}\mu_{10}\mathcal{E}_{\mathrm{XUV}}E_{\mathrm{VIS}}^2\mathrm{e}^{-(\frac{\Gamma_3}{2}+\frac{\Gamma_1}{2})\tau}\mathrm{e}^{-\imath(\omega_3-\omega_1)\tau}
\end{aligned}
\tag{B.27}
$$

$$
\begin{aligned}
\sigma(\omega) = \frac{\omega}{c\epsilon_0}\Im\Bigg[\frac{1}{\mathscr{F}[E(t)]}\mathscr{F}\Big[& c_0^*(t)c_1(t)\mathrm{e}^{\imath(\omega_0-\omega_1)t}\mathrm{e}^{-\frac{\Gamma_1}{2}t}\mu_{01} + c_0^*(t)c_3(t)\mathrm{e}^{\imath(\omega_0-\omega_3)t}\mathrm{e}^{-\frac{\Gamma_3}{2}t}\mu_{03} \\
& + c_0(t)c_1^*(t)\mathrm{e}^{-\imath(\omega_0-\omega_1)t}\mathrm{e}^{-\frac{\Gamma_1}{2}t}\mu_{01} + c_0(t)c_3^*(t)\mathrm{e}^{-\imath(\omega_0-\omega_3)t}\mathrm{e}^{-\frac{\Gamma_3}{2}t}\mu_{03}\Big]\Bigg]
\end{aligned}
\tag{B.28}
$$

$$
\begin{aligned}
= \frac{\omega}{c\epsilon_0}\Im\Bigg[& \frac{\mathcal{E}_{\mathrm{XUV}}}{\int_{-\infty}^{\infty}\mathcal{E}_{\mathrm{XUV}}\delta(t)\mathrm{e}^{-\imath\omega t}\mathrm{d}t}\Bigg[\left(-\imath/\hbar\right)\mu_{10}^2\int_{-\infty}^{\infty}\Theta(t)\left(\mathrm{e}^{\imath(\omega_0-\omega_1)t}-\mathrm{e}^{-\imath(\omega_0-\omega_1)t}\right)\mathrm{e}^{-\frac{\Gamma_1}{2}t}\mathrm{e}^{-\imath\omega t}\mathrm{d}t \\
& +\left(\imath/\hbar^3\right)\mu_{12}^2\mu_{10}^2E_{\mathrm{VIS}}^2\mathrm{e}^{-\Gamma_1\tau}\int_{-\infty}^{\infty}\Theta(t)\Theta(t-\tau)\left(\mathrm{e}^{\imath(\omega_0-\omega_1)t}-\mathrm{e}^{-\imath(\omega_0-\omega_1)t}\right)\mathrm{e}^{-\frac{\Gamma_1}{2}t}\mathrm{e}^{-\imath\omega t}\mathrm{d}t \\
& +\left(\imath/\hbar^3\right)\mu_{01}\mu_{12}\mu_{23}\mu_{30}E_{\mathrm{VIS}}^2\mathrm{e}^{-(\frac{\Gamma_3}{2}+\frac{\Gamma_1}{2})\tau}\int_{-\infty}^{\infty}\Theta(t)\Big(\mathrm{e}^{\imath\left((\omega_0-\omega_1)t-(\omega_1-\omega_3)\tau\right)} \\
& \qquad -\mathrm{e}^{-\imath\left((\omega_0-\omega_1)t+(\omega_1-\omega_3)\tau\right)}\Big)\mathrm{e}^{-\frac{\Gamma_1}{2}t}\mathrm{e}^{-\imath\omega t}\mathrm{d}t \\
& -\left(\imath/\hbar\right)\mu_{30}^2\int_{-\infty}^{\infty}\Theta(t)\left(\mathrm{e}^{\imath(\omega_0-\omega_3)t}-\mathrm{e}^{-\imath(\omega_0-\omega_3)t}\right)\mathrm{e}^{-\frac{\Gamma_3}{2}t}\mathrm{e}^{-\imath\omega t}\mathrm{d}t \\
& +\left(\imath/\hbar^3\right)\mu_{23}^2\mu_{30}^2E_{\mathrm{VIS}}^2\mathrm{e}^{-\Gamma_3\tau}\int_{-\infty}^{\infty}\Theta(t)\left(\mathrm{e}^{\imath(\omega_0-\omega_3)t}-\mathrm{e}^{-\imath(\omega_0-\omega_3)t}\right)\mathrm{e}^{-\frac{\Gamma_3}{2}t}\mathrm{e}^{-\imath\omega t}\mathrm{d}t \\
& +\left(\imath/\hbar^3\right)\mu_{03}\mu_{32}\mu_{21}\mu_{10}E_{\mathrm{VIS}}^2\mathrm{e}^{-(\frac{\Gamma_3}{2}+\frac{\Gamma_1}{2})\tau}\int_{-\infty}^{\infty}\Theta(t)\Big(\mathrm{e}^{\imath\left((\omega_0-\omega_3)t-(\omega_3-\omega_1)\tau\right)} \\
& \qquad -\mathrm{e}^{-\imath\left((\omega_0-\omega_3)t+(\omega_3-\omega_1)\tau\right)}\Big)\mathrm{e}^{-\frac{\Gamma_3}{2}t}\mathrm{e}^{-\imath\omega t}\mathrm{d}t\Bigg]\Bigg]
\end{aligned}
\tag{B.29}
$$

$$
\begin{aligned}
= \frac{\omega}{c\epsilon_0}\Im\Bigg[& \left(-\imath/\hbar\right)\mu_{10}^2\int_0^{\infty}\left(\mathrm{e}^{-\left(\frac{\Gamma_1}{2}+\imath(\omega-\omega_0+\omega_1)\right)t}-\mathrm{e}^{-\left(\frac{\Gamma_1}{2}+\imath(\omega+\omega_0-\omega_1)\right)t}\right)\mathrm{d}t \\
& +\left(\imath/\hbar^3\right)\mu_{12}^2\mu_{10}^2E_{\mathrm{VIS}}^2\mathrm{e}^{-\Gamma_1\tau}\int_0^{\infty}\left(\mathrm{e}^{-\left(\frac{\Gamma_1}{2}+\imath(\omega-\omega_0+\omega_1)\right)t}-\mathrm{e}^{-\left(\frac{\Gamma_1}{2}+\imath(\omega+\omega_0-\omega_1)\right)t}\right)\mathrm{d}t \\
& +\left(\imath/\hbar^3\right)\mu_{01}\mu_{12}\mu_{23}\mu_{30}E_{\mathrm{VIS}}^2\mathrm{e}^{-(\frac{\Gamma_3}{2}+\frac{\Gamma_1}{2})\tau}\int_0^{\infty}\Big(\mathrm{e}^{-\left(\frac{\Gamma_1}{2}+\imath(\omega-\omega_0+\omega_1)\right)t-\imath(\omega_1-\omega_3)\tau} \\
& \qquad -\mathrm{e}^{-\left(\frac{\Gamma_1}{2}+\imath(\omega+\omega_0-\omega_1)\right)t+\imath(\omega_1-\omega_3)\tau}\Big)\mathrm{d}t \\
& -\left(\imath/\hbar\right)\mu_{30}^2\int_0^{\infty}\left(\mathrm{e}^{-\left(\frac{\Gamma_3}{2}+\imath(\omega-\omega_0+\omega_3)\right)t}-\mathrm{e}^{-\left(\frac{\Gamma_3}{2}+\imath(\omega+\omega_0-\omega_3)\right)t}\right)\mathrm{d}t \\
& +\left(\imath/\hbar^3\right)\mu_{23}^2\mu_{30}^2E_{\mathrm{VIS}}^2\mathrm{e}^{-\Gamma_3\tau}\int_0^{\infty}\left(\mathrm{e}^{-\left(\frac{\Gamma_3}{2}+\imath(\omega-\omega_0+\omega_3)\right)t}-\mathrm{e}^{-\left(\frac{\Gamma_3}{2}+\imath(\omega+\omega_0-\omega_3)\right)t}\right)\mathrm{d}t \\
& +\left(\imath/\hbar^3\right)\mu_{03}\mu_{32}\mu_{21}\mu_{10}E_{\mathrm{VIS}}^2\mathrm{e}^{-(\frac{\Gamma_3}{2}+\frac{\Gamma_1}{2})\tau}\int_0^{\infty}\Big(\mathrm{e}^{-\left(\frac{\Gamma_3}{2}+\imath(\omega-\omega_0+\omega_3)\right)t-\imath(\omega_3-\omega_1)\tau} \\
& \qquad -\mathrm{e}^{-\left(\frac{\Gamma_3}{2}+\imath(\omega+\omega_0-\omega_3)\right)t+\imath(\omega_3-\omega_1)\tau}\Big)\mathrm{d}t\Bigg]\Bigg]
\end{aligned}
\tag{B.30}
$$

$$
\begin{aligned}
= \frac{\omega}{c\epsilon_0}\Im\Bigg[& \left(-\imath/\hbar\right)\mu_{10}^2\left(\frac{1}{\frac{\Gamma_1}{2}+\imath(\omega-\omega_0+\omega_1)}-\frac{1}{\frac{\Gamma_1}{2}+\imath(\omega+\omega_0-\omega_1)}\right)\\
&+\left(\imath/\hbar^3\right)\mu_{12}^2\mu_{10}^2E_{\mathrm{VIS}}^2\mathrm{e}^{-\Gamma_1\tau}\left(\frac{1}{\frac{\Gamma_1}{2}+\imath(\omega-\omega_0+\omega_1)}-\frac{1}{\frac{\Gamma_1}{2}+\imath(\omega+\omega_0-\omega_1)t}\right)\\
&+\left(\imath/\hbar^3\right)\mu_{01}\mu_{12}\mu_{23}\mu_{30}E_{\mathrm{VIS}}^2\mathrm{e}^{-(\frac{\Gamma_3}{2}+\frac{\Gamma_1}{2})\tau}\left(\frac{\mathrm{e}^{-\imath(\omega_1-\omega_3)\tau}}{\frac{\Gamma_1}{2}+\imath(\omega-\omega_0+\omega_1)}-\frac{\mathrm{e}^{\imath(\omega_1-\omega_3)\tau}}{\frac{\Gamma_1}{2}+\imath(\omega+\omega_0-\omega_1)}\right)\\
&-\left(\imath/\hbar\right)\mu_{30}^2\left(\frac{1}{\frac{\Gamma_3}{2}+\imath(\omega-\omega_0+\omega_3)}-\frac{1}{\frac{\Gamma_3}{2}+\imath(\omega+\omega_0-\omega_3)}\right)\\
&+\left(\imath/\hbar^3\right)\mu_{23}^2\mu_{30}^2E_{\mathrm{VIS}}^2\mathrm{e}^{-\Gamma_3\tau}\left(\frac{1}{\frac{\Gamma_3}{2}+\imath(\omega-\omega_0+\omega_3)}-\frac{1}{\frac{\Gamma_3}{2}+\imath(\omega+\omega_0-\omega_3)}\right)\\
&+\left(\imath/\hbar^3\right)\mu_{03}\mu_{32}\mu_{21}\mu_{10}E_{\mathrm{VIS}}^2\mathrm{e}^{-(\frac{\Gamma_3}{2}+\frac{\Gamma_1}{2})\tau}\left(\frac{\mathrm{e}^{-\imath(\omega_3-\omega_1)\tau}}{\frac{\Gamma_3}{2}+\imath(\omega-\omega_0+\omega_3)}-\frac{\mathrm{e}^{\imath(\omega_3-\omega_1)\tau}}{\frac{\Gamma_3}{2}+\imath(\omega+\omega_0-\omega_3)}\right)\Bigg]
\end{aligned}
\tag{B.31}
$$

We now introduce the ith state to ground state difference energy to be $\Delta_i = \omega_i - \omega_0$ and the normalized energy $\epsilon_i = \frac{\omega-\Delta_i}{\Gamma_i/2}$. Additionally we only look at positive frequencies, thus neglecting all denominators containing Terms proportional to $\omega + \Delta_i$.

$$
\begin{aligned}
= \frac{\omega}{c\epsilon_0}\Im\Bigg[& \left(-\imath/\hbar\right)\mu_{10}^2\frac{2}{\Gamma_1}\frac{1}{1+\imath\epsilon_1}\\
&+\left(\imath/\hbar^3\right)\mu_{12}^2\mu_{10}^2E_{\mathrm{VIS}}^2\frac{2}{\Gamma_1}\frac{1}{1+\imath\epsilon_1}\\
&+\left(\imath/\hbar^3\right)\mu_{01}\mu_{12}\mu_{23}\mu_{30}E_{\mathrm{VIS}}^2\frac{2}{\Gamma_1}\frac{\mathrm{e}^{-\imath(\omega_1-\omega_3)\tau}}{1+\imath\epsilon_1}\\
&-\left(\imath/\hbar\right)\mu_{30}^2\frac{2}{\Gamma_3}\frac{1}{1+\imath\epsilon_3}\\
&+\left(\imath/\hbar^3\right)\mu_{23}^2\mu_{30}^2E_{\mathrm{VIS}}^2\frac{2}{\Gamma_3}\frac{1}{1+\imath\epsilon_3}\\
&+\left(\imath/\hbar^3\right)\mu_{03}\mu_{32}\mu_{21}\mu_{10}E_{\mathrm{VIS}}^2\frac{2}{\Gamma_3}\frac{\mathrm{e}^{-\imath(\omega_3-\omega_1)\tau}}{1+\imath\epsilon_3}\Bigg]
\end{aligned}
\tag{B.32}
$$

$$
\begin{aligned}
= \frac{\omega}{c\epsilon_0}\Im\Bigg[& \left(-\imath/\hbar\right)\mu_{10}^2\frac{2}{\Gamma_1}\frac{1-\imath\epsilon_1}{1+\epsilon_1^2} \\
& +\left(\imath/\hbar^3\right)\mu_{12}^2\mu_{10}^2E_{\mathrm{VIS}}^2\frac{2}{\Gamma_1}\frac{1-\imath\epsilon_1}{1+\epsilon_1^2} \\
& +\left(\imath/\hbar^3\right)\mu_{01}\mu_{12}\mu_{23}\mu_{30}E_{\mathrm{VIS}}^2\frac{2}{\Gamma_1}\frac{(1-\imath\epsilon_1)\,\mathrm{e}^{-\imath(\omega_1-\omega_3)\tau}}{1+\epsilon_1^2} \\
& -\left(\imath/\hbar\right)\mu_{30}^2\frac{2}{\Gamma_3}\frac{1-\imath\epsilon_3}{1+\epsilon_3^2} \\
& +\left(\imath/\hbar^3\right)\mu_{23}^2\mu_{30}^2E_{\mathrm{VIS}}^2\frac{2}{\Gamma_3}\frac{1-\imath\epsilon_3}{1+\epsilon_3^2} \\
& +\left(\imath/\hbar^3\right)\mu_{03}\mu_{32}\mu_{21}\mu_{10}E_{\mathrm{VIS}}^2\frac{2}{\Gamma_3}\frac{(1-\imath\epsilon_3)\,\mathrm{e}^{-\imath(\omega_3-\omega_1)\tau}}{1+\epsilon_3^2}\Bigg]
\end{aligned}
\tag{B.33}
$$

$$
\begin{aligned}
= \frac{\omega}{c\epsilon_0}\Im\Bigg[& \left(-1/\hbar\right)\mu_{10}^2\frac{2}{\Gamma_1}\frac{\imath+\epsilon_1}{1+\epsilon_1^2} \\
& +\left(1/\hbar^3\right)\mu_{12}^2\mu_{10}^2E_{\mathrm{VIS}}^2\frac{2}{\Gamma_1}\frac{\imath+\epsilon_1}{1+\epsilon_1^2} \\
& +\left(1/\hbar^3\right)\mu_{01}\mu_{12}\mu_{23}\mu_{30}E_{\mathrm{VIS}}^2\frac{2}{\Gamma_1}\frac{(1-\imath\epsilon_1)\Big(\cos\left((\omega_1-\omega_3)\tau\right)-\imath\sin\left((\omega_1-\omega_3)\tau\right)\Big)}{1+\epsilon_1^2} \\
& -\left(1/\hbar\right)\mu_{30}^2\frac{2}{\Gamma_3}\frac{\imath+\epsilon_3}{1+\epsilon_3^2} \\
& +\left(1/\hbar^3\right)\mu_{23}^2\mu_{30}^2E_{\mathrm{VIS}}^2\frac{2}{\Gamma_3}\frac{\imath+\epsilon_3}{1+\epsilon_3^2} \\
& +\left(\imath/\hbar^3\right)\mu_{03}\mu_{32}\mu_{21}\mu_{10}E_{\mathrm{VIS}}^2\frac{2}{\Gamma_3}\frac{(1-\imath\epsilon_3)\Big(\cos\left((\omega_3-\omega_1)\tau\right)-\imath\sin\left((\omega_3-\omega_1)\tau\right)\Big)}{1+\epsilon_3^2}\Bigg]
\end{aligned}
\tag{B.34}
$$

$$
\begin{aligned}
&= \frac{\omega}{c\epsilon_0} \left(-1/\hbar\right)\mu_{10}^2 \frac{2}{\Gamma_1}\frac{1}{1+\epsilon_1^2} \\
&\quad +\left(1/\hbar^3\right)\mu_{12}^2\mu_{10}^2 E_{\mathrm{VIS}}^2 \frac{2}{\Gamma_1}\frac{1}{1+\epsilon_1^2} \\
&\quad +\left(1/\hbar^3\right)\mu_{01}\mu_{12}\mu_{23}\mu_{30} E_{\mathrm{VIS}}^2 \frac{2}{\Gamma_1}\frac{\cos\left((\omega_1-\omega_3)\,\tau\right)-\epsilon_1\sin\left((\omega_1-\omega_3)\,\tau\right)}{1+\epsilon_1^2} \\
&\quad -\left(1/\hbar\right)\mu_{30}^2 \frac{2}{\Gamma_3}\frac{1}{1+\epsilon_3^2} \\
&\quad +\left(1/\hbar^3\right)\mu_{23}^2\mu_{30}^2 E_{\mathrm{VIS}}^2 \frac{2}{\Gamma_3}\frac{1}{1+\epsilon_3^2} \\
&\quad +\left(1/\hbar^3\right)\mu_{03}\mu_{32}\mu_{21}\mu_{10} E_{\mathrm{VIS}}^2 \frac{2}{\Gamma_3}\frac{\cos\left((\omega_3-\omega_1)\,\tau\right)-\epsilon_3\sin\left((\omega_3-\omega_1)\,\tau\right)}{1+\epsilon_3^2}
\end{aligned}
\tag{B.35}
$$

$$
\begin{aligned}
&= \frac{\omega}{c\epsilon_0}\Im\Bigg[\left(-1/\hbar\right)\mu_{10}^2 \frac{2}{\Gamma_1}\frac{\imath+\epsilon_1}{1+\epsilon_1^2} \\
&\quad +\left(1/\hbar^3\right)\mu_{12}^2\mu_{10}^2 E_{\mathrm{VIS}}^2 \frac{2}{\Gamma_1}\frac{\imath+\epsilon_1}{1+\epsilon_1^2} \\
&\quad +\left(1/\hbar^3\right)\mu_{01}\mu_{12}\mu_{23}\mu_{30} E_{\mathrm{VIS}}^2 \frac{2}{\Gamma_1}\frac{(\imath+\epsilon_1)\,\mathrm{e}^{-\imath(\omega_1-\omega_3)\tau}}{1+\epsilon_1^2} \\
&\quad -\left(1/\hbar\right)\mu_{30}^2 \frac{2}{\Gamma_3}\frac{\imath+\epsilon_3}{1+\epsilon_3^2} \\
&\quad +\left(1/\hbar^3\right)\mu_{23}^2\mu_{30}^2 E_{\mathrm{VIS}}^2 \frac{2}{\Gamma_3}\frac{\imath+\epsilon_3}{1+\epsilon_3^2} \\
&\quad +\left(1/\hbar^3\right)\mu_{03}\mu_{32}\mu_{21}\mu_{10} E_{\mathrm{VIS}}^2 \frac{2}{\Gamma_3}\frac{(\imath+\epsilon_3)\,\mathrm{e}^{-\imath(\omega_3-\omega_1)\tau}}{1+\epsilon_3^2}\Bigg]
\end{aligned}
\tag{B.36}
$$

We only look at ω_1 and ignore the influence from the energetically well seperated state $|3\rangle$.

$$
\begin{aligned}
&= \frac{\omega}{c\epsilon_0}\Im\Bigg[\left(-3/\hbar\right)\mu_{10}^2 \frac{2}{\Gamma_1}\frac{\imath+\epsilon_1}{3+\epsilon_1^2} \\
&\quad +\left(3/\hbar^1\right)\mu_{21}^2\mu_{10}^2 E_{\mathrm{VIS}}^2 \frac{2}{\Gamma_1}\frac{\imath+\epsilon_1}{3+\epsilon_1^2} \\
&\quad +\left(3/\hbar^1\right)\mu_{01}\mu_{12}\mu_{23}\mu_{30} E_{\mathrm{VIS}}^2 \frac{2}{\Gamma_1}\frac{(\imath+\epsilon_1)\,\mathrm{e}^{-\imath(\omega_1-\omega_3)\tau}}{3+\epsilon_1^2}\Bigg]
\end{aligned}
\tag{B.37}
$$

We now write this Formula in atomic units, where $\hbar = 1, c = 137$ and $\epsilon_0 = \frac{1}{4\pi}$.

$$= \frac{8\pi\omega}{137\Gamma_1}\Im\Bigg[-\mu_{10}^2\frac{\imath+\epsilon_1}{3+\epsilon_1^2} + \mu_{21}^2\mu_{10}^2E_{\mathrm{VIS}}^2\frac{\imath+\epsilon_1}{3+\epsilon_1^2} \mu_{01}\mu_{12}\mu_{23}\mu_{30}E_{\mathrm{VIS}}^2\frac{(\imath+\epsilon_1)\mathrm{e}^{-\imath(\omega_1-\omega_3)\tau}}{3+\epsilon_1^2}\Bigg] \tag{B.38}$$

$$= \frac{4\pi}{137}\left(\epsilon_1+\frac{2\Delta_1}{\Gamma_1}\right)\Im\Bigg[-\mu_{10}^2\frac{\imath+\epsilon_1}{3+\epsilon_1^2} + \mu_{21}^2\mu_{10}^2E_{\mathrm{VIS}}^2\frac{\imath+\epsilon_1}{3+\epsilon_1^2} \mu_{01}\mu_{12}\mu_{23}\mu_{30}E_{\mathrm{VIS}}^2\frac{(\imath+\epsilon_1)\mathrm{e}^{-\imath(\omega_1-\omega_3)\tau}}{3+\epsilon_1^2}\Bigg] \tag{B.39}$$

For the lowest lying, dipole allowed doubly excited states in helium (2s2p and $sp_{2,3+}$) one has ${}^{2\Delta_i}/_{\Gamma_i} \gg \epsilon_i$ which leads to the simplyfied expression

$$= \frac{8\pi\Delta_1}{137\Gamma_1}\Im\Bigg[-\mu_{10}^2\frac{\imath+\epsilon_1}{3+\epsilon_1^2} + \mu_{21}^2\mu_{10}^2E_{\mathrm{VIS}}^2\frac{\imath+\epsilon_1}{3+\epsilon_1^2} \mu_{01}\mu_{12}\mu_{23}\mu_{30}E_{\mathrm{VIS}}^2\frac{(\imath+\epsilon_1)\mathrm{e}^{-\imath(\omega_1-\omega_3)\tau}}{3+\epsilon_1^2}\Bigg] \tag{B.40}$$

$$\sigma(\omega) = \frac{-4\pi}{137}\Im\left[\mu_{10}^2\frac{\omega}{\Gamma_1/2}\frac{\left(\imath+\frac{\omega-\omega_1}{\Gamma_{1/2}}\right)}{3+(\frac{\omega-\omega_1}{\Gamma_{1/2}})^2}\mathrm{e}^{-\imath\varphi_{original}}\right] \tag{B.41}$$

$$\sigma(\omega) = \mathrm{e}^{-\imath\varphi_{original}}\frac{8\pi\Delta_1}{137\Gamma_1}\Im\Bigg[-\mu_{10}^2\frac{\imath+\epsilon_1}{3+\epsilon_1^2} + \mu_{21}^2\mu_{10}^2E_{\mathrm{VIS}}^2\frac{\imath+\epsilon_1}{3+\epsilon_1^2} \mu_{01}\mu_{12}\mu_{23}\mu_{30}E_{\mathrm{VIS}}^2\frac{(\imath+\epsilon_1)\mathrm{e}^{-\imath\varphi}}{3+\epsilon_1^2}\Bigg]$$

$$\begin{aligned}\langle\psi(t)|(-er)|\psi(t)\rangle = &\Big(c_0^*(t)\mathrm{e}^{\imath\omega_0 t}\langle\varphi_0| + c_3^*(t)\mathrm{e}^{\imath\omega_3 t}\langle\varphi_3| + c_2^*(t)\mathrm{e}^{\imath\omega_2 t}\langle\varphi_2| + c_1^*(t)\mathrm{e}^{\imath\omega_1 t}\langle\varphi_1|\Big)\Big(-er\Big)\\ &\Big(c_0(t)\mathrm{e}^{-\imath\omega_0 t}|\varphi_0\rangle + c_3(t)\mathrm{e}^{-\imath\omega_3 t}|\varphi_3\rangle + c_2(t)\mathrm{e}^{-\imath\omega_2 t}|\varphi_2\rangle + c_1(t)\mathrm{e}^{-\imath\omega_1 t}|\varphi_1\rangle\Big)\\ = &\, c_0^*(t)c_3(t)\mathrm{e}^{\imath(\omega_0-\omega_3)t}\langle\varphi_0|(-er)|\varphi_3\rangle + c_0^*(t)c_1(t)\mathrm{e}^{\imath(\omega_0-\omega_1)t}\langle\varphi_0|(-er)|\varphi_1\rangle +\\ &\, c_2^*(t)c_3(t)\mathrm{e}^{\imath(\omega_2-\omega_3)t}\langle\varphi_2|(-er)|\varphi_3\rangle + c_2^*(t)c_1(t)\mathrm{e}^{\imath(\omega_2-\omega_1)t}\langle\varphi_2|(-er)|\varphi_1\rangle\end{aligned}$$

$$\sigma_{\text{modified}}(q_{\text{modified}},\epsilon) = A \cdot \frac{q^2_{\text{original}}+1}{q^2_{\text{modified}}+1} \cdot \frac{(q_{\text{modified}}+\epsilon)^2}{1+\epsilon^2} \tag{B.42}$$

$$d(t) = \delta(t) + \frac{\Gamma_1}{2} e^{-\Gamma/2t} (q_{\text{modified}} - i)^2 \mu_{01}^2 \Bigg(1 + e^{\imath\pi} E^2_{\text{VIS}} \frac{\mu^2_{21}}{\hbar^2} + e^{\imath\Delta\varphi_{13}} e^{\imath\Delta\omega_{13}\tau} E^2_{\text{VIS}} \frac{\mu_{12}\mu_{23}\mu 30}{\mu 01 \hbar^2} \Bigg) \tag{B.43}$$

Since we are interested in the dipole radiation from $|1\rangle$ to $|0\rangle$ we only need to calculate $c_0^*(t)c_1(t)e^{\imath(\omega_0-\omega_1)t}\langle\varphi_0|(-er)|\varphi_1\rangle$. Where $c_0^*(t) = 1$, $\langle\varphi_0|(-er)|\varphi_1\rangle = \mu_{01}$ and

$$\begin{aligned} c_1(t) = & \left(-\imath/\hbar\right)\mu_{10}\mathcal{E}_{\text{XUV}} \\ & + \left(\imath/\hbar^1\right)\mu_{12}\mu_{21}\mu_{10}\mathcal{E}_{\text{XUV}} E^2_{\text{VIS}} e^{-\Gamma_1\tau} \\ & + \left(\imath/\hbar^1\right)\mu_{12}\mu_{23}\mu_{30}\mathcal{E}_{\text{XUV}} E^2_{\text{VIS}} e^{-(\frac{\Gamma_1}{2}+\frac{\Gamma_3}{2})\tau} e^{-\imath(\omega_1-\omega_3)\tau} e^{\imath(\omega_0-\omega_1)t} \end{aligned}$$

which leads to the following solution:

$$\begin{aligned} < d(t) > = & \left(-\imath/\hbar\right)\mu_{10}^2\mathcal{E}_{\text{XUV}}\Theta(t)\left(e^{\imath(\omega_0-\omega_1)t} - e^{\imath(\omega_0-\omega_1)t}\right) \\ & + \left(\imath/\hbar^1\right)\mu_{12}^2\mu_{10}^2\mathcal{E}_{\text{XUV}}\Theta(t)E^2_{\text{VIS}}e^{-\Gamma_1\tau}\left(e^{\imath(\omega_0-\omega_1)t} - e^{\imath(\omega_0-\omega_1)t}\right) \\ & + \left(\imath/\hbar^1\right)\mu_{01}\mu_{12}\mu_{23}\mu_{30}\mathcal{E}_{\text{XUV}}\Theta(t)E^2_{\text{VIS}}e^{-(\frac{\Gamma_1}{2}+\frac{\Gamma_3}{2})\tau}e^{-\imath(\omega_1-\omega_3)\tau}\left(e^{\imath(\omega_0-\omega_1)t} - e^{\imath(\omega_0-\omega_1)t}\right) \end{aligned} \tag{B.44}$$

Together with the steps done in the previous paper (see supplement of [2]), we arrive at the full complex dipole moment in third order perturbation theory:

$$\begin{aligned} d(t) = \delta(t) + \frac{\Gamma_1}{2} e^{-\Gamma_1/2t} \frac{2\mu_{10}^2\mathcal{E}_{\text{XUV}}}{\hbar} \sin\left((\omega_0-\omega_1)t\right)\theta(t)\left(q_{\text{original}} - \imath\right)^2 \\ \left(1 - \frac{\mu^2_{12}}{\hbar^2}E^2_{\text{VIS}}e^{-\Gamma_1\tau} - \frac{\mu_{12}\mu_{23}\mu_{30}}{\hbar^2\mu_{01}}E^2_{\text{VIS}}e^{-(\frac{\Gamma_1}{2}+\frac{\Gamma_3}{2})\tau}e^{-\imath(\omega_1-\omega_3)\tau}\right) \end{aligned}$$

$$
\begin{aligned}
d(\omega) &= \int_{-\infty}^{\infty} dt\ \mathrm{e}^{-\imath\omega t} d(t) \\
&= \int_{-\infty}^{\infty} dt\ \mathrm{e}^{-\imath\omega t}\Bigg[\delta(t) + \frac{\Gamma_1}{2}\mathrm{e}^{-\Gamma_1/2 t}\frac{2\mu_{10}^2\mathcal{E}_{\mathrm{XUV}}}{\hbar}\sin\left((\omega_0-\omega_1)t\right)\theta(t)\left(q_{\mathrm{original}}-\imath\right)^2 \\
&\qquad\qquad \left(1 - \frac{\mu_{12}^2}{\hbar^2}E_{\mathrm{VIS}}^2\mathrm{e}^{-\Gamma_1\tau} - \frac{\mu_{12}\mu_{23}\mu_{30}}{\hbar^2\mu_{01}}E_{\mathrm{VIS}}^2\mathrm{e}^{-(\frac{\Gamma_1}{2}+\frac{\Gamma_3}{2})\tau}\mathrm{e}^{-\imath(\omega_1-\omega_3)\tau}\right)\Bigg] \\
&= 1 + \int_{-\infty}^{\infty} dt\ \theta(t)\left(\mathrm{e}^{\imath(\omega_0-\omega_1-\omega+\imath\Gamma_1/2)t} - \mathrm{e}^{-\imath(\omega_0-\omega_1+\omega-\imath\Gamma_1/2)t}\right)\frac{\Gamma_1\mu_{10}^2\mathcal{E}_{\mathrm{XUV}}}{2\imath\hbar}\left(q_{\mathrm{original}}-\imath\right)^2 \\
&\qquad\qquad \left(1 - \frac{\mu_{12}^2}{\hbar^2}E_{\mathrm{VIS}}^2\mathrm{e}^{-\Gamma_1\tau} - \frac{\mu_{12}\mu_{23}\mu_{30}}{\hbar^2\mu_{01}}E_{\mathrm{VIS}}^2\mathrm{e}^{-(\frac{\Gamma_1}{2}+\frac{\Gamma_3}{2})\tau}\mathrm{e}^{-\imath(\omega_1-\omega_3)\tau}\right)
\end{aligned}
$$

Neglecting the negative frequencies leads to

$$
\begin{aligned}
&= 1 + \frac{\Gamma_1\mu_{10}^2\mathcal{E}_{\mathrm{XUV}}}{\hbar\Gamma_1\left(\frac{\omega-\omega_1+\omega_3}{\Gamma_1/2}-\imath\right)}\left(q_{\mathrm{original}}-\imath\right)^2 \\
&\qquad \left(1 - \frac{\mu_{12}^2}{\hbar^2}E_{\mathrm{VIS}}^2\mathrm{e}^{-\Gamma_1\tau} - \frac{\mu_{12}\mu_{23}\mu_{30}}{\hbar^2\mu_{01}}E_{\mathrm{VIS}}^2\mathrm{e}^{-(\frac{\Gamma_1}{2}+\frac{\Gamma_3}{2})\tau}\mathrm{e}^{-\imath(\omega_1-\omega_3)\tau}\right)
\end{aligned}
$$

Introducing $\epsilon = \frac{\omega-\omega_1+\omega_3}{\Gamma_1/2}$ and writing each contribution in terms of Fano parameters gives

$$
\begin{aligned}
d(\omega) = 3 + \frac{\mu_{10}^2\mathcal{E}_{\mathrm{XUV}}}{\hbar(\epsilon-\imath)}\Bigg(&\left(q_{\mathrm{original}}^2+1\right)\mathrm{e}^{\imath\varphi_{\mathrm{original}}} + \left(q_3^2+1\right)\mathrm{e}^{\imath\left(\varphi_{\mathrm{original}}+\pi\right)} \\
&+\left(q_2^2+1\right)\mathrm{e}^{\imath\left(\varphi_{\mathrm{original}}+\pi-(\omega_1-\omega_3)\tau+\Delta\varphi_{13}\right)}\Bigg)
\end{aligned}
$$

with $q_3 = q_3(E_{\mathrm{VIS}},\tau,\mu_{12})$ and $q_2 = q_3(E_{\mathrm{VIS}},\tau,\mu_{12},\mu_{23})$. $\Delta\varphi_{13}$ is the phase differnce between the Fano Phase of state $|3\rangle$ und $|1\rangle$.
This sum of 3 complex Fano resonances again is a complex Fano resonace and can therefor be rewritten as

$$
d(\omega) = 1 + A\cdot\left(q_{\mathrm{original}}^2+1\right)\mathrm{e}^{\imath\varphi_{\mathrm{modified}}}\frac{\epsilon+i}{\epsilon^2+1}
$$

with $A = \frac{\mu_{01}^2 E_{\mathrm{XUV}}\left(\left(q_{\mathrm{original}}^2-q_3\right)^2+\left(q_2^2+1\right)^2-2\left(q_{\mathrm{original}}^2-q_3\right)\left(q_2^2+1\right)\cos\left((\omega_1-\omega_3)\tau+\Delta\varphi_{13}\right)\right)^{\frac{1}{2}}}{\hbar\left(q_{\mathrm{original}}^2+1\right)}$ and

$\varphi_{\mathrm{modified}} = \arctan\left(\left(q_{\mathrm{original}}^2-q_3^2\right)\tan\left(\varphi_{\mathrm{original}}\right) - \left(q_2^2+1\right)\tan\left(\varphi_{\mathrm{original}}+(\omega_1-\omega_3)\tau+\Delta\varphi_{13}\right)\right)$
which gives the follow cross section

$$
\sigma(\omega) = \sigma_0\frac{\omega}{c\epsilon_0}\Im\left[1 + A\cdot\left(q_{\mathrm{original}}^2+1\right)\mathrm{e}^{\imath\varphi_{\mathrm{modified}}}\frac{\epsilon+i}{\epsilon^2+1}\right]
$$

Appendix C

The optical density of helium

C.1 Fit of the non-resonant backgound

$$\sigma_0^{fit}(\omega) = a_0 + \sum_{k=1}^{k=5} a_k \omega^k$$

a_0	30.78865875723
a_1	−1.696014464231
a_2	0.04116820950202
a_3	−0.0005211442693275
a_4	$3.351095461225 \cdot 10^{-6}$
a_5	$-8.64455721385 \cdot 10^{-9}$

Table C.1: Tabulated values for the fit of the resonant background cross section of helium between 26 eV and 70 eV used to subtract the resonant background from the measured data of the $sp_{2,n+}$ doubly excited series. Fit function is a polynomial of fifth degree as given on top of the table. Data are fitted from figure 3 and table 1 in [127]. See also page 60.

C.2 Optical density near the doubly excited series

Series	Configuration	Energy (eV)	Γ (meV)	q	μ^2
N=2	1s2p	60.147	37.4	−2.77	0.345
	$sp_{2,3+}$	63.658	8.2	−2.58	0.306
	$sp_{2,4+}$	64.466	3.5	−2.55	0.295
	$sp_{2,5+}$	64.816	1.8	−2.54	0.290
	$sp_{2,6+}$	65.000	1.0	−2.53	0.290
	$sp_{2,7+}$	65.110	0.7	−2.52	0.289
	$sp_{2,8+}$	65.179	0.4	−2.58	0.282

Table C.2: Tabulated values for the $sp_{2,n+}$ doubly excited series. Data are extracted from [28]. See also Tab. 2.1 on page 20.

C.3 Optical density near the singly excited series

Series	Configuration	Energy (eV)	Γ (meV)	q	μ^2_{ge}
N=1	1s2p	21.2180	0.0074	$-\infty$	0.53143
	1s3p	23.0870	0.0023	$-\infty$	0.12988
	1s4p	23.7421	0.0010	$-\infty$	0.05136
	1s5p	24.0458	0.0005	$-\infty$	0.02554
	1s6p	24.2110	0.0003	$-\infty$	0.01455
	1s7p	24.3107	0.0002	$-\infty$	0.00908
	1s8p	24.3755	0.0001	$-\infty$	0.00605

Table C.3: Tabulated values for the first helium singly excited series (N=1). Data are extracted from NIST [71]. See also Tab. 2.1 on page 20.

Bibliography

[1] A. Kaldun, C. Ott, A. Blättermann, M. Laux, K. Meyer, T. Ding, A. Fischer, and T. Pfeifer.
Extracting phase- and amplitude modifications of laser-coupled Fano resonances.
accepted by Phys. Rev. Lett. (Feb 2014).
URL http://prl.aps.org/accepted/be074Y33Ze616b3559b93cc77ef264cc8e9b5f6f6.

[2] C. Ott, A. Kaldun, P. Raith, K. Meyer, M. Laux, J. Evers, C. H. Keitel, C. H. Greene, and T. Pfeifer.
Lorentz Meets Fano in Spectral Line Shapes: A Universal Phase and Its Laser Control.
Science **340**, 716–720 (2013).
URL http://www.sciencemag.org/content/340/6133/716.abstract.

[3] C. Ott, A. Kaldun, P. Raith, K. Meyer, M. Laux, Y. Zhang, S. Hagstotz, T. Ding, and T. Pfeifer.
Quantum Interferometry and Correlated Two-Electron Wave-Packet Observation in Helium.
arXiv:1205.0519v1 [physics.atom-ph] (2012).

[4] C. Ott, M. Schönwald, P. Raith, A. Kaldun, G. Sansone, M. Krüger, P. Hommelhoff, Y. Patil, Y. Zhang, K. Meyer, M. Laux, and T. Pfeifer.
Strong-field spectral interferometry using the carrier–envelope phase.
New Journal of Physics **15**, 073031 (2013).
URL http://stacks.iop.org/1367-2630/15/i=7/a=073031.

[5] P. Raith, C. Ott, K. Meyer, A. Kaldun, M. Laux, M. Ceci, C. P. Anderson, and T. Pfeifer.
Carrier-envelope phase- and spectral control of fractional high-harmonic combs.
Journal of Applied Physics **114**, – (2013).
URL http://scitation.aip.org/content/aip/journal/jap/114/17/10.1063/1.4827194.

[6] M. Kübel, N. G. Kling, K. J. Betsch, N. Camus, A. Kaldun, U. Kleineberg, I. Ben-Itzhak, R. R. Jones, G. G. Paulus, T. Pfeifer, J. Ullrich, R. Moshammer, M. F. Kling, and B. Bergues.
Nonsequential double ionization of N<math><msub><mrow></mrow><mn>2</mn></msub></math> in a near-single-cycle laser pulse.
Phys. Rev. A **88**, 023418 (Aug 2013).
URL http://link.aps.org/doi/10.1103/PhysRevA.88.023418.

[7] K. Meyer, C. Ott, P. Raith, A. Kaldun, Y. Jiang, A. Senftleben, M. Kurka, R. Moshammer, J. Ullrich, and T. Pfeifer.
Noisy Optical Pulses Enhance the Temporal Resolution of Pump-Probe Spectroscopy.
Phys. Rev. Lett. **108**, 098302 (Mar 2012).
URL http://link.aps.org/doi/10.1103/PhysRevLett.108.098302.

[8] P. Raith, C. Ott, C. Anderson, A. Kaldun, K. Meyer, M. Laux, Y. Zhang, and T. Pfeifer.
Fractional high-order harmonic combs and energy tuning by attosecond-precision split-spectrum pulse control.
Applied Physics Letters **100**, 121104–121104–5 (Mar 2012).

[9] T. A. Moore, P. Möhrke, L. Heyne, A. Kaldun, M. Kläui, D. Backes, J. Rhensius, L. J. Heyderman, J.-U. Thiele, G. Woltersdorf, A. Fraile Rodriguez, F. Nolting, T. O. Menteş, M. A. Niño, A. Locatelli, A. Potenza, H. Marchetto, S. Cavill, and S. S. Dhesi.
Magnetic-field-induced domain-wall motion in permalloy nanowires with modified Gilbert damping.
Phys. Rev. B **82**, 094445 (Sep 2010).
URL http://link.aps.org/doi/10.1103/PhysRevB.82.094445.

[10] J. Fraunhofer.
Bestimmung des Brechungs- und des Farben-Zerstreuungs - Vermögens verschiedener Glasarten, in Bezug auf die Vervollkommnung achromatischer Fernröhre.
Denkschriften der Königlichen Akademie der Wissenschaften zu München **5**, 193–226 (1814).

[11] P. Massey and M. Hanson.
Astronomical Spectroscopy.
arXiv:1010.5270v2 [astro-ph.IM] (2011).

[12] C. Leitherer, W. D. Vacca, P. S. Conti, A. V. Filippenko, C. Robert, and W. L. W. Sargent.
Hubble Space Telescope Ultraviolet Imaging and Spectroscopy of the Bright Starburst in the Wolf-Rayet Galaxy NGC 4214.
Astrophysical Journal **465**, 717 (Jul 1996).
URL
http://adsabs.harvard.edu/cgi-bin/bib_query?1996ApJ...465..717L.

[13] M. Rauch.
The Lyman Alpha Forest in the Spectra of QSOs.
ARA&A **36**, 267–316 (1998).

[14] T. Lyman.
The Spectrum of Hydrogen in the Region of Extremely Short Wave-Lengths.
Astrophysical Journal **23**, 181 (April 1906).

[15] R. Pohl, A. Antognini, F. Nez, F. D. Amaro, F. Biraben, J. M. R. Cardoso, D. S. Covita, A. Dax, S. Dhawan, L. M. P. Fernandes, A. Giesen, T. Graf, T. W. Hänsch, P. Indelicato, L. Julien, C.-Y. Kao, P. Knowles, E.-O. Le Bigot, Y.-W. Liu, J. A. M. Lopes, L. Ludhova, C. M. B. Monteiro, F. Mulhauser, T. Nebel, P. Rabinowitz, J. M. F. dos Santos, L. A. Schaller, K. Schuhmann, C. Schwob, D. Taqqu, J. F. C. A. Veloso, and F. Kottmann.
The size of the proton.
Nature **466**, 213–216 (2010).
URL http:
//www.nature.com/nature/journal/v466/n7303/abs/nature09250.html.

[16] H. Haken and H. C. Wolf.
Atom- und Quantenphysik.
8th edition. Springer Verlag (2004).

[17] http://physics.nist.gov/cuu/Constants/.

[18] M. Weitz, A. Huber, F. Schmidt-Kaler, D. Leibfried, W. Vassen, C. Zimmermann, K. Pachucki, T. W. Hänsch, L. Julien, and F. Biraben.
Precision measurement of the 1S ground-state Lamb shift in atomic hydrogen and deuterium by frequency comparison.
Phys. Rev. A **52**, 2664–2681 (Oct 1995).
URL http://link.aps.org/doi/10.1103/PhysRevA.52.2664.

[19] W. Demtröder.
Laserspektroskopie.
Second edition. Springer Verlag (1991).

[20] H. Beutler.
Über Absorptionsserien von Argon, Krypton und Xenon zu Termen zwischen den beiden Ionisierungsgrenzen $^2P\{_3/^{2/0}\}$ *und* $^2P\{_1/^{2/0}\}$.

Zeitschrift für Physik **93**, 177–196 (March 1935).

[21] E. Majorana.
Teoria dei tripletti P Incompleti.
Il Nuovo Cimento **8**, 107–113 (1931).
URL http://dx.doi.org/10.1007/BF02959482.

[22] A. Vittorini-Orgeas and A. Bianconi.
From Majorana Theory of Atomic Autoionization to Feshbach Resonances in High Temperature Superconductors.
Journal of Superconductivity and Novel Magnetism **22**, 215–221 (2009).
URL http://dx.doi.org/10.1007/s10948-008-0433-x.

[23] U. Fano.
Sullo spettro di assorbimento dei gas nobili presso il limite dello spettro d'arco.
Il Nuovo Cimento **12**, 154–161 (1935).
URL http://dx.doi.org/10.1007/BF02958288.

[24] H. Feshbach.
Unified theory of nuclear reactions.
Annals of Physics **5**, 357 – 390 (1958).
URL
http://www.sciencedirect.com/science/article/pii/0003491658900071.

[25] J. M. Blatt and V. F. Weisskopf.
Theoretical nuclear physics.
Wiley, New York (1952).

[26] R. P. Madden and K. Codling.
New Autoionizing Atomic Energy Levels in He, Ne, and Ar.
Phys. Rev. Lett. **10**, 516–518 (1963).

[27] U. Fano and J. W. Cooper.
Line Profiles in the Far-uv Absorption Spectra of the Rare Gases.
Phys. Rev. **137**, A1364–A1379 (1965).

[28] J. M. Rost, K. Schulz, M. Domke, and G. Kaindl.
Resonance parameters of photo doubly excited helium.
J. Phys. B **30**, 4663 (1997).

[29] M. Kroner, A. O. Govorov, S. Remi, B. Biedermann, S. Seidl, A. Badolato, P. M. Petroff, W. Zhang, R. Barbour, B. D. Gerardot, R. J. Warburton, and K. Karrai.
The nonlinear Fano effect.
Nature **451**, 311–314 (2008).

[30] A. E. Miroshnichenko, S. Flach, and Y. S. Kivshar.
Fano resonances in nanoscale structures.
Rev. Mod. Phys. **82**, 2257–2298 (2010).

[31] J. A. Fan, C. Wu, K. Bao, J. Bao, R. Bardhan, N. J. Halas, V. N. Manoharan, P. Nordlander, G. Shvets, and F. Capasso.
Self-Assembled Plasmonic Nanoparticle Clusters.
Science **328**, 1135–1138 (2010).
URL http://www.sciencemag.org/content/328/5982/1135.abstract.

[32] A. R. Schmidt, M. H. Hamidian, P. Wahl, F. Meier, A. V. Balatsky, J. D. Garrett, T. J. Williams, G. M. Luke, and J. C. Davis.
Imaging the Fano lattice to 'hidden order' transition in URu2Si2.
Nature **465**, 570 – 576 (2010).
URL http://dx.doi.org/10.1038/nature09073.

[33] S. H. Linn, W. Tzeng, J. M. Brom, and C. Y. Ng.
Molecular beam photoionization study of HgBr2 and HgI2.

The Journal of Chemical Physics **78**, 50–61 (1983).
URL http:
//scitation.aip.org/content/aip/journal/jcp/78/1/10.1063/1.444475.

[34] U. Fano.
Effects of Configuration Interaction on Intensities and Phase Shifts.
Physical Review **124**, 1866–1878 (December 1961).

[35] M. Domke, K. Schulz, G. Remmers, G. Kaindl, and D. Wintgen.
High-resolution study of $^1P^o$ double-excitation states in helium.
Phys. Rev. A **53**, 1424–1438 (1996).

[36] A. J. DeMaria, D. A. Stetser, and H. Heynau.
SELF MODE-LOCKING OF LASERS WITH SATURABLE ABSORBERS.
Applied Physics Letters **8**, 174–176 (1966).
URL http:
//scitation.aip.org/content/aip/journal/apl/8/7/10.1063/1.1754541.

[37] D. E. Spence, P. N. Kean, and W. Sibbett.
60-fsec pulse generation from a self-mode-locked Ti:sapphire laser.
Opt. Lett. **16**, 42–44 (Jan 1991).
URL http://ol.osa.org/abstract.cfm?URI=ol-16-1-42.

[38] P. M. Paul, E. S. Toma, P. Breger, G. Mullot, F. Augé, P. Balcou, H. G. Muller, and P. Agostini.
Observation of a Train of Attosecond Pulses from High Harmonic Generation.
Science **292**, 1689–1692 (2001).
URL http://www.sciencemag.org/content/292/5522/1689.abstract.

[39] A. Mcpherson, G. Gibson, H. Jara, U. Johann, T. S. Luk, I. A. Mcintyre, K. Boyer, and C. K. Rhodes.
Studies of Multiphoton Production of Vacuum Ultraviolet-Radiation in the Rare-Gases.
J. Opt. Soc. Am. B **4**, 595–601 (1987).

[40] A. L'Huillier and P. Balcou.
High-order harmonic generation in rare gases with a 1-ps 1053-nm laser.
Phys. Rev. Lett. **70**, 774–777 (Feb 1993).
URL http://link.aps.org/doi/10.1103/PhysRevLett.70.774.

[41] J. P. Geindre, A. Mysyrowicz, A. D. Santos, P. Audebert, A. Rousse, G. Hamoniaux, A. Antonetti, F. Falliès, and J. C. Gauthier.
Frequency-domain interferometer for measuring the phase and amplitude of a femtosecond pulse probing a laser-produced plasma.
Opt. Lett. **19**, 1997–1999 (Dec 1994).
URL http://ol.osa.org/abstract.cfm?URI=ol-19-23-1997.

[42] E. Tokunaga, T. Kobayashi, and A. Terasaki.
Frequency-domain interferometer for femtosecond time-resolved phase spectroscopy.
Opt. Lett. **17**, 1131–1133 (Aug 1992).
URL http://ol.osa.org/abstract.cfm?URI=ol-17-16-1131.

[43] S. Chen, K. J. Schafer, and M. B. Gaarde.
Transient absorption of attosecond pulse trains by laser-dressed helium.
Opt. Lett. **37**, 2211–2213 (Jun 2012).
URL http://ol.osa.org/abstract.cfm?URI=ol-37-12-2211.

[44] W.-C. Chu and C. D. Lin.
Absorption and emission of single attosecond light pulses in an autoionizing gaseous medium dressed by a time-delayed control field.
Phys. Rev. A **87**, 013415 (Jan 2013).
URL http://link.aps.org/doi/10.1103/PhysRevA.87.013415.

[45] M. J. J. Vrakking, D. M. Villeneuve, and A. Stolow.
Observation of fractional revivals of a molecular wave packet.

Phys. Rev. A **54**, R37–R40 (Jul 1996).
URL http://link.aps.org/doi/10.1103/PhysRevA.54.R37.

[46] T. Weinacht, J. Ahn, and P. Bucksbaum.
Controlling the shape of a quantum wavefunction.
Nature **397**, 233–235 (1999).
URL http://www.scopus.com/inward/record.url?eid=2-s2.0-0033590501.

[47] M. Wollenhaupt, A. Assion, D. Liese, C. Sarpe-Tudoran, T. Baumert, S. Zamith, M. A. Bouchene, B. Girard, A. Flettner, U. Weichmann, and G. Gerber.
Interferences of Ultrashort Free Electron Wave Packets.
Phys. Rev. Lett. **89**, 173001 (Oct 2002).
URL http://link.aps.org/doi/10.1103/PhysRevLett.89.173001.

[48] J. Mauritsson, T. Remetter, M. Swoboda, K. Klünder, A. L'Huillier, K. J. Schafer, O. Ghafur, F. Kelkensberg, W. Siu, P. Johnsson, M. J. J. Vrakking, I. Znakovskaya, T. Uphues, S. Zherebtsov, M. F. Kling, F. Lépine, E. Benedetti, F. Ferrari, G. Sansone, and M. Nisoli.
Attosecond Electron Spectroscopy Using a Novel Interferometric Pump-Probe Technique.
Phys. Rev. Lett. **105**, 053001 (Jul 2010).
URL http://link.aps.org/doi/10.1103/PhysRevLett.105.053001.

[49] A. Hibbert.
Developments in atomic structure calculations.
Reports on Progress in Physics **38**, 1217 (1975).
URL http://stacks.iop.org/0034-4885/38/i=11/a=001.

[50] P. E. Grabowski and D. F. Chernoff.
Pseudospectral calculation of helium wave functions, expectation values, and oscillator strength.
Phys. Rev. A **84**, 042505 (Oct 2011).
URL http://link.aps.org/doi/10.1103/PhysRevA.84.042505.

[51] P. Jorgensen.
Molecular and Atomic Applications of Time-Dependent Hartree-Fock Theory.
Annual Review of Physical Chemistry **26**, 359–380 (1975).
URL http://www.annualreviews.org/doi/abs/10.1146/annurev.pc.26.100175.002043.

[52] C.-Y. Chung, J. Hsu, S. Mukamel, and E. O. Potma.
Controlling stimulated coherent spectroscopy and microscopy by a position-dependent phase.
Phys. Rev. A **87**, 033833 (Mar 2013).
URL http://link.aps.org/doi/10.1103/PhysRevA.87.033833.

[53] R. Feynman, R. B. Leighton, and M. L. Sands.
The Feynman Lectures on Physics.
Addison-Wesley (1963).
3 volumes.

[54] M. Sargent, M. O. Scully, and W. E. Lamb.
Laser Physics.
Addison-Wesley (1974).

[55] F. Hopf and G. Stegeman.
Applied Classical Electrodynamics: Linear optics.
Wiley series in pure and applied optics. Wiley (1985).
URL http://books.google.de/books?id=dRpRAAAAMAAJ.

[56] S. Redner.
Citation Statistics From More Than a Century of Physical Review.
arXiv:physics/0407137 [physics.soc-ph] (2004).

[57] R. Boyd.
Nonlinear Optics.
Electronics & Electrical, third edition. Acad. Press, San Diego (2008).

URL http://books.google.de/books?id=30t9VmOmOGsC.

[58] U. FANO and J. W. COOPER.
Spectral Distribution of Atomic Oscillator Strengths.
Rev. Mod. Phys. **40**, 441–507 (Jul 1968).
URL http://link.aps.org/doi/10.1103/RevModPhys.40.441.

[59] D. M. Riffe.
Classical Fano oscillator.
Phys. Rev. B **84**, 064308 (Aug 2011).
URL http://link.aps.org/doi/10.1103/PhysRevB.84.064308.

[60] P. A. M. Dirac.
On the Theory of Quantum Mechanics.
Proceedings of the Royal Society of London. Series A **112**, 661–677 (1926).
URL
http://rspa.royalsocietypublishing.org/content/112/762/661.short.

[61] J. J. Sakurai.
Modern Quantum Mechanics.
revised edition. Addison Wesley (1994).

[62] M. O. Scully and S. Zubairy.
Quantum Optics.
Cambridge University Press (1997).
URL http://books.google.de/books?id=20ISsQCKKmQC.

[63] V. Weisskopf and E. Wigner.
Berechnung der natürlichen Linienbreite auf Grund der Diracschen Lichttheorie.
Zeitschrift für Physik **63**, 54–73 (1930).
URL http://dx.doi.org/10.1007/BF01336768.

[64] I. I. Rabi.
Space Quantization in a Gyrating Magnetic Field.
Phys. Rev. **51**, 652–654 (1937).

[65] B. J. Dalton and M. Gagen.
Strongly driven Stark coupled three-level systems and transitions at the Rabi frequency.
J. Phys. B **18**, 4403 (1985).

[66] L. Allen.
Optical Resonance and Two-level Atoms.
Courier Dover Publications (1987).

[67] S. H. Autler and C. H. Townes.
Stark Effect in Rapidly Varying Fields.
Phys. Rev. **100**, 703–722 (1955).

[68] E. Merzbacher.
Quantum mechanics.
Wiley (1961).
URL http://books.google.de/books?id=YgVRAAAAMAAJ.

[69] J. J. J. Sakurai and J. Napolitano.
Modern Quantum Mechanics.
ADDISON WESLEY Publishing Company Incorporated (2010).
URL http://books.google.de/books?id=N4I-AQAACAAJ.

[70] H. N. Russell and F. A. Saunders.
New Regularities in the Spectra of the Alkaline Earths.
Astrophysical Journal **61**, 38 (January 1925).

[71] http://physics.nist.gov/pml/data/asd.cfm.

[72] M. J. Bell, A. R. Beck, H. Mashiko, D. M. Neumark, and S. R. Leone.
Intensity dependence of light-induced states in transient absorption of laser-dressed helium measured with isolated attosecond pulses.
Journal of Modern Optics **60**, 1506–1516 (2013).
URL
http://www.tandfonline.com/doi/abs/10.1080/09500340.2013.826389.

[73] H. Klar.
Correlation in single- and multiphoton processes.
In F. Ehlotzky (Ed.), *Fundamentals of Laser Interactions*, volume 229 of *Lecture Notes in Physics*, pp. 149–160. Springer Berlin / Heidelberg (1985).
10.1007/3-540-15640-2_43.

[74] K. Schulz, G. Kaindl, M. Domke, J. D. Bozek, P. A. Heimann, A. S. Schlachter, and J. M. Rost.
Observation of New Rydberg Series and Resonances in Doubly Excited Helium at Ultrahigh Resolution.
Phys. Rev. Lett. **77**, 3086–3089 (1996).

[75] M. Domke, K. Schulz, G. Remmers, G. Kaindl, and D. Wintgen.
High-resolution study of $^1P^o$ double-excitation states in helium.
Phys. Rev. A **53**, 1424–1438 (Mar 1996).
URL http://link.aps.org/doi/10.1103/PhysRevA.53.1424.

[76] D. C. Morton, Q. Wu, and G. W. Drake.
Energy levels for the stable isotopes of atomic helium(4He I and 3He I).
Canadian Journal of Physics **84**, 83–105 (2006).
URL http://www.nrcresearchpress.com/doi/abs/10.1139/p06-009.

[77] R. C. G. Ligtenberg, P. J. M. van der Burgt, S. P. Renwick, W. B. Westerveld, and J. S. Risley.
Optical oscillator strengths of noble-gas resonance transitions in the vacuum-ultraviolet region.
Phys. Rev. A **49**, 2363–2380 (Apr 1994).
URL http://link.aps.org/doi/10.1103/PhysRevA.49.2363.

[78] A. Johansson, M. Raarup, Z. Li, V. Lokhnygin, D. Descamps, C. Lyngå, E. Mevel, J. Larsson, C.-G. Wahlström, S. Aloise, M. Gisselbrecht, M. Meyer, and A. L'Huillier.
Two-color pump-probe experiments in helium using high-order harmonics.
European Physical Journal D – Atoms, Molecules, Clusters & Optical Physics **22**, 3 – 11 (2003).

[79] G. Drake.
High Precision Calculations for Helium.
Springer Handbook of Atomic, Molecular, and Optical Physics pp. 199 – 219 (2006).

[80] G. Drake.
Springer Handbook of Atomic, Molecular, and Optical Physics.
Springer New York (2006).

[81] C. Cook.
Pulse Compression-Key to More Efficient Radar Transmission.
Proceedings of the IRE **48**, 310–316 (March 1960).

[82] D. Strickland and G. Mourou.
Compression of amplified chirped optical pulses.
Optics Communications **56**, 219 – 221 (1985).
URL
http://www.sciencedirect.com/science/article/pii/0030401885901208.

[83] P. F. Moulton.
Spectroscopic and laser characteristics of Ti:Al2O3.
J. Opt. Soc. Am. B **3**, 125–133 (Jan 1986).
URL http://josab.osa.org/abstract.cfm?URI=josab-3-1-125.

[84] http://www.femtolasers.com/.

[85] http://www.femtolasers.com/compact PRO.110.0.html.

[86] http://www.femtolasers.com/KALEIDOSCOPE TM.122.0.html.

[87] A. L'Huillier, L. A. Lompre, G. Mainfray, and C. Manus.
Multiply Charged Ions Formed by Multiphoton Absorption Processes in the Continuum.
Phys. Rev. Lett. **48**, 1814–1817 (Jun 1982).
URL http://link.aps.org/doi/10.1103/PhysRevLett.48.1814.

[88] G. G. Paulus, W. Nicklich, H. Xu, P. Lambropoulos, and H. Walther.
Plateau in above threshold ionization spectra.
Phys. Rev. Lett. **72**, 2851–2854 (May 1994).
URL http://link.aps.org/doi/10.1103/PhysRevLett.72.2851.

[89] A. Sperl.
private communications.

[90] P. Jaegle.
Coherent Sources of XUV Radiation.
Springer, New York (2006).

[91] L. V. Keldysh.
Ionization in field of a strong electromagnetic wave.
Sov. Phys. JETP **20**, 1307–& (1965).

[92] P. B. Corkum and F. Krausz.
Attosecond science.
Nature Phys. **3**, 381–387 (2007).

[93] C. Winterfeldt, C. Spielmann, and G. Gerber.
Colloquium: Optimal control of high-harmonic generation.
Rev. Mod. Phys. **80**, 117–140 (Jan 2008).
URL http://link.aps.org/doi/10.1103/RevModPhys.80.117.

[94] P. Salières, P. Antoine, A. de Bohan, and M. Lewenstein.
Temporal and Spectral Tailoring of High-Order Harmonics.
Phys. Rev. Lett. **81**, 5544–5547 (1998).

[95] J. Mauritsson, P. Johnsson, E. Gustafsson, A. L'Huillier, K. J. Schafer, and M. B. Gaarde.
Attosecond Pulse Trains Generated Using Two Color Laser Fields.
Phys. Rev. Lett. **97**, 013001 (Jul 2006).
URL http://link.aps.org/doi/10.1103/PhysRevLett.97.013001.

[96] A. L'Huillier, K. J. Schafer, and K. C. Kulander.
Theoretical aspects of intense field harmonic generation.
Journal of Physics B: Atomic, Molecular and Optical Physics **24**, 3315 (1991).
URL http://stacks.iop.org/0953-4075/24/i=15/a=004.

[97] R. W. Boyd.
Nonlinear Optics.
Second edition. Academic Press, San Diego (2003).

[98] W. H. Wollaston.
A Method of Examining Refractive and Dispersive Powers, by Prismatic Reflection.
Philosophical Transactions of the Royal Society of London **92**, 365–380 (1802).
URL http://rstl.royalsocietypublishing.org/content/92/365.short.

[99] W. T. Pollard and R. A. Mathies.
Analysis of Femtosecond Dynamic Absorption Spectra of Nonstationary States.
Annual Review of Physical Chemistry **43**, 497–523 (1992).
URL http://www.annualreviews.org/doi/abs/10.1146/annurev.pc.43.100192.002433.
PMID: 1463575.

[100] L. d. M. M. Eigen.
Self-Dissociation and Protonic Charge Transport in Water and Ice.
Proceedings of the Royal Society A: Mathematical, Physical and Engineering Sciences **246**, 505–533 (1958).

[101] Z.-H. Loh, C. H. Greene, and S. R. Leone.
Femtosecond induced transparency and absorption in the extreme ultraviolet by coherent coupling of the He 2s2p (1Po) and 2p2 (1Se) double excitation states with 800 nm light.
Chem. Phys. **350**, 7 – 13 (2008).

[102] E. Goulielmakis, Z.-H. Loh, A. Wirth, R. Santra, N. Rohringer, V. S. Yakovlev, S. Zherebtsov, T. Pfeifer, A. M. Azzeer, M. F. Kling, S. R. Leone, and F. Krausz.
Real-time observation of valence electron motion.
Nature **466**, 739–743 (2010).

[103] H. Wang, M. Chini, S. Chen, C.-H. Zhang, F. He, Y. Cheng, Y. Wu, U. Thumm, and Z. Chang.
Attosecond Time-Resolved Autoionization of Argon.
Phys. Rev. Lett. **105**, 143002 (2010).

[104] M. Holler, F. Schapper, L. Gallmann, and U. Keller.
Attosecond Electron Wave-Packet Interference Observed by Transient Absorption.
Phys. Rev. Lett. **106**, 123601 (2011).

[105] T. Remetter, P. Johnsson, J. Mauritsson, K. Varju, Y. Ni, F. Lepine, E. Gustafsson, M. Kling, J. Khan, R. Lopez-Martens, K. J. Schafer, M. J. J. Vrakking, and A. L/'huillier.
Attosecond electron wave packet interferometry.
Nat Phys **2**, 323–326 (May 2006).
URL http://dx.doi.org/10.1038/nphys290.

[106] M. Hentschel, R. Kienberger, C. Spielmann, G. A. Reider, N. Milosevic, T. Brabec, P. B. Corkum, U. Heinzmann, M. Drescher, and F. Krausz.
Attosecond metrology.
Nature **414**, 509 (2001).

[107] J. Itatani, F. Quéré, G. L. Yudin, M. Y. Ivanov, F. Krausz, and P. B. Corkum.
Attosecond streak camera.
Phys. Rev. Lett. **88**, 173903 (2002).

[108] J. Mauritsson, T. Remetter, M. Swoboda, K. Klünder, A. L'Huillier, K. J. Schafer, O. Ghafur, F. Kelkensberg, W. Siu, P. Johnsson, M. J. J. Vrakking, I. Znakovskaya, T. Uphues, S. Zherebtsov, M. F. Kling, F. Lépine, E. Benedetti, F. Ferrari, G. Sansone, and M. Nisoli.
Attosecond Electron Spectroscopy Using a Novel Interferometric Pump-Probe Technique.
Phys. Rev. Lett. **105**, 053001 (2010).

[109] E. Goulielmakis, Z.-H. Loh, A. Wirth, R. Santra, N. Rohringer, V. S. Yakovlev, S. Zherebtsov, T. Pfeifer, A. M. Azzeer, M. F. Kling, S. R. Leone, and F. Krausz.
Real-time observation of valence electron motion.
Nature **466**, 739–743 (2010).
URL http://www.nature.com/nature/journal/v466/n7307/abs/nature09212.html.

[110] M. Joffre, D. Hulin, J. Chambaret, A. Migus, A. Antonetti, and C. Benoit ä la Guillaume.
Bleaching of an Exciton Line Using Sub-T2 Pulses: Artifact or Reality?
Proceedings of the 6th International Conference on Ultrafast Phenomena pp. 223–225 (Jul 1988).

[111] X. Dai, M. Richter, H. Li, A. D. Bristow, C. Falvo, S. Mukamel, and S. T. Cundiff.
Two-Dimensional Double-Quantum Spectra Reveal Collective Resonances in an Atomic Vapor.
Phys. Rev. Lett. **108**, 193201 (May 2012).
URL http://link.aps.org/doi/10.1103/PhysRevLett.108.193201.

[112] K. T. Kim, C. Zhang, T. Ruchon, J.-F. Hergott, T. Auguste, D. M. Villeneuve, P. B. Corkum, and F. Quere.
Photonic streaking of attosecond pulse trains.

Nature Photonics **7**, 651 – 656 (2013).
URL http://dx.doi.org/10.1038/nphoton.2013.170.

[113] J. Nentwig.
Kunststoff-Folien: Herstellung, Eigenschaften, Anwendung.
Third edition. Carl Hanser Verlag (2006).
URL http://books.google.de/books?id=sIdhvOEdkvcC.

[114] http://henke.lbl.gov/optical_constants/.

[115] http://www.lebowcompany.com/.

[116] http://www.physikinstrumente.com/.

[117] https://www.newport.com/Agilis
Series-Piezo-Motor-Driven-Rotation-Stages/685206/1033/info.aspx.

[118] G. G. Paulus, F. Lindner, H. Walther, A. Baltuška, E. Goulielmakis, M. Lezius, and F. Krausz.
Measurement of the Phase of Few-Cycle Laser Pulses.
Phys. Rev. Lett. **91**, 253004 (2003).

[119] A. Ellett and R. M. Zabel.
The Pirani Gauge for the Measurement of Small Changes of Pressure.
Phys. Rev. **37**, 1102–1111 (May 1931).
URL http://link.aps.org/doi/10.1103/PhysRev.37.1102.

[120] H. A. Rowland.
XXIX. On concave gratings for optical purposes.
Philos. Mag. Ser. 5 **16**, 197–210 (1883).

[121] H. G. Beutler.
The Theory of the Concave Grating.
J. Opt. Soc. Am. **35**, 311–350 (1945).

[122] T. Kita, T. Harada, N. Nakano, and H. Kuroda.
Mechanically ruled aberration-corrected concave gratings for a flat-field grazing-incidence spectrograph.
Appl. Opt. **22**, 512–513 (1983).

[123] N. Nakano, H. Kuroda, T. Kita, and T. Harada.
Development of a flat-field grazing-incidence XUV spectrometer and its application in picosecond XUV spectroscopy.
Appl. Opt. **23**, 2386–2392 (1984).

[124] http://www.lambda-at.com/pdf/ConcaveGrating Spectrograph-Grazing(1)%5B1%5D.pdf.

[125] http://www.princetoninstruments.com/.

[126] X. Wang, M. Chini, Y. Cheng, Y. Wu, and Z. Chang.
In situ calibration of an extreme ultraviolet spectrometer for attosecond transient absorption experiments.
Appl. Opt. **52**, 323–329 (Jan 2013).
URL http://ao.osa.org/abstract.cfm?URI=ao-52-3-323.

[127] J. A. R. Samson, Z. X. He, L. Yin, and G. N. Haddad.
Precision measurements of the absolute photoionization cross sections of He.
J. Phys. B **27**, 887 (1994).

[128] C. Ott.
Attosecond multidimensional interferometry of single and two correlated electrons in atoms.
PhD Thesis, Universität Heidelberg (2012).

[129] S. E. Harris.
Electromagnetically Induced Transparency.
Physics Today **50** (1997).

URL http://scitation.aip.org/content/aip/magazine/physicstoday/article/50/7/10.1063/1.881806.

[130] M. Fleischhauer, A. Imamoglu, and J. P. Marangos.
Electromagnetically induced transparency: Optics in coherent media.
Rev. Mod. Phys. **77**, 633–673 (Jul 2005).
URL http://link.aps.org/doi/10.1103/RevModPhys.77.633.

[131] R. W. Boyd and D. J. Gauthier.
'Slow' and 'fast' light.
Progress in Optics **43**, 497– 530 (2002).

[132] J. B. Khurgin.
Slow light in various media: a tutorial.
Adv. Opt. Photon. **2**, 287–318 (Sep 2010).
URL http://aop.osa.org/abstract.cfm?URI=aop-2-3-287.

[133] A. E. Siegman.
Lasers.
University Science Books, Sausalito (1986).

[134] M. Chini, B. Zhao, H. Wang, Y. Cheng, S. X. Hu, and Z. Chang.
Subcycle ac Stark Shift of Helium Excited States Probed with Isolated Attosecond Pulses.
Phys. Rev. Lett. **109**, 073601 (Aug 2012).
URL http://link.aps.org/doi/10.1103/PhysRevLett.109.073601.

[135] M. Chini, X. Wang, Y. Cheng, Y. Wu, D. Zhao, D. A. Telnov, S.-I. Chu, and Z. Chang.
Sub-cycle Oscillations in Virtual States Brought to Light.
Sci. Rep. **3** (January 2013).
URL http://dx.doi.org/10.1038/srep01105.

[136] F. He, C. Ruiz, A. Becker, and U. Thumm.
Attosecond probing of instantaneous ac Stark shifts in helium atoms.
Journal of Physics B: Atomic, Molecular and Optical Physics **44**, 211001 (2011).
URL http://stacks.iop.org/0953-4075/44/i=21/a=211001.

[137] S. Chen, M. Wu, M. B. Gaarde, and K. J. Schafer.
Quantum interference in attosecond transient absorption of laser-dressed helium atoms.
Phys. Rev. A **87**, 033408 (Mar 2013).
URL http://link.aps.org/doi/10.1103/PhysRevA.87.033408.

[138] M. Tarana and C. H. Greene.
Femtosecond transparency in the extreme-ultraviolet region.
Phys. Rev. A **85**, 013411 (2012).

[139] W.-C. Chu and C. D. Lin.
Photoabsorption of attosecond XUV light pulses by two strongly laser-coupled autoionizing states.
Phys. Rev. A **85**, 013409 (2012).

[140] S. Chen, M. J. Bell, A. R. Beck, H. Mashiko, M. Wu, A. N. Pfeiffer, M. B. Gaarde, D. M. Neumark, S. R. Leone, and K. J. Schafer.
Light-induced states in attosecond transient absorption spectra of laser-dressed helium.
Phys. Rev. A **86**, 063408 (Dec 2012).
URL http://link.aps.org/doi/10.1103/PhysRevA.86.063408.

[141] A. Hooker, C. H. Greene, and W. Clark.
Classical examination of the Stark effect in hydrogen.
Phys. Rev. A **55**, 4609–4612 (Jul 1997).
URL http://link.aps.org/doi/10.1103/PhysRevA.55.4609.

[142] K. Ito, K. Yoshino, Y. Morioka, and T. Namioka.
The 1 s 2 1 S 0 –1 snp 1 P 1 0 series of the helium spectrum.
Physica Scripta **36**, 88 (1987).
URL http://stacks.iop.org/1402-4896/36/i=1/a=014.

[143] M. Schultze, M. Fieß, N. Karpowicz, J. Gagnon, M. Korbman, M. Hofstetter, S. Neppl, A. L. Cavalieri, Y. Komninos, T. Mercouris, C. A. Nicolaides, R. Pazourek, S. Nagele, J. Feist, J. Burgdörfer, A. M. Azzeer, R. Ernstorfer, R. Kienberger, U. Kleineberg, E. Goulielmakis, F. Krausz, and V. S. Yakovlev.
Delay in Photoemission.
Science **328**, 1658–1662 (2010).
URL http://www.sciencemag.org/content/328/5986/1658.abstract.

[144] O. Kocharovskaya.
Amplification and lasing without inversion.
Physics Reports **219**, 175 – 190 (1992).
URL
http://www.sciencedirect.com/science/article/pii/037015739290135M.

[145] L. Argenti, C. Ott, T. Pfeifer, and F. Martín.
Attosecond Transient Absorption Spectroscopy of doubly-excited states in helium.
arXiv:1211.2566v1 [physics.atom-ph] (2012).

[146] M. Heinz, F. Vewinger, U. Schneider, L. P. Yatsenko, and K. Bergmann.
Phase control in a coherent superposition of degenerate quantum states through frequency control.
Optics Communications **264**, 248 – 255 (2006).
URL http:
//www.sciencedirect.com/science/article/pii/S0030401806004846.

[147] P. M. Kraus, S. B. Zhang, A. Gijsbertsen, R. R. Lucchese, N. Rohringer, and H. J. Wörner.
High-Harmonic Probing of Electronic Coherence in Dynamically Aligned Molecules.
Phys. Rev. Lett. **111**, 243005 (Dec 2013).
URL http://link.aps.org/doi/10.1103/PhysRevLett.111.243005.

[148] J. Mauritsson, P. Johnsson, E. Mansten, M. Swoboda, T. Ruchon, A. L'Huillier, and K. J. Schafer.
Coherent Electron Scattering Captured by an Attosecond Quantum Stroboscope.
Phys. Rev. Lett. **100**, 073003 (Feb 2008).
URL http://link.aps.org/doi/10.1103/PhysRevLett.100.073003.

[149] B. Dai and P. Lambropoulos.
Dynamics of 3- and 4-level systems under strong field and ionization.
Zeitschrift für Physik D Atoms, Molecules and Clusters **3**, 11–21 (1986).
URL http://dx.doi.org/10.1007/BF01442343.

[150] K. Bergmann, H. Theuer, and B. W. Shore.
Coherent population transfer among quantum states of atoms and molecules.
Rev. Mod. Phys. **70**, 1003–1025 (Jul 1998).
URL http://link.aps.org/doi/10.1103/RevModPhys.70.1003.

[151] L. Argenti and E. Lindroth.
Ionization Branching Ratio Control with a Resonance Attosecond Clock.
Phys. Rev. Lett. **105**, 053002 (2010).

[152] M. Wu, S. Chen, K. J. Schafer, and M. B. Gaarde.
Ultrafast time-dependent absorption in a macroscopic three-level helium gas.
Phys. Rev. A **87**, 013828 (Jan 2013).
URL http://link.aps.org/doi/10.1103/PhysRevA.87.013828.

[153] W. B. Westerveld, F. B. Kets, H. G. M. Heideman, and J. van Eck.
Electron impact excitation of the (2p 2) 3 P doubly excited state of helium.
Journal of Physics B: Atomic and Molecular Physics **12**, 2575 (1979).
URL http://stacks.iop.org/0022-3700/12/i=15/a=018.

[154] G. W. F. Drake and A. Dalgarno.
States of the Helium Isoelectronic Sequence.
Phys. Rev. A **1**, 1325–1329 (May 1970).
URL http://link.aps.org/doi/10.1103/PhysRevA.1.1325.

[155] M. Domke, C. Xue, A. Puschmann, T. Mandel, E. Hudson, D. A. Shirley, G. Kaindl, C. H. Greene, H. R. Sadeghpour, and H. Petersen.
Extensive double-excitation states in atomic helium.
Phys. Rev. Lett. **66**, 1306–1309 (Mar 1991).
URL http://link.aps.org/doi/10.1103/PhysRevLett.66.1306.

[156] Z.-H. Loh, M. Khalil, R. E. Correa, R. Santra, C. Buth, and S. R. Leone.
Quantum State-Resolved Probing of Strong-Field-Ionized Xenon Atoms Using Femtosecond High-Order Harmonic Transient Absorption Spectroscopy.
Phys. Rev. Lett. **98**, 143601 (Apr 2007).
URL http://link.aps.org/doi/10.1103/PhysRevLett.98.143601.

[157] H. Wang, M. Chini, S. Chen, C.-H. Zhang, Y. Cheng, F. He, Y. Wu, U. Thumm, and Z. Chang.
Attosecond Time-Resolved Autoionization of Argon.
Phys. Rev. Lett. **105**, 143002 (Oct 2010).
URL http://link.aps.org/doi/10.1103/PhysRevLett.105.143002.

[158] M. Holler, F. Schapper, L. Gallmann, and U. Keller.
Attosecond Electron Wave-Packet Interference Observed by Transient Absorption.
Phys. Rev. Lett. **106**, 123601 (Mar 2011).
URL http://link.aps.org/doi/10.1103/PhysRevLett.106.123601.

[159] J. M. Rost, K. Schulz, M. Domke, and G. Kaindl.
Resonance parameters of photo doubly excited helium.
Journal of Physics B: Atomic, Molecular and Optical Physics **30**, 4663 (1997).
URL http://stacks.iop.org/0953-4075/30/i=21/a=010.

[160] G. Taubin.
Estimation of Planar Curves, Surfaces, and Nonplanar Space Curves Defined by Implicit Equations with Applications to Edge and Range Image Segmentation.
IEEE Trans. Pattern Anal. Mach. Intell. **13**, 1115–1138 (1991).

[161] K. Kanatani and P. Rangarajan.
Hyper least squares fitting of circles and ellipses.
Computational Statistics & Data Analysis **55**, 2197–2208 (2011).

[162] A. H. Safavi-Naeini, T. P. M. Alegre, J. Chan, M. Eichenfield, M. Winger, Q. Lin, J. T. Hill, D. E. Chang, and O. Painter.
Electromagnetically induced transparency and slow light with optomechanics.
Nature **472**, 69–73 (April 2011).

[163] M. O. Scully.
From lasers and masers to phaseonium and phasers.
Physics Reports **219**, 191 – 201 (1992).
URL
http://www.sciencedirect.com/science/article/pii/037015739290136N.

[164] R. N. Shakhmuratov, F. Vagizov, and O. Kocharovskaya.
Radiation burst from a single γ-photon field.
Phys. Rev. A **84**, 043820 (Oct 2011).
URL http://link.aps.org/doi/10.1103/PhysRevA.84.043820.

[165] D. Marcuse.
Maser action without population inversion.
Proceedings of the IEEE **51**, 849–850 (May 1963).

[166] P. Bouger.
Essai d'optique sur la gradation de la lumiere.
Les matres de la pensee scientifique (1792).

[167] A. Beer.
Bestimmung der Absorption des rothen Lichts in farbigen Flüssigkeiten.
Annal. Phys. Chem. **86**, 78–88 (1852).

[168] J. Lambert and E. Anding.
Lamberts Photometrie: (Photometria, sive De mensura et gradibus luminis, colorum et umbrae) (1760).
Number v. 1-2 in Ostwalds Klassiker der exakten Wissenschaften. W. Engelmann (1892).
URL `http://books.google.de/books?id=Fq4RAAAAYAAJ`.

Danksagung

Stets hilfsbereit und mit offenem Ohr,
ob für Probleme mit Physik oder im Labor,
beim Verstehen der Daten mit vollem Eifer,
stand mir zur Seite Thomas Pfeifer.

Hier beim Dank möcht' ich noch beachten,
Selim Jochim fürs Zweitgutachten.

Ob Tag oder Nacht,
wir haben's möglich gemacht:
über Fanolinien stets die Kontrolle.
Entfernung spielte keine Rolle,
stets korrigierte meine Texte er flott,
vielen Dank, Christian Ott!

Teilten uns Fahrrad, Bett und Schlitten,
haben gemeinsam viel durchlitten,
doch lachten stets - das war sicher,
es war eine tolle Zeit, Andreas Fischer!

Thomas Ding will ich beim Dank nicht vergessen,
leistete große Hilfe beim Aufbau und Messen.

Im Büro teilten wir Lachen und Klagen,
hatten uns -in englisch- viel zu sagen,
bewahrtest mich in China vor Leid und Weh,
vielen Dank, lieber Zouye.

Danke liebes Team Interatto
für die gemeinsame Zeit,
namentlich sind's genau:
Kristina, Martin, und Veit
Alex B., und Yonghao,
und einst zählten hinzu
Rima, Philipp, Steffen und Yizhu.

Für die Zuflucht beim Schreiben
die Tipps, die zahlreichen und teuren,
auch ein Dank an Seb Meuren.

Gab es Brot, war'n wir stets gut gelaunt
haben die Wälder durchfahren und bestaunt
danke, Alex Sperl, für's sportliche Trainieren,
und natürlich für's exakte Korrigieren.

Danke, Nico, für die vielen Stündchen,
die wir zusammen arbeiteten in München,
bei Nachtschichten warst du eine Frohnatur
zudem last du mir viele Seiten Korrektur
genau wie du, Bettina Fischer,
auch darum ist mein Dank dir sicher.

Danke, liebe Freunde nah und fern,
ich hab euch alle wirklich gern,
ihr teilt Sorgen mit mir und Lachen,
- ohne euch war die Arbeit nicht zu machen!

Auch für deine Unterstützung sag ich Danke,
Anke!

Liebe Verwandte, ihr seid toll,
wart des Verständnisses immer voll,
musstet ihr auch oft auf mich verzichten
- da wird auch dieser Dank nicht's richten.

Mein Bruderherz, auch an dich hab ich gedacht,
an die Kindheitstage, die wir gemeinsam verbracht,
und es warten auf uns - das ist keine Frage,
noch viele gemeinsam glückliche Tage!

Du hast mich stets bei meiner Arbeit unterstützt,
getan, was immer mir auch nützt
(mir sogar Essen zubereitet)
bist mein Lichblick, der mich lenkt und der mich leitet,
du bist mein Stella Polaris,
vielen Dank dir, liebe Charis!

Norbert, du liebst sie beide, deine Söhne,
hast viele Erinnerungen - witzige und schöne,
und hast dich stets für mich eingesetzt,
so gilt mein Dank dir nicht zuletzt.

Eva, hast das Leben mir geschenkt
und gelehrt, wie man ein Auto lenkt,
und du hast auf viel für mich verzichtet,
drum bin zu herzenstiefstem Dank ich dir verpflichtet!